Quantitative Spectroscopy for Detection of Cervical Dysplasia

by

Jelena Mirković

B.S. Chemistry and Biology
Coastal Carolina University
(2001)

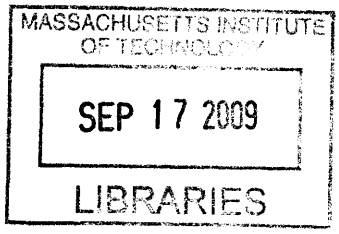

ARCHIVES

SUBMITTED TO THE HARVARD/MIT DIVISION OF
HEALTH SCIENCES AND TECHNOLOGY
IN PARTIAL FULFILLMENT OF THE REQUIREMENTS FOR THE DEGREE OF

DOCTOR OF PHILOSOPHY IN HEALTH SCIENCES AND TECHNOLOGY

at the

MASSACHUSETTS INSTITUTE OF TECHNOLOGY

June 2009

Signature of the Author:.....
Department of Health Sciences and Technology
May 1 2009

Certified by:.....
Michael S. Feld
Professor of Physics and Director of G. R .Harrison Spectroscopy Laboratory
Thesis Supervisor

Accepted by:.....
Ram Sasisekharan
Director of Health Sciences and Technology and Edward Hood Taplin Professor of
Health Sciences & Technology and Biological Engineering

Quantitative Spectroscopy for Detection of Cervical Dysplasia

by

Jelena Mirković

Submitted to the Harvard/MIT Division of Health Sciences and Technology
on May 1st, 2009 in Partial Fulfillment of the Requirements for the Degree of
Doctor of Philosophy in Health Sciences and Technology

Abstract

The current clinical standard for cervical cancer diagnosis is colposcopy, a procedure that involves visual inspection and biopsy of at-risk tissue, followed by histopathology. The major objective of colposcopy is detection of high-grade squamous intraepithelial lesions (HSIL), which are precancerous lesions with high risk of progression. Colposcopy, even when conducted by experts, is subject to significant diagnostic variability. The aim of the work presented in this thesis was to develop a non-invasive clinical tool for detection of cervical HSIL and for guiding the biopsy during colposcopy. Previously we have developed a contact-probe portable instrument for tissue reflectance and fluorescence collection, and spectral analysis models to extract and quantify biochemical and structural features of tissue to provide disease state assessment. In this thesis we further refine the instrumentation and spectral analysis models and conduct the clinical *in vivo* studies. The clinical *in-vivo* study showed cervical anatomy was a confounder to diagnostic algorithms that treat cervix as spectroscopically uniform. We used complex instrumentation to comprehensively study cervical tissue and found that scattering alone was sufficient to identify HSIL. We developed an accurate algorithm based on tissue scattering for detection of HSIL in the cervical transformation zone, an area where vast majority of cervical lesions arise. We further successfully extended our point-probe technique into the imaging mode, to provide the wide-area surveillance capability. The on-going imaging clinical *in-vivo* feasibility study demonstrates spectroscopic contrast between cervical HSIL and non-HSIL tissue and is consistent with findings of the contact-probe study. The future steps include diagnostic accuracy assessment of the imaging technique, and if proven successful, a clinical study to evaluate the performance of spectroscopy-guided biopsy.

Thesis supervisor: Michael S. Feld
Title: Professor of Physics and Director of G.H. Spectroscopy Laboratory

Acknowledgments

I would like to dedicate this thesis to my family, mother Ruza Jeremic-Mirkovic, father Dusan Mirkovic, brother Milos Mirkovic, and Grandmother Radmila Jeremic. Without their love and constant support I would have never been able to achieve any of the important goals in my life. They were and continue to be pillars of my strength. Hvala, dragi moji.

At the end of the incredible journey of my graduate school education I reflect upon years of scientific joy and struggle. Under the guidance of my advisor, Michael Feld, I grew as a scientist and as a person. I thank him for optimism, support, and belief in me even when I lacked it myself. Thank you, Michael.

I thank members of my thesis committee: Roger Mark, Elizabeth Stier, and Christopher Crum for their scientific and clinical guidance, time, and effort.

I would like to thank from the bottom of my heart to my scientific sister Sasha McGee for her companionship, for going through every graduate/medical school battle with me and for always being there for me. Our "Dynamic Duo" moments went from chemistry cumulative exams, to the Spec Lab fun and cries over years, through all the medical school classes, to Cairo, and I am looking forward to continuing our sisterhood passed the graduate school era.

The clinical work that led to the achievements of this thesis could not have been carried out without a joint effort of many colleagues. I thank an MIT engineer Luis Galindo for manufacturing the instrumentation and to my clinical collaborators Elizabeth Stier, Antonio De las Morenas, Victoria Feng, Olivera Vragovic, Danny Schust, and Cathrina McGahan from Boston Medical Center and Christopher Crum from Brigham and Women's Hospital for their contributions to the project. Dr. Stier, thank you so much for being accommodating, patient, and understanding with me as a scientist in the colposcopy clinic. Dr. Crum, thank you for investing so much time and effort in teaching me about cervical pathology. Your personality and work is an inspiration to me.

I was blessed by having wonderful colleagues, past and present, at the MIT Spectroscopy Laboratory and I thank all of them for their support. I would especially like to thank Condon Lau for his infectious optimism, for grilling me with tough scientific questions, and for always being ready to help. I would like to thank Chung-Chieh Yu, Kamran Badizadegan, Obrad Scepanovic, Max Kalashnikov, and Martin Hunter, for many helpful discussions. Zoya Volynskaya has been a source of laughs in my graduate school life. Thank you so much, DM, for your support and friendship. I thank James Tunnell for his guidance early in my graduate school career and Jonathan Nazemi for his numerous contributions to instrumentation and science in my project and even more for his friendship and laughs.

I would like to thank Collin Stultz for giving me a wonderful Introduction to Clinical Medicine experience, but also for being my mentor outside of the lab and for his care, understanding, and support when I was going through the toughest time during my PhD. Thanks so much, Collin.

Cathy Modica touched me with her kindness. You are one of the HST's biggest assets. Thanks, Cathy, for your support.

I thank my dear friends Kit Kadlec, Tanja Radovic, Nikola Kojic, Sandra Pekic, Peng Yu, Al-Thaddeus Avestruz, Justin Hodgkiss, and Dmitry Pushin for their friendship and love through the years.

Table of Contents

List of Figures

List of Tables

List of Abbreviations

Term	Definition
AUC	Area under the ROC curve
bvr	Effective blood vessel radius
CNS	Clinically normal squamous sites
Coll	Fractional contribution of collagen fluorescence to IFS
DRS	Diffuse Reflectance Spectroscopy
HSIL	High grade squamous intraepithelial lesion
IFS	Intrinsic Fluorescence Spectroscopy
LCV	Leave-one-out cross-validation
LEEP	Loop Electrosurgical Excision Procedure
LSIL	Low grade squamous intraepithelial lesion
Non-SG	Non-HSIL sites with <25% of the stroma occupied by glands
non-HSIL	Clinically suspicious sites which were not HSILs by histopathology
NT	Normal transformation zone
QSI	Quantitative Spectroscopy Imaging
SG	Non-HSIL sites with ≥25% of the stroma occupied by glands
SIL	Squamous intraepithelial lesion
Hb	Hemoglobin concentration
α	Oxygen saturation of hemoglobin
β-car	Concentration of β-carotene

CHAPTER 1

Introduction

Here we introduce the overall goal of the work presented in this thesis, followed by the overview of the thesis accomplishments and thesis content.

1.1 Motivation

Cervical cancer, one of the major causes of cancer death in women worldwide, is usually preceded by a precursor condition known as dysplasia. This condition is characterized by metabolic and proliferative changes in epithelial cells and structural reorganization of the connective tissue.[1] Surveillance strategies for dysplasia target early identification of patients at risk of cancer development. The current clinical standard for cervical dysplasia diagnosis is colposcopy, a procedure that involves visual inspection and biopsy of at-risk tissue, followed by histopathology.[2] The accuracy of colposcopy highly depends on the physician's expertise. The reported values of sensitivity and specificities vary widely in the literature. In expert hands, colposcopy is quite sensitive for detection of high-grade squamous intraepithelial lesions (HSILs), which are dysplastic lesions with high risk of progression.[3] However, colposcopy exhibits low specificity which leads to many unnecessary biopsies.[3] Sampling of tissue is invasive to the patient, and specimen processing and diagnosis are time consuming, requiring hours to days before a diagnosis can be rendered. Furthermore, diagnosis of dysplasia can be unreliable because of low intra- and inter-observer agreement in histopathology diagnosis.

In contrast, spectroscopic techniques, which are based on light-tissue interactions, can be developed to provide diagnostic information non-invasively, in real-time, and in an objective and quantitative manner. As an objective real-time diagnostic tool, spectroscopy could potentially reduce the interobserver disagreement in colposcopy and the amount of unnecessary biopsies during colposcopy. Spectroscopic techniques, implemented in contact probe manner, as well as imaging with wide-area surveillance capabilities, have been tested in various stages of clinical studies, from pilot to phase III clinical studies.[4-13] These studies show the potential of spectroscopy to guide biopsy during colposcopic examination to improve the accuracy of disease detection.

The sources of contrast in tissue spectra due to the presence of disease are related to the changes that accompany cervical dysplasia, including loss of differentiation of the epithelial cells[1], degradation and reorganization of stromal

collagen by matrix metalloproteinase activity[14,15], and angiogenesis[16]. Several research projects, including this thesis, use physically based models to extract spectroscopic parameters related to cervical tissue properties from tissue spectra and used them to develop disease diagnostic algorithms.[6,10,17] The advantage of the model-based spectroscopy techniques is that they provide an understanding of the origins of spectroscopic contrast between normal and diseased tissue, and they diagnose disease based on quantitative information about tissue morphology and biochemistry.

Central to the research presented in this thesis is the notion that cervical tissue spectroscopy is not only affected by disease, but by other factors such as age[18,19], menopausal status[19,20], time after the application of acetic acid[8], and normal variations in cervical anatomy[5,13,19]. For example, spectroscopic differences between normal ectocervix (the outer zone of the cervix lined by stratified squamous epithelium) and endocervix (the inner zone of the cervix lined by a single layer of mucus producing columnar cells) have been noted by some[5,13] and explained by differences in anatomy. Another important source of normal variations in anatomy are the dynamic changes that occur in the cervix during reproductive life, namely the process of squamous metaplasia in the transformation zone of the cervix. Here, the endocervical mucosal surface is actively replaced by squamous epithelium in the form of squamous metaplasia of the subcolumnar reserve cells.[1,21] As reserve cells differentiate into squamous cells, the cellular features change and the epithelial thickness increases. Additionally, the cervical stroma gradually loses its glandularity. Furthermore, there is a distribution of risk of disease even within the transformation zone. More severe disease is typically located close to the border between the endocervix and the transformation zone (squamo-columnar junction) where the epithelium is least mature, while the most mature metaplastic epithelium has little neoplastic potential, like that of the original squamous epithelium.[1] The normal anatomical variations between the transformation zone and ectocervix (normal squamous epithelium), as well as within transformation zone, should be reflected in tissue spectroscopy and, if significant, must be accounted for when developing diagnostic algorithms.

A small minority of squamous tissue abnormalities is found in the ectocervix, and the gynecologists sometimes sample the ectocervix. However, the vast majority of HSILs are found within the transformation zone.[1] Furthermore, normal ectocervix and endocervix are easily identified by colposcopic examination.[2] Therefore, in order to improve the accuracy of clinical HSIL detection, spectroscopy must be able to identify HSILs within the transformation zone. In order to achieve this goal, spectroscopy must be able to reliably resolve the disease process in the context of the background microanatomic complexity inherent in the cervix.

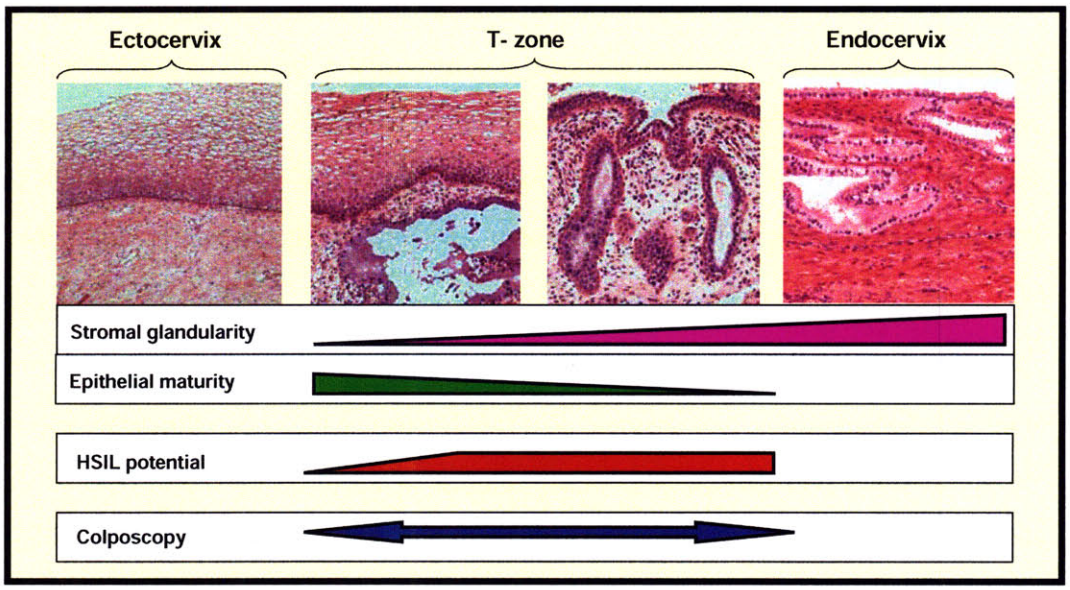

Figure 1.1.1. Clinical goal of spectroscopic studies presented in this thesis.

The goal of this thesis was to develop a real-time clinical diagnostic tool based on reflectance and fluorescence spectroscopy, which is accurate and free of confounding effect of anatomy, for detection of HSILs.

1.2 Overview of Thesis Accomplishments

Previously we have developed a contact-probe portable instrument for collection of tissue reflectance and fluorescence spectra, and spectral analysis models to extract and quantify biochemical and structural features of tissue to provide disease state assessment. The instrument developed in our laboratory, the FastEEM, was used to collect white light reflectance and fluorescence spectra in real-time via an

optical fiber probe. The three spectroscopic modalities were then used to obtain biochemical and morphological tissue information and to provide diagnosis: Intrinsic Fluorescence Spectroscopy (IFS) which provides the relative contributions of tissue biochemicals; Diffuse Reflectance Spectroscopy (DRS) which provides information about scattering and absorption properties of the stromal tissue, and Light Scattering Spectroscopy (LSS) which provides information about epithelial nuclear size distribution and density. Initial *in-vivo* pilot studies have been performed in the oral cavity, uterine cervix, colon, bladder and Barrett's esophagus.

The goal of this thesis was to develop a real-time clinical diagnostic tool based on reflectance and fluorescence spectroscopy, which is accurate and free of confounding effect of anatomy, for detection of HSILs. In order to achieve such a goal the work in this thesis was focused on: 1) clinical *in vivo* studies of cervical dysplasia, 2) instrumentation improvement, and 3) analysis model development.

During the course of clinical *in vivo* study, we have developed an understanding of the physical basis for differences in the spectroscopic parameters due to tissue anatomy and disease. We demonstrated that both normal variations in tissue anatomy and disease are major sources of spectroscopic contrast, and that it was crucial to disentangle the effects of the two in order to develop reliable diagnostic algorithms. The results of clinical *in-vivo* study showed cervical anatomy was a confounder to diagnostic algorithms that treat cervix as spectroscopically uniform. As a result we developed an accurate and site-specific algorithm for detection of HSILs in the transformation zone, an area where vast majority of cervical lesions arise. Tissue scattering alone was sufficient to identify HSIL disease within transformation zone of the cervix. We further successfully extended the contact-probe technique into the imaging mode, to provide then wide-area surveillance capability. The on-going imaging clinical *in vivo* feasibility study demonstrates spectroscopic contrast between cervical HSIL and non-HSIL tissue and is consistent with findings of the contact-probe study. The simplicity of our findings suggests that significantly simpler, faster, and less expensive cervical dysplasia system may be effective in improving cervical dysplasia detection in both developed and developing

countries. The realization of this future direction is pending on the results of the larger imaging study confirming the results obtained so far.

Instrument improvements allowed for extraction of artifact free reflectance and fluorescence data. Two sources of artifact in tissue spectra collected during the contact probe pilot studies were identified, and an instrumental method to remove this effect prospectively was implemented. A method to retrospectively remove artifact in already collected data was developed and enormous amount of valuable clinical data collected has been salvaged.

The analysis model development advance understanding of the physical basis for spectral diagnosis. We have improved our understanding of model based LSS analysis and showed that what we have initially attributed to signal from nuclear scattering (LSS signal) is actually due to changes in hemoglobin absorption due to vessel packaging phenomena.

1.3 Overview of Thesis Content

In Chapter 2 we first explain anatomy and histology of normal cervix in detail as understanding of normal anatomic variations in the cervix is crucial for the work presented in this thesis. We introduce cervical dysplasia and cancer by discussing the epidemiology, as well as the relationship of cervical pathogenesis to human papilloma virus (HPV) infections. We further explain the histopathology of cervical dysplasia. Finally, we describe the current clinical management of cervical dysplasia and cancer including screening, diagnosis, and treatment.

We begin Chapter 3 by discussing the basic principles of tissue spectroscopy and the motivation for developing using it in the clinic for cancer diagnosis. The physical basis of each of the four fundamental light-tissue interactions: elastic scattering, absorption, fluorescence, and Raman scattering, is described. We next provide an overview of the research that utilizes spectroscopic approaches for the diagnosis of cervical dysplasia disease in both contact-probe and wide-area surveillance manner. Further detail of these studies and comparison with our own findings is provided in the subsequent chapters. Finally, we discuss the basic

principles of two optical imaging techniques, confocal microscopy and optical coherence tomography, and their application for detection of cervical dysplasia.

Chapter 4 describes two instruments which were used to collect clinical data *in vivo*. First we introduce and explain in detail the hardware and the software of the contact-probe device, the Fast Excitation Emission Matrix (FastEEM) instrument. We further discuss the safety of using FastEEM instrument to conduct research involving human subjects. Finally, we introduce the Quantitative Spectroscopy Imaging (QSI) system, which is an extension of the point probe device with the wide-area surveillance capabilities.

Chapter 5 introduces Tri-Modal Spectroscopy (TMS), a technique used to provide spectral diagnosis developed in our laboratory. TMS is a combination of three spectroscopic techniques: Diffuse Reflectance Spectroscopy (DRS), Intrinsic Fluorescence Spectroscopy (IFS), and Light Scattering Spectroscopy (LSS). As will be explained in this chapter, the work presented in this thesis focuses primarily on DRS and IFS analysis. Here we provide details of DRS and IFS, as well as explain why LSS is no longer used in our data analysis. We next describe the statistical methods used in this thesis to determine the statistical significance of extracted parameters and to develop the algorithms for disease diagnosis. Finally, we explain the clinical *in vivo* study design for both contact-probe and imaging studies.

In Chapter 6 we investigate the effects of cervical tissue anatomy on reflectance and fluorescence spectroscopy measurements, with an aim to facilitate development of a diagnostic algorithm free of the confounding effects of anatomy. We present evidence that sites collected in the transformation zone, the area in which the vast majority of high grade squamous intraepithelial lesions (HSILs) are found, are spectroscopically distinct from the squamous sites, even in the absence of disease. We demonstrate that the apparent performance of diagnostic algorithms for identifying HSILs is enhanced when clinically normal squamous sites are included, as a result of normal anatomic differences. Based on findings presented in this chapter, including clinically normal squamous sites into the data set which is used to evaluate the performance of the algorithm for detection of HSIL is a confounding artifact that

artificially increases performance values with respect to the key differentiation to be made, namely distinguishing HSILs from clinically suspicious non-HSILs.

In Chapter 7 we use contact probe data to develop a spectral algorithm for detection of high grade squamous intraepithelial lesions (HSILs) free of the confounding effects of cervical anatomy. We focus on the clinically relevant issue that spectroscopy must address, namely how well HSILs can be differentiated from non-HSILs among clinically suspicious sites, majority of which are found in transformation zone. Results presented in this chapter show that the spectroscopic contrast between non-HSIL and HSIL is enhanced if parameters are normalized by an internal standard, the corresponding parameter extracted from clinically normal squamous site of the same patient. We show that the diagnostic performance of the spectroscopic algorithm developed here is superior to that of colposcopy.

In Chapter 8 we describe a pilot study in which we extend quantitative spectroscopy from contact-probe to wide-area QSI for detection of HSILs in the transformation zone. Here we present the disease related structural and biochemical changes observed by QSI. Using the observed spectroscopy changes, we construct diagnostic maps showing the locations of HSILs on patients evaluated prospectively with QSI. To construct the spectroscopy diagnostic maps, we normalize the quantitative spectroscopy measurements to reduce the effects of patient-to-patient variation and utilize the spatial continuity of disease to improve contrast between HSIL and non-HSIL sites. These maps are compared to corresponding disease maps obtained with histopathology to demonstrate the accuracy of QSI for detecting HSILs in the cervix. The results presented in this chapter show that sites identified as HSIL by QSI are in good agreement with pathology. Furthermore, the HSIL identification criteria are the same for contact-probe and wide-area imaging implementations, indicating that quantitative spectroscopy's diagnosis is independent of instrument implementation.

In Chapter 9 we investigate correlation between spectroscopy parameters and pattern of staining of two objective biomarkers for cervical dysplasia diagnosis p16 ^{INK4a} and Ki-67.

Chapter 10 discusses potential future directions, and in Chapter 11 we conclude this thesis by providing an overview of thesis accomplishments followed by the final remarks.

1.4 References

1. A. Blaustein and R. J. Kurman, *Blaustein's pathology of the female genital tract*, Springer, New York (2002)
2. D. G. Ferris, *Modern colposcopy : textbook and atlas*, Kendall/Hunt, Dubuque, Iowa (2004)
3. M. F. Mitchell, D. Schottenfeld, G. Tortolero-Luna, S. B. Cantor and R. Richards-Kortum, "Colposcopy for the diagnosis of squamous intraepithelial lesions: A meta-analysis," *Obstetrics and Gynecology* **91** (4), 626-631 (1998).
4. R. D. Alvarez, T. C. Wright and O. D. Grp, "Effective cervical neoplasia detection with a novel optical detection system: A randomized trial," *Gynecologic Oncology* **104** (2), 281-289 (2007).
5. S. K. Chang, Y. N. Mirabal, E. N. Atkinson, D. Cox, A. Malpica, M. Follen and R. Richards-Kortum, "Combined reflectance and fluorescence spectroscopy for in vivo detection of cervical pre-cancer," *Journal of Biomedical Optics* **10** (2), - (2005).
6. I. Georgakoudi, E. E. Sheets, M. G. Muller, V. Backman, C. P. Crum, K. Badizadegan, R. R. Dasari and M. S. Feld, "Trimodal spectroscopy for the detection and characterization of cervical precancers in vivo," *American Journal of Obstetrics and Gynecology* **186** (3), 374-382 (2002).
7. W. K. Huh, R. M. Cestero, F. A. Garcia, M. A. Gold, R. S. Guido, K. McIntyre-Seltman, D. M. Harper, L. Burke, S. T. Sum, R. F. Flewelling and R. D. Alvarez, "Optical detection of high-grade cervical intraepithelial neoplasia in vivo: Results of a 604-patient study," *American Journal of Obstetrics and Gynecology* **190** (5), 1249-1257 (2004).
8. N. M. Marin, A. Milbourne, H. Rhodes, T. Ehlen, D. Miller, L. Benedet, R. Richards-Kortum and M. Follen, "Diffuse reflectance patterns in cervical spectroscopy," *Gynecologic Oncology* **99** (3), S116-S120 (2005).
9. Y. N. Mirabal, S. K. Chang, E. N. Atkinson, A. Malpica, M. Follen and R. Richards-Kortum, "Reflectance spectroscopy for in vivo detection of cervical precancer," *Journal of Biomedical Optics* **7** (4), 587-594 (2002).
10. J. R. Mourant, T. J. Bocklage, T. M. Powers, H. M. Greene, K. L. Bullock, L. R. Marr-Lyon, M. H. Dorin, A. G. Waxman, M. M. Zsemlye and H. O. Smith, "In vivo light scattering measurements for detection of precancerous conditions of the cervix," *Gynecologic Oncology* **105** (2), 439-445 (2007).
11. R. J. Nordstrom, L. Burke, J. M. Niloff and J. F. Myrtle, "Identification of cervical intraepithelial neoplasia (CIN) using UV-excited fluorescence and diffuse-reflectance tissue spectroscopy," *Lasers in Surgery and Medicine* **29** (2), 118-127 (2001).
12. I. M. Orfanoudaki, G. C. Themelis, S. K. Sifakis, D. H. Fragouli, J. G. Panayiotides, E. M. Vazgiouraki and E. E. Koumantakis, "A clinical study of

optical biopsy of the uterine cervix using a multispectral imaging system," *Gynecologic Oncology* **96** (1), 119-131 (2005).

13. N. Ramanujam, M. F. Mitchell, A. Mahadevan, S. Thomsen, A. Malpica, T. Wright, N. Atkinson and R. RichardsKortum, "Development of a multivariate statistical algorithm to analyze human cervical tissue fluorescence spectra acquired in vivo," *Lasers in Surgery and Medicine* **19** (1), 46-62 (1996).
14. R. Kalluri and M. Zeisberg, "Fibroblasts in cancer," *Nature Reviews Cancer* **6** (5), 392-401 (2006).
15. H. Nagase and J. F. Woessner, "Matrix metalloproteinases," *Journal of Biological Chemistry* **274** (31), 21491-21494 (1999).
16. J. Mazibrada, M. Ritta, M. Mondini, M. De Andrea, B. Azzimonti, C. Borgogna, M. Ciotti, A. Orlando, N. Surico, L. Chiusa, S. Landolfo and M. Garigho, "Interaction between inflammation and angiogenesis during different stages of cervical carcinogenesis," *Gynecologic Oncology* **108** (1), 112-120 (2008).
17. S. K. Chang, N. Marin, M. Follen and R. Richards-Kortum, "Model-based analysis of clinical fluorescence spectroscopy for in vivo detection of cervical intraepithelial dysplasia," *Journal of Biomedical Optics* **11** (2), - (2006).
18. C. K. Brookner, M. Follen, I. Boiko, J. Galvan, S. Thomsen, A. Malpica, S. Suzuki, R. Lotan and R. Richards-Kortum, "Autofluorescence patterns in short-term cultures of normal cervical tissue," *Photochemistry and Photobiology* **71** (6), 730-736 (2000).
19. J. A. Freeberg, D. M. Serachitopol, N. McKinnon, R. Price, E. N. Atkinson, D. D. Cox, C. MacAulay, R. Richards-Korturn and M. Follen, "Fluorescence and reflectance device variability throughout the progression of a phase II clinical trial to detect and screen for cervical neoplasia using a fiber optic probe," *Journal of Biomedical Optics* **12** (3), - (2007).
20. E. M. Gill, A. Malpica, R. Richards-Kortum, M. Follen and N. Ramanujam, "Collagen autofluorescence of the human cervix and menopausal status," *Lasers in Surgery and Medicine* 12-12 (2003).
21. V. Kumar, A. K. Abbas, N. Fausto, S. L. Robbins and R. S. Cotran, *Robbins and Cotran pathologic basis of disease*, Elsevier Saunders, Philadelphia (2005)

CHAPTER 2

The Cervix: Anatomy, Histology, and Pathology

In this chapter we first explain anatomy and histology of normal cervix in detail as understating of normal anatomic variations in the cervix is crucial for the work presented in this thesis. We introduce cervical dysplasia and cancer by discussing the epidemiology, as well as the relationship of cervical pathogenesis to human papilloma virus (HPV) infections. We further explain the histopathology of cervical dysplasia. Finally, we describe the current clinical management of cervical dysplasia and cancer including primary prevention, screening, diagnosis, and treatment.

2.1 Anatomy and Histology of the Cervix

2.1.1 Gross Anatomy

The uterus is divided into the corpus, isthmus, and cervix. The cervix (Latin word for *neck*) is an inferior extension of the uterus which connects the corpus of the uterus with the vagina.[1] It is characterized by a thick muscular wall and constricted lumen, or cervical canal. In mature women the cervix is approximately 3 cm long and 2 cm wide. The centrally located cervical os, an opening to the cervical canal, is circular (3-5 mm in diameter) in nulligravida and slitlike in parous women. The cervical canal is lined by mucus secreting cells which protects against bacterial infections and either aid or prevents the sperm transport from vagina to uterus, depending on the stage of the reproductive cycle. Blood supply of the cervix includes descending branches of the uterine arteries. Venous drainage parallels the arterial supply. Sensory nerves arise from the cervical canal only, and are relatively scarce in the outer portion of the cervix, or ectocervix. This distribution of innervation is responsible for the relative insensitivity of the ectocervix to pain.

2.1.2 Histology of Normal Cervix

The cervix is divided into three distinct histological zones: ectocervix, endocervix, and the transformation zone.

2.1.2.i Ectocervix

Ectocervix, the outer portion of the cervix, is covered by non-keratinizing stratified squamous epithelium. The epithelium consists of the single layer of stem cells, called basal layer, one or few layers of parabasal cells, an intermediate layer consisting of cells rich in glycogen, and a superficial layer of flat cells. Basal cell layer functions as a germinal layer of the squamous epithelium. These small cells (~10 μm diameter) contain large oval nuclei, scant cytoplasm, and have occasional mitotic figures. Parabasal cells are irregular polyhedral cells with large oval nuclei and visible nucleoli. Unlike basal layer cells, parabasal cells posses certain degree of squamous differentiation. The intermediate layer consists of flattened cells with small and round nuclei, and glycogen rich cytoplasm. These cells, which comprise

majority of squamous cells, undergo maturation and do not divide. The superficial layer is composed of terminally differentiated cells. These cells are flattened and have small pyknotic nuclei. The thickness of the ectocervical epithelium is influenced by hormones estrogen and progesterone, and therefore varies with age and menstrual cycle.

The ectocervical stroma is composed of fibrous connective tissue, devoid of glands. The superficial stroma contains reticular capillary network. Straight vessel loops branch from the capillary network and extend into basal and parabasal layers of the squamous epithelium to supply epithelial cells with nutrients and oxygen. The photograph of hematoxylin & eosin (H&E) stained tissue section of the ectocervix can be appreciated in Figure 2.1.1.(a).

2.1.2.ii Endocervix

Cervical canal, or endocervix, is lined by a single layer of mucus-producing columnar cells. The nuclei of these cells are oval in shape and basally placed. The majority of endocervical epithelial cells contain cytoplasm with mucinous droplets and a few of them are ciliated. Unlike the ectocervical stroma, the endocervical stroma is abundant with "cervical glands". These cervical glands are not true glandular structures, since they are actually mucus-producing tubules lined by the same type of the epithelium that lines the surface. They are loosely arranged in a fibrous stroma. In the endocervix the small capillary loops are located directly beneath the columnar cells. The photograph of H&E stained tissue section of the endocervix can be appreciated in Figure 2.1.1.(b).

2.1.2.iii The Transformation Zone (T-zone)

The transformation zone is an area where the endocervical mucosal surface is actively replaced by squamous epithelium typically by the process of squamous metaplasia of the subcolumnar reserve cells.[1,2] Squamous metaplasia is a normal process occurring in most women during the reproductive period. At the time of menarche both the uterus and the cervix enlarge under the influence of hormonal factors. The enlargement results in eversion of endocervical columnar epithelium to the outer portion of the cervix. Over time, the fragile columnar epithelium is replaced

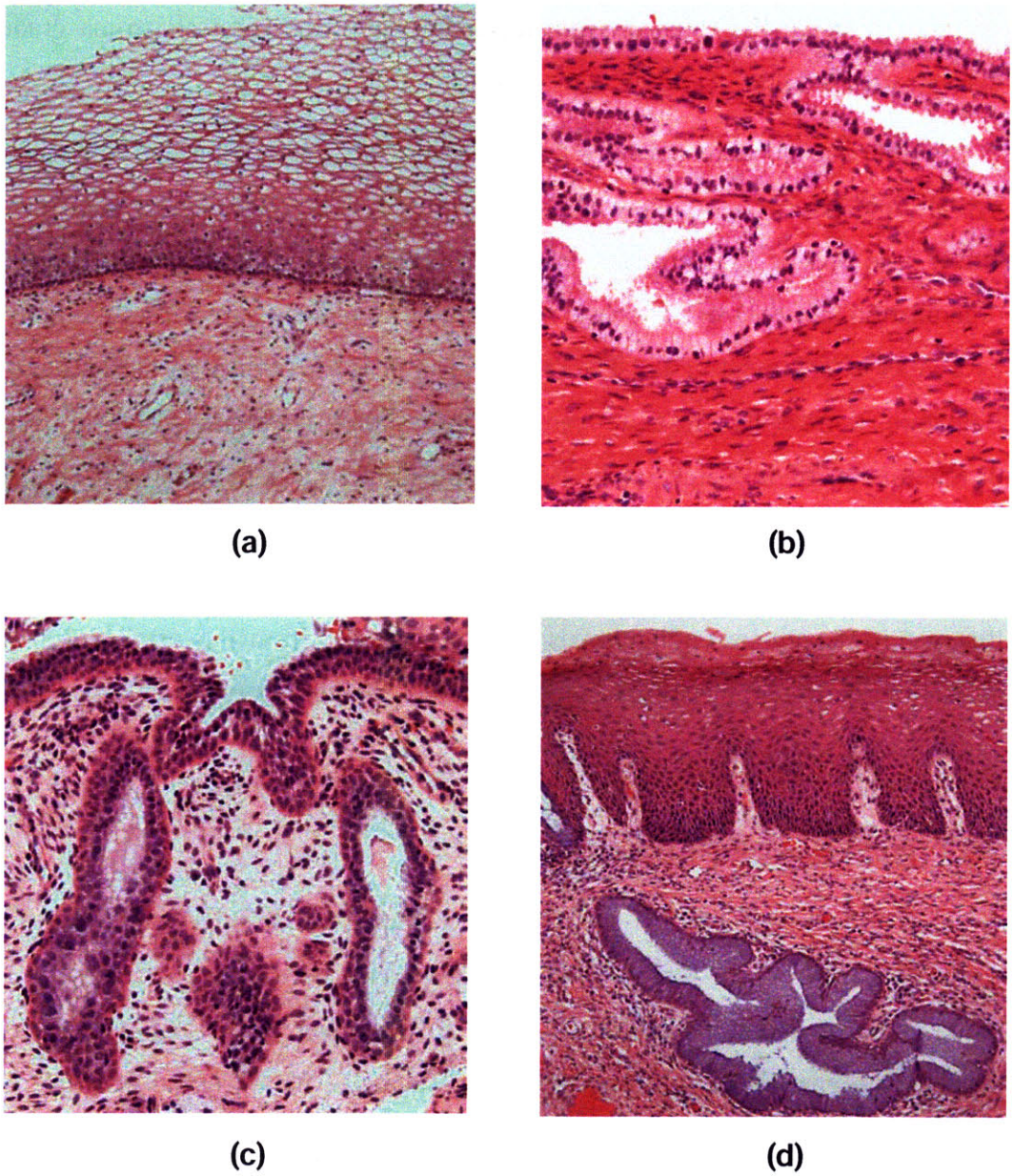

Figure 2.1.1. Histology of the normal cervix: (a) Ectocervix, (b) Endocervix (c) Transformation zone: immature squamous metaplasia (hyperplasia of the reserve cells), and (d) Transformation zone: mature squamous metaplasia

by squamous epithelium. The first stage of squamous metaplasia is the appearance and expansion of reserve cells beneath the columnar epithelium. The origin of these cells is not well understood. The reserve cells have large, uniformly shaped, round nuclei, scant cytoplasm and poorly defined borders. The reserve cell hyperplasia, or expansion, is followed by squamous differentiation. As reserve cells differentiate, first into the immature, and then mature squamous cells, the cellular features change

and the epithelial thickness increases. Additionally, the cervical stroma gradually loses its glandularity.

Immature squamous metaplasia lacks surface maturation and abundance of cytoplasmic glycogen, and may be easily confused with cervical dysplasia. However, unlike the cervical dysplasia, immature squamous epithelium maintains cell organization and cohesion, nuclear abnormalities are absent, and it is often covered by a layer of columnar cells. The photographs of H&E stained tissue section of the immature transformation zone can be appreciated in Figure 2.1.1.(c). Further differentiation of immature metaplastic epithelium results in squamous epithelium indistinguishable from the original squamous epithelium. The Figure 2.1.1.(d) shows a photograph of H&E stained tissue section of the mature transformation zone. Here, the mature squamous epithelium is indistinguishable from the original squamous epithelium; however, the stroma contains residual glandular structures.

2.2 Cervical Pathology

2.2.1 Epidemiology of Cervical Cancer

Cervical cancer is the second most common cancer in women, in whom it comprises 12% of all cancers (437,600 new cases per year).[3] It is much more common in developing countries, where 78% of cases occur and where cervical cancer represents 15% of all cancers. In sub-Saharan Africa, Central America, South Central Asia, and Melanesia it is still remains the main cancer in women.[4] The discrepancy in cervical cancer distribution is largely due to the establishment of cervical cancer prevention programs in developed countries, which are essentially non-existent in many developing countries.

In the United States and developed countries, the fatalities due to cervical cancer have been greatly reduced. Both the incidence and mortality have decreased by 75% since the implementation of Papanicolaou smear screening in 1950's.[3] According to National Cancer Institute Surveillance, Epidemiology, and End Results Program (NCI SEER) statistics estimated new cases of cervical cancer and estimated deaths in the US for year 2007 are 11,150 and 3,670 respectively.[5]

The human papilloma virus (HPV) infection is a necessary factor for development of cervical dysplasia and cancer and can be detected in 99.7 % of cervical cancers.[6] The risk factors for development of cervical dysplasia and cancer include early onset of sexual activity, multiple sexual partners, a high-risk sexual partner, history of sexually transmitted diseases, smoking, high parity, immunosuppression, low socioeconomic status, prolonged use of oral contraceptives, and previous history of vulvar or vaginal squamous dysplasia.[3] These factors most likely represent surrogate markers for increased sexual exposure and risk of exposure to HPV. Furthermore, as it is the long-term persistence of HPV infection that is required for the development of invasive cancer, cofactors such as smoking and immunosuppression potentially act by impairing the ability of the immune system to suppress or eliminate HPV infection.

2.2.2 Human Papilloma Virus Infection

HPV is a small virus characterized by a double-stranded, circular DNA, non-enveloped virion encased in a protein capsid.[7] Presently, there are over 100 known HPV types, each of which is highly trophic for specific epithelium. HPV infections occur on the skin and mucous membranes, on the conjunctiva, oral cavity, larynx, tracheobrachial tree, esophagus, bladder, anus, and genital tract of both sexes.[1] More than 40 HPV types have been isolated from the anogenital tract. According to the degree of oncogenicity, the anogenital HPV type may be either high-risk or low-risk. High-risk group causes cervical and anal dysplasia, and includes HPV types 16, 18, 31, 33, 35, 39, 45, 51, 52, 56, 58, 59, and 68. The low-risk types, such as HPV 6, 11, 42, and 44, typically cause benign clinical lesions (e.g. condyloma acuminatum or flat warts).[4] The most common type detected in both high grade squamous intraepithelial lesions (HSILs) and invasive cancers is HPV 16, which is found in over 50% of squamous intraepithelial lesions (SILs) and invasive cancers.[4,8]

An infection by high-risk HPV type represents a necessary but not sufficient risk factor for cervical dysplasia. The infection by HPV is usually self-limited and transient. It is estimated that the cumulative risk of such infections in 70 years of a women's life is more than 70%. However, only very few women will ever develop a

persistent infection leading to development of cervical lesions. The cells of the transformation zone are particularly prone to infections by HPV. Presumably, transformation zone cells contain receptors targeted by the HPV, but this process is not completely understood. The HPV requires access to the basal and parabasal cell layers of the transformation zone epithelium to establish the infection. The latent infection produces no cytopathic effects or epithelial morphologic abnormalities, since HPV DNA only resides in the basal cells and infectious virions are not produced. If a productive viral infection is established, large quantities of virions are formed. This produces the cytophatic effects of HPV characteristic for the low grade lesions- such as koilocytosis and nuclear atypia and cytoplasmic vacuolization. Replication and production of new infectious virions occurs only in the intermediate epithelial layer, and not in the basal/parabasal layers, as this process requires a certain degree of epithelial cell differentiation. Since intermediate cells are determined to die, the viral infection causes almost no damage to the infected host.

The cervical high grade lesions and ultimately cancer develop as a consequence of uncontrolled viral replication in the basal and parabasal epithelial layers, which is relatively rare event.[4] Imbalance in the expression of the viral E6 and E7 genes is crucial in oncogenesis. The E6 protein supports premature degradation of the cellular p53 tumor suppressor gene and thus interferes with apoptotic function of the host cell. The E7 protein induces destabilization of the retinoblastoma protein (Rb) complex and thus allows the cell to evade cell cycle control. Interference of viral genes with pathways involved in the replication of the epithelial cell and life cycle leads to chromosomal instability, which eventually leads to cancer.

2.2.3 Histopathology of the Cervix

Histopathology of the cervix includes benign diseases (cervicitis, hyperplasia, benign tumors, and cysts), as well as the dysplastic and cancerous lesions. Cervical dysplasia includes squamous intraepithelial lesions, as well as the lesions of glandular origin, or precursors of adenocarcinomas, which are confined to the endocervix. Here we describe histology of common squamous tissue abnormalities.

2.2.3.i Reactive and reparative changes

Acute, or more frequently, chronic inflammation is a common feature that accompanies squamous metaplasia. The superficial stroma may contain lymphoid follicles and depending on the degree of inflammation, the surface epithelium can erode. The eroded epithelium is replaced by immature metaplastic squamous cells through a process known as repair. Reactive epithelia are characterized by nuclear atypia and epithelial disorganization and, thus, are often confused with dysplastic lesions. Reactive changes can be distinguished from squamous dysplasia by the presence of smooth nuclear borders, uniform nuclear size and shape, presence of distinct cell borders, and mitotic figures found only along the basal cell layer.

2.2.3.ii Squamous Intraepithelial Lesions (SILs)

Cervical SILs are defined as squamous alterations in the cervical transformation zone that are induced by HPV infection.[8] SILs are characterized by cellular atypia, abnormal cellular proliferation, and progressive loss of differentiation. Cellular atypia that accompany precancerous progression typically include nuclear enlargement and hyperchromasia, variations in nuclear size and shape, and nuclear membrane irregularity. The presence of mitotic figures outside of the basal and parabasal cellular layer is common. The decrease in glycogenation of epithelial cells is also common, and consistent with loss of differentiation. According to the extent of epithelial nuclear abnormalities, SILs are divided into two categories: low grade (LSIL) and high grade (HSIL) SILs. Alternatively, squamous lesions in the cervix may be termed cervical intraepithelial neoplasia (CIN). CIN terminology is based on the concept that all types of precursor lesions to squamous cell carcinoma represent a single disease process. However, it is now understood that this basic premise underlying the CIN terminology is incorrect. The changes that are referred to as CIN do not represent a histologic and cytologic continuum in disease development, but instead two distinct biologic entities, LSIL and HSIL. LSILs are typically caused by a productive viral infection. They are associated with multiple HPV types and exhibit polyploidy. These lesions are usually self-limited and regress spontaneously. Unlike LSILs, HSILs are associated with a limited number of high-risk HPV types, they are monoclonal, frequently aneuploid, and have a potential to progress to invasive squamous cell carcinoma if left untreated. For reference, the LSIL is equivalent to

flat condyloma, exophytic condyloma and CIN I, while HSIL encompasses CIN II and CIN III/carcinoma *in situ*. We employ the two-tier type of diagnostic terminology throughout the thesis.

LSIL. Hallmark cell of LSIL is a koilocyte. Koilocytosis is a process of degeneration of a mature squamous cell due to production and accumulation of new HPV virions within the cell. Koilocytes are located in upper two thirds of the squamous epithelium, and characterized by superficial or intermediated cells with enlarged, raisin-like nuclei. Electron microscopic imaging of koilocytes indicates that the nuclei are filled with numerous encapsulated HPV virions. The area adjacent to the nucleus appears transparent – perinuclear halo. The cytoplasm alterations represent aggregation of cytoskeleton filament and organelles into the periphery. At the base there are signs of abnormal cell proliferation. The degree of basal and parabasal cell proliferation is limited to the lower third of the epithelium. The mitotic figures are limited to the layer of proliferation.

HSIL. The degree of proliferation of basal and parabasal cells increases to above the lower third of the epithelium. Mitotic figures may extend to the top of the epithelial surface. Koilocytes may be found in the upper portion of the epithelial surface.

Invasive cancer. Invasive cancer is characterized by disruption of the basement membrane between the epithelial surface cells and the underlying stroma.

The histopathology classification presented above represents traditional classification. It is, however, important to note that differences in the differentiation level or pathway of the underlying mucosa may influence the morphologic presentation of cervical lesions, leading to additional patterns not accounted for in traditional classifications. We limit the discussion to traditional classification, and refer the reader to advanced literature for further detail.[8]

2.2.3.iii Transformation zone and Pathogenesis

The concept of the transformation zone is extremely important for understanding the pathogenesis of cervical dysplasia and cancer. Since transformation zone cells are particularly prone to infections by HPV, the vast

majority of all SIL are located within the transformation zone. Virtually all SIL begin at or near squamo-columnar junction. Furthermore, distribution of HSIL risk varies with location within transformation zone. More severe disease is typically located close to the squamo-columnar junction, where the epithelium is least mature. Most mature metaplastic epithelium has little neoplastic potential, like that of the original squamous epithelium.

2.2.4 Clinical Management of Cervical Dysplasia

Secondary prevention of cervical cancer in the United States and developed countries includes yearly screening by cervical exfoliative cytology (Pap smear test), followed by diagnostic test (colposcopy and biopsy) if necessary, and treatment if indicated by the diagnostic test. Almost 60 million Pap tests are performed in the US each year. Approximately 3.5 million of these are abnormal, and an estimated 2.5 million women undergo diagnostic colposcopy.[9] Recently a vaccine for protection against HPV infections have been developed.

2.2.4.i Screening

The concept of exfoliative cytology for detection of cervical dysplasia was invented in the 1930's independently by a Romanian physician Aurel Babes and Greek zoologist Georgios Papanicolaou. The cervical cells of the transformation zone are stained and examined under the microscope for changes consistent with dysplasia or cancer. However, Dr. Papanicolaou's publication *Diagnosis of Uterine Cancer by the Vaginal Smear* in the 1943 impacted the medical community and led the way to establishing cervical exfoliative cytology as method of screening for cervical cancer. Since the early 1950's cervical screening with Papnicoulaou (Pap) smear gained acceptance in the United States, and is responsible for 75 % reduction in incidence and mortality of cervical cancer.[4] We note, however, that Pap smear is not a perfect screening test. The studies that evaluated the performance of Pap smear report sensitivities and specificities ranged from 30% to 87%, and from 86% to 100%, respectively. [10]

Abnormal Pap smear includes several categories: atypical squamous cell of undetermined significance (ASC-US), atypical squamous cells cannot exclude HSIL

(ASC-H), low-grade squamous intraepithelial lesion (LSIL), high-grade squamous intraepithelial lesion (HSIL), atypical glandular cells (AGC), and adenocarcinoma in situ (AIS), all of which are indications for a diagnostic test, colposcopy.[3]

2.2.4.ii Diagnosis

In case of the positive screening test, a diagnostic test called colposcopy is performed. The colposcopy involves examination of the cervix under the low-power microscope, after the application of acetic acid. Colposcopy was invented in the 1930's and is still in use today.

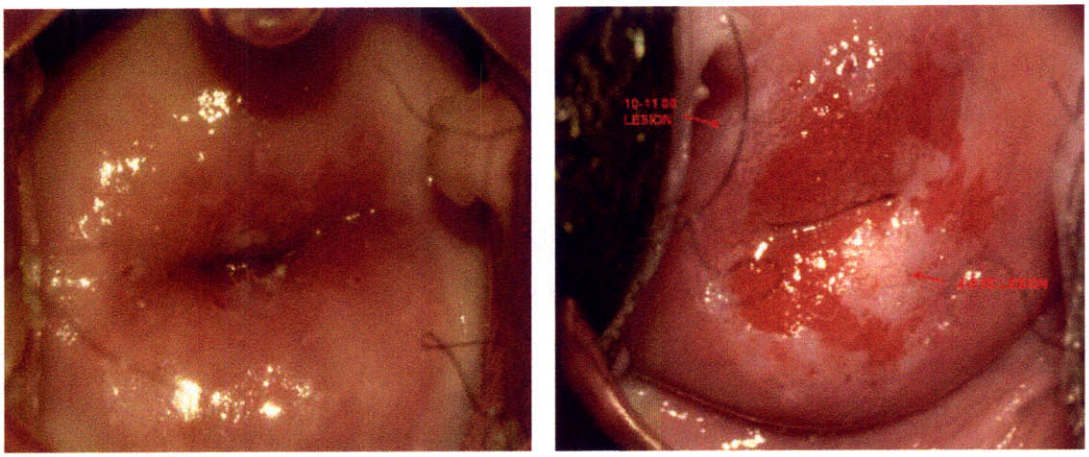

Figure 2.2.1. Colposcopy picture of: (a) normal cervix and (b) abnormal cervix with two acetowhite lesions in the transformation zone.

Recognition of abnormalities within the transformation zone is the most critical objective of colposcopy.[3] The epithelial and vascular characteristics such as epithelial color, vessel pattern, caliber, and intercapillary distances, the surface topography (flat, ulcerated, raised), and margin characteristics are examined before and after the application of 3-5% acetic acid. The size, shape, location and extent of cervical lesions are determined by visual assessment, which is followed by histological sampling (biopsy) of most abnormal-appearing areas of the cervix.

Acetowhite epithelium is the most common feature associated with cervical dysplasia. It refers to epithelium that transiently changes color from pink or red to white after the application of 3-5 % acetic acid. The reasons for acetowhitening are not well understood. Even though acetic acid is used as a stain for guiding biopsy,

acetowhitening is not specific to neoplastic changes. Immature metaplastic as well as reparative epithelium also exhibit acetowhitening effect. However, acetowhite color observed in regions of high-grade lesions and cancer is usually more intense and more persistent than color seen in regions of low-grade lesions and metaplasia.[3]

2.2.4.ii Treatment

Women with biopsy-confirmed LSIL are usually managed by a follow-up without treatment. The reasons for expectant management of LSILs are twofold. Not only do the LSIL exhibit high regression rates, but the accuracy of LSIL diagnosis is a subject to high inter-observer disagreement.[4] In contrast, the majority of women with biopsy-confirmed HSIL are treated. Thus, in our studies, we strive to use spectroscopy to diagnose HSIL.

The common techniques for treatment of cervical dysplasia are surgical ablative methods, such as cryotherapy and CO_2 laser ablation, and surgical excisional methods, such as Loop electrosurgical excision procedure (LEEP), and cold knife conization. In the US, LEEP is a procedure of choice for treatment of cervical dysplasia. It refers to excision of tissue by an electrified wire loop. High frequency alternating current (350 to 750 kHz) is used to vaporize abnormal tissue. [3]

2.2.4.ii Primary Prevention: HPV Vaccine

On June 8, 2006, the U.S. Food and Drug Administration approved quadrivalent HPV (Types 6, 11, 16, 18) recombinant vaccine (Gardasil, Merck & Co., Inc.) for vaccination of females 9 to 26 years of age.[11] This well tolerated and highly effective vaccine is now available for use and distribution.

The major component of the HPV vaccine is the HPV L1 major capsid protein, which self-assembles into virus-like particles (VLPs).[4] Preclinical research demonstrated that L1 is highly immunogenic. Multicenter clinical trials for HPV vaccines demonstrated efficacy against incident and persistent HPV infection and abnormal cervical cytology and histology.

The significant reduction in the prevalence of cervical abnormalities is expected in the next 20 years due to the establishment of HPV vaccination.[4]

However, the impact of HPV vaccination remains to be seen, as there are numerous questions related to implementation and success of the HPV vaccination to be answered. Duration of protection is unknown, as follow-up studies is currently limited to only four years. The minimum protective antibody titer is not known. Furthermore, the benefit of vaccination of immunocompromised patients, such as those with HIV infection, autoimmune disorders, or those receiving immunosupression therapy is unlikely. Therefore, it is not expected that necessity of cervical cancer screening and diagnosis will cease to exist in near future.

2.3 References

1. A. Blaustein and R. J. Kurman, *Blaustein's pathology of the female genital tract*, Springer, New York (2002)
2. V. Kumar, A. K. Abbas, N. Fausto, S. L. Robbins and R. S. Cotran, *Robbins and Cotran pathologic basis of disease*, Elsevier Saunders, Philadelphia (2005)
3. D. G. Ferris, *Modern colposcopy : textbook and atlas*, Kendall/Hunt, Dubuque, Iowa (2004)
4. J. Monsonégo, *Emerging issues on HPV infections : from science to practice*, Karger, Basel ; New York (2006)
5. A. Milbourne, S. Y. Park, J. L. Benedet, D. Miller, T. Ehlen, H. Rhodes, A. Malpica, J. Matisic, D. Van Niekirk, E. N. Atkinson, N. Hadad, N. MacKinnon, C. MacAulay, R. Richards-Kortum and M. Follen, "Results of a pilot study of multispectral digital colposcopy for the in vivo detection of cervical intraepithelial neoplasia," *Gynecologic Oncology* **99** (3), S67-S75 (2005).
6. J. M. M. Walboomers, M. V. Jacobs, M. M. Manos, F. X. Bosch, J. A. Kummer, K. V. Shah, P. J. F. Snijders, J. Peto, C. J. L. M. Meijer and N. Munoz, "Human papillomavirus is a necessary cause of invasive cervical cancer worldwide," *Journal of Pathology* **189** (1), 12-19 (1999).
7. M. Schaechter, *Mechanisms of microbial disease*, Williams & Wilkins, Baltimore (1998)
8. C. P. Crum, *Diagnostic Gynecologic and Obstetrics Pathology*, Elsevier Saunders, (2006)
9. B. E. Sirovich, S. Feldman and A. Goodman, *Screning for cervical cancer. In: UpToDate*, UpToDate, Waltham, MA, (2008)
10. K. Nanda, D. C. McCrory, E. R. Myers, L. A. Bastian, V. Hasselblad, J. D. Hickey and D. B. Matchar, "Accuracy of the Papanicolaou test in screening for and follow-up of cervical cytologic abnormalities: A systematic review," *Annals of Internal Medicine* **132** (10), 810-819 (2000).
11. R. A. Drezek, R. Richards-Kortum, M. A. Brewer, M. S. Feld, C. Pitris, A. Ferenczy, M. L. Faupel and M. Follen, "Optical imaging of the cervix," *Cancer* **98** (9), 2015-2027 (2003).

CHAPTER 3

Optical Techniques for Detection of Cervical Dysplasia

We begin this chapter by discussing the basic principles of tissue spectroscopy and the motivation for using it in the clinic for cancer diagnosis. The physical basis of each of the four fundamental light-tissue interactions: elastic scattering, absorption, fluorescence, and Raman scattering, is described. We next provide an overview of the research that utilizes spectroscopic approaches for diagnosis of cervical dysplasia in both contact-probe and wide-area surveillance manner. Further detail of these studies and comparison with our own findings will be provided in the subsequent chapters. Finally, we discuss the basic principles of two optical imaging techniques, confocal microscopy and optical coherence tomography, and their application for detection of cervical dysplasia.

3.1 Spectroscopic techniques for tissue diagnostics

Optical techniques are emerging as a promising new addition to widely used medical imaging modalities such as X-ray radiography, ultrasound imaging, X-ray computed tomography (CT), and magnetic resonance imaging (MRI). The major advantages of the optical techniques, and here we will focus particularly on spectroscopy techniques, is that the diagnostic information can be obtained non-invasively, without exposure to radiation, in real-time, and in an objective and quantitative manner.

Information contained in tissue spectra is based on light-tissue interactions, which depend upon the structural and biochemical composition of tissue. Endogenous properties of cervical tissue change as it progresses from the normal state through dysplasia to cancer. These changes include loss of differentiation and increased metabolic rate of the epithelial cells[1], nuclear abnormalities, degradation and reorganization of stromal collagen by matrix metalloproteinase activity[2,3], and angiogenesis[4]. There changes are manifested in the absorption, elastic and inelastic scattering, and fluorescence spectra of the tissue. Therefore, spectroscopy may be developed to provide detailed morphological and biochemical information about lesions without tissue removal, thus providing a "spectral diagnosis." Here we discuss physical basis of each of these four fundamental light-tissue interactions: elastic scattering, absorption, fluorescence, and Raman scattering.

3.1.1 Absorption

Molecules and atoms can absorb incident light, converting the light's energy into internal energy and ultimately, heat. The energy of visible and ultraviolet (UV) light can elevate the electrons in molecules and atoms to excited energy states. These energy states exist as discrete levels, and can be excited only by photons of a frequency that corresponds to that energy level (Figure 3.1.1.). The structure of the molecule determines which incident frequencies will be absorbed. For example, hemoglobin, pigment contained in red blood cells, strongly absorbs blue light. Thus, the blue component will be removed from a beam of white light diffusely reflected from tissue containing hemoglobin, resulting in its characteristic red color.

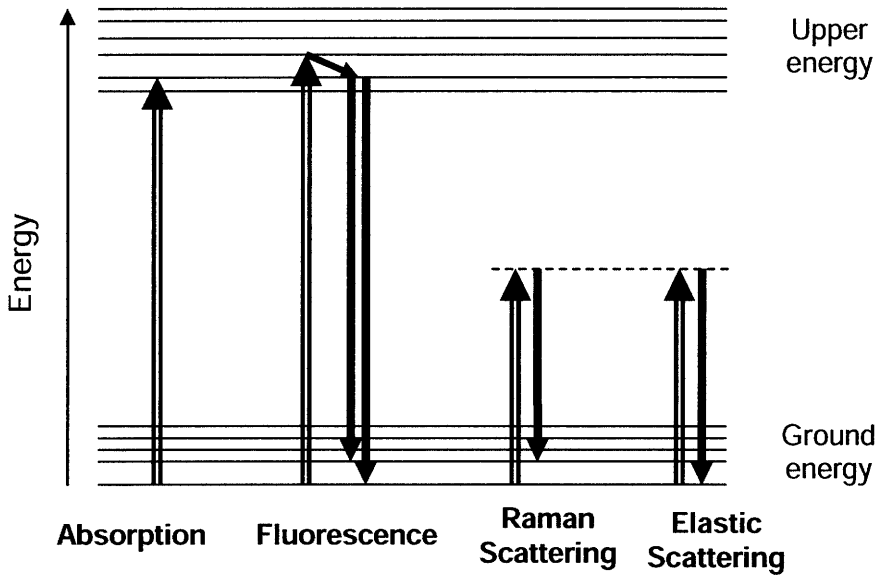

Figure 3.1.1. Fundamental light-tissue interactions. An incident ray that is transmitted into the tissue can interact with molecules in several different ways. The light may be elastically scattered, emerging with the same wavelength as the incident beam and providing information about the morphological structure of the scatterers in the tissue. It may be absorbed and either converted into internal energy or re-emitted as fluorescence. Monitoring this interaction provides chemical information about the chromophores and fluorophores in the tissue. The light can also undergo Raman scattering, transferring part of its energy to the scattering molecule and emerging with a longer wavelength.

The absorption spectrum of tissue depends on the type of predominant absorbing molecules or chromophores and therefore, provides information about its chemical composition. Common tissue chromophores absorb in the UV, visible and IR wavelength regions. Water is a strong tissue absorber in both the UV and IR regions. DNA and proteins absorb in the UV region, while hemoglobin, melanin and β-carotene absorb in the visible region. Other tissue chromophores include porphyrin-like structures such as bilirubin, myoglobin, cytochrome c oxidase and protoporphyrin. Light is readily absorbed in the UV and infrared regions and thus, is

able to penetrate only one or two cell layers deep into the tissue. Visible light of short wavelengths typically penetrates to a depth of 0.5-2.5 mm.[6] In the wavelength region of 600-1500 nm, known as the diagnostic window, scattering prevails over absorption, and light can penetrate as deep as 8-10 mm.[6]

Absorption-based techniques are widely used for the purpose of evaluating tissue oxygenation. For example, hemoglobin absorption spectra change with oxygenation. Oxyhemoglobin has a strong absorption peak in the blue region at 415 nm and a smaller double peak at 542 nm and 577 nm, while deoxyhemoglobin has a strong peak at 430 nm and a single peak at 560 nm. The pulse oxymeter is based on measuring these spectral changes in absorption of hemoglobin with various degrees of oxygenation.[7]

3.1.2 Elastic scattering

An elastic scattering event redirects an incident light photon without changing its energy. Elastic scattering is a ubiquitous feature of spectroscopy of biological tissues. It arises from both extracellular microstructures, such as collagen fiber network, as well as intracellular structures such as nuclei, mitochondria, lysosomes, and other organelles which are small compared to the wavelength of light.[5] The properties of the scattered light depend on the density of scattering particles, the particle size, and the ratio of the refractive indices of the particles relative to the medium.

Light emerging from the tissue surface can be scattered either once (single scattering) or many times (multiple scattering). Single scattered light results mainly from scattering from the cell nuclei within the epithelium. Multiple scattering is the dominant light-tissue interaction, is said to be diffusely reflected, and it is responsible for the turbid appearance of biological tissue. Diffusely reflected light generally contains information about scattering structures deeper within the tissue, such as stromal collagen matrix, since multiple scattered light typically penetrates several millimeters into the tissue.

3.1.3 Fluorescence spectroscopy

In many cases light absorbed by a molecule is converted into heat; however, an absorbed photon can also be re-emitted as fluorescence. Fluorescence emission occurs at a lower energy (longer wavelength) than the absorption energy of the incident photons (Figure 3.1.1.). The difference in wavelength between the incident light and fluorescence is known as the Stokes shift. Fluorescence is more dominant in the UV than in the IR.

The main endogenous tissue fluorophores include metabolic substances such as the reduced form of nicotinamide adenine dinucleotide (phosphate) NAD(P)H and flavins, aromatic amino acid tryptophan, the structural protein collagen, and porphyrins. Fluorescence excitation and emission spectra in tissue can be used to identify fluorophores and monitor their concentrations.

The fluorescence emitted by a molecule in tissue depends on the energy level difference between the electronic ground state and excited state and the distribution of vibrational and rotational levels within these states (Figure 3.1.1.). These states can shift in the presence of different local environmental factors, such as pH, temperature, oxygenation, and nearby chromophores with which energy transfer, complex formation, or reactions can occur.[5] In the progression of disease the local environment in which the fluorophores are embedded can change, as well as their relative concentrations, thus leading to changes in the observed fluorescence intensity and lineshape.

3.1.5 Raman spectroscopy

Raman spectroscopy is a technique that measures the frequency shift and intensity of light inelastically scattered from molecules. As discussed earlier, in elastic scattering the energy of the scattered photon is the same as that of the incident photon. In inelastic scattering, by contrast, a portion of the energy of the incident light is converted to internal energy of the scattering molecule. Hence, the energy of the scattered photon is reduced. In Raman scattering, a specific form of inelastic scattering important in probing biological tissue, the internal energy process is molecular vibration. The incident wave sets the molecule into motion, and the energy

of the scattered photons is reduced by this amount of energy. This change in energy manifests itself as a *shift* in frequency, which corresponds to the transfer of energy to or from the sample's vibrational or rotational modes. The intensity pattern of the scattered light produces a "fingerprint" of the scattering molecule. In the Raman effect spectral information is encoded as frequency shifts in the scattered light; every molecule has its own distinct set of vibrations, hence its own characteristic frequency shifts. Raman frequency *shifts* are always the same, regardless of the wavelength of the incident light. This gives an important degree of flexibility in generating a Raman spectrum; UV, visible or infrared excitation light can all be used, and in each case the Raman fingerprints will be the same. The incident wavelength can thus be tailored to the specific application, in contrast to many spectroscopic techniques.

Because each molecule possesses a unique pattern of Raman shifts, the molecular composition of the tissue can be determined via Raman spectroscopy. Further, unlike fluorescence, reflectance, and absorption spectroscopies, Raman spectroscopy provides narrow spectral bands, with high information content, that can be assigned to specific molecular vibrations.

3.1.5 Spectroscopic techniques for detection of cervical dysplasia

The effectiveness of spectroscopy, particularly reflectance and fluorescence spectroscopy, for non-invasive *in vivo* diagnosis of cervical dysplasia has been extensively evaluated. Contact probes, as well as imaging techniques with wide-area surveillance capabilities, have been tested in various stages of clinical studies, from pilot to phase III clinical studies.[6-15] The results show the potential of reflectance and fluorescence spectroscopy, individually or in combination, to guide biopsy during colposcopic examination to improve the accuracy of disease detection.

Higher hemoglobin concentration in HSIL sites compared to other tissue types has been noted by Chang et al.[16] Marin et al.[10] report that hemoglobin features of the reflectance tissue spectra are more prominent in abnormal tissue compared to normal squamous tissue. Studies that considered diagnosing HSIL within clinically suspicious sites only, such as Georgakoudi et al.[8], as well as Mourant et al.[12] reported no significant change in the hemoglobin concentration between HSIL and non-HSILs.

In a study of 161 patients, Mirabal et al.[11] found that there is a gradual decrease in mean reflectance intensity as the severity of cervical dysplasia increases. It is unknown, however, if higher hemoglobin concentration, lower scattering, or a combination of both is responsible for such a trend. This observation is consistent with the study of Arifler et al.[17], who used Monte Carlo modeling of cervical tissue to show that the decreased value of the stromal reduced scattering coefficient is the major cause for decreased reflectance intensity of HSIL compared to normal squamous tissue. Georgakoudi et al.[8] also report lower reduced scattering coefficient for SILs vs. biopsied non-SILs.

Increased NADH contribution of SILs compared to non-SILs within the transformation zone has been observed by Georgakoudi et al.[8] Chang et. al[16] report a decreased stromal collagen contribution.. Studies by Nordstrom[13], and Huh[9], which utilize 340 nm fluorescence, reported no significant differences between HSIL and normal sites in the transformation zone (squamous metaplasia). A study of Ramanujam et al. reported that 340 nm excitation HSIL sites could not be differentiated from non-HSIL sites in the transformation zone (cervical intraepithelial neoplasia 2/3 (equivalent to HSIL) vs. squamous metaplasia).

Previous efforts have been made to combine spectroscopy with imaging, particularly in the cervix[18-22], to enable wide-area diagnosis as is done in colposcopy. Milbourne *et al.* and Park *et al.* conducted three color reflectance and fluorescence spectroscopic imaging and observed that dysplastic cervical tissue emits at a slightly different wavelength than normal cervical tissue when excited with ultraviolet or blue excitation light. A study by Alvarez et al describes results of a large multicenter two-arm randomized trial comparing the effectiveness of colposcopy alone with colposcopy and a optical detection system (ODS), a method based on white light tissue reflectance, fluorescence and cervical video imaging. The result of the study shows that the use of ODS in conjunction with colposcopy increased the true positive rate for detection of CIN2,3 in women with ASC and LSIL referral cytology by 26.5% and is claimed to be clinically significant. The use of the ODS did not improve detection of CIN2,3 in women with HSIL referral cytology. The great strength of the study was the involvement of impressive number of patients to help

strengthen the conclusion that optical information obtained by ODS was contributing significantly to diagnosis of CIN2,3 lesions.

The work presented in this thesis differs from the work presented above in two ways: 1) we investigate the effects of cervical tissue anatomy, specifically epithelial tissue type and glandular composition of cervical stroma, on spectroscopy and develop a diagnostic algorithm free of the confounding effect of cervical anatomy, and 2) we develop an imaging system with wide-area surveillance which measures tissue properties by using physical models of light propagation to extract information about tissue scatterers, absorbers, and fluorophores from the measured spectra.

3.2 Optical Coherence Tomography

Optical coherence tomography (OCT) was developed in early 1990's for non-invasive cross-sectional imaging in biological systems. OCT uses low-coherence interferometry to produce a two-dimensional image of optical scattering from tissue in a way analogous to ultrasound imaging. In the most basic form, an OCT instrument consists of a Michelson-type interferometer with a focused sample arm beam and a lateral-scanning mechanism. OCT has longitudinal and lateral spatial resolution of a few micrometers and can detect reflected signals as small as 10^{-10} of the incident optical power.

OCT has found clinical applications mainly in the fields of ophthalmology. Recently, promising advances have also been made in the detection of cervical cancer with OCT. *In vivo* pilot studies have shown that in premenopausal women, average OCT reflection intensities from abnormal cervical epithelium were significantly stronger than normal epithelium, and vice versa in postmenopausal women.[23,24] These differences were attributed to neoplastic changes in the chromatin texture and the nuclear morphology and texture. The disadvantage of OCT is the fact that this technique does not provide biochemical information. Furthermore the information is not quantitative and needs subjective interpretation.

3.3 Confocal Microscopy

3.3.1 Principles of Confocal Microscopy

Confocal microscopy is an optical modality developed in the 1950's to overcome the poor contrast inherent in imaging thick specimens with a conventional microscope. The thick specimen can be sliced into very thin sections, which requires fixation, embedding, and staining, but this approach is obviously not suitable for imaging living cells or tissue. In contrast to conventional optical microscopy, confocal microscopy provides the elimination of out-of-focus light and the ability to collect serial optical sections from thick specimens. Spatial filtering is used to eliminate out-of-focus light in specimens that are thicker than the plane of focus. A point source is imaged by a lens to a diffraction-limited spot to illuminate three-dimensional specimen. The illuminated spot is mapped by another lens to a pinhole to reject off-focus light. The filtered light is then detected by a photodetector. Imaging of an optical two-dimensional optical section is achieved by laterally scanning a focused beam of light across the specimen. Confocal microscope can be implemented in both transmission and reflection modes. Also, both elastic scattering and fluorescence are used as a source of contrast in confocal microscopy.

Several studies explored the potential of reflectance and fluorescence confocal microscopy to image the morphologic and biochemical changes associated with precancer. Increased epithelial fluorescence, attributed to mitochondrial NADH, as well as decreased collagen fluorescence, attributed to collagen matrix degradation by matrix metalloproteinases, has been observed for dysplastic compared to normal cervical freshly excised tissue using fluorescence confocal microscopy.[25] Furthermore, *in vivo* reflectance confocal microscopy was successful in visualizing the increase in nuclear-to-cytoplasmic ratio and nuclear density associated with the progression of cervical intraepithelial neoplasia (CIN). These results demonstrate the potential of confocal reflectance to identify the morphological and biochemical changes associated with the progression of precancer. However, just as in the case of OCT, confocal microscopy does not provide quantitative information about tissue biochemistry and morphology and needs subjective interpretation.

3.4 References

1. A. Blaustein and R. J. Kurman, *Blaustein's pathology of the female genital tract*, Springer, New York (2002)
2. R. Kalluri and M. Zeisberg, "Fibroblasts in cancer," *Nature Reviews Cancer* **6** (5), 392-401 (2006).
3. H. Nagase and J. F. Woessner, "Matrix metalloproteinases," *Journal of Biological Chemistry* **274** (31), 21491-21494 (1999).
4. J. Mazibrada, M. Ritta, M. Mondini, M. De Andrea, B. Azzimonti, C. Borgogna, M. Ciotti, A. Orlando, N. Surico, L. Chiusa, S. Landolfo and M. Garigho, "Interaction between inflammation and angiogenesis during different stages of cervical carcinogenesis," *Gynecologic Oncology* **108** (1), 112-120 (2008).
5. J. R. Lakowicz, *Principles of Fluorescence Spectroscopy*, Kluwer Academics/Plenum Publishers, New York (1999)
6. R. D. Alvarez, T. C. Wright and O. D. Grp, "Effective cervical neoplasia detection with a novel optical detection system: A randomized trial," *Gynecologic Oncology* **104** (2), 281-289 (2007).
7. S. K. Chang, Y. N. Mirabal, E. N. Atkinson, D. Cox, A. Malpica, M. Follen and R. Richards-Kortum, "Combined reflectance and fluorescence spectroscopy for in vivo detection of cervical pre-cancer," *Journal of Biomedical Optics* **10** (2), - (2005).
8. I. Georgakoudi, E. E. Sheets, M. G. Muller, V. Backman, C. P. Crum, K. Badizadegan, R. R. Dasari and M. S. Feld, "Trimodal spectroscopy for the detection and characterization of cervical precancers in vivo," *American Journal of Obstetrics and Gynecology* **186** (3), 374-382 (2002).
9. W. K. Huh, R. M. Cestero, F. A. Garcia, M. A. Gold, R. S. Guido, K. McIntyre-Seltman, D. M. Harper, L. Burke, S. T. Sum, R. F. Flewelling and R. D. Alvarez, "Optical detection of high-grade cervical intraepithelial neoplasia in vivo: Results of a 604-patient study," *American Journal of Obstetrics and Gynecology* **190** (5), 1249-1257 (2004).
10. N. M. Marin, A. Milbourne, H. Rhodes, T. Ehlen, D. Miller, L. Benedet, R. Richards-Kortum and M. Follen, "Diffuse reflectance patterns in cervical spectroscopy," *Gynecologic Oncology* **99** (3), S116-S120 (2005).
11. Y. N. Mirabal, S. K. Chang, E. N. Atkinson, A. Malpica, M. Follen and R. Richards-Kortum, "Reflectance spectroscopy for in vivo detection of cervical precancer," *Journal of Biomedical Optics* **7** (4), 587-594 (2002).
12. J. R. Mourant, T. J. Bocklage, T. M. Powers, H. M. Greene, K. L. Bullock, L. R. Marr-Lyon, M. H. Dorin, A. G. Waxman, M. M. Zsemlye and H. O. Smith, "In vivo light scattering measurements for detection of precancerous conditions of the cervix," *Gynecologic Oncology* **105** (2), 439-445 (2007).
13. R. J. Nordstrom, L. Burke, J. M. Niloff and J. F. Myrtle, "Identification of cervical intraepithelial neoplasia (CIN) using UV-excited fluorescence and diffuse-reflectance tissue spectroscopy," *Lasers in Surgery and Medicine* **29** (2), 118-127 (2001).

14. I. M. Orfanoudaki, G. C. Themelis, S. K. Sifakis, D. H. Fragouli, J. G. Panayiotides, E. M. Vazgiouraki and E. E. Koumantakis, "A clinical study of optical biopsy of the uterine cervix using a multispectral imaging system," *Gynecologic Oncology* **96** (1), 119-131 (2005).
15. N. Ramanujam, M. F. Mitchell, A. Mahadevan, S. Thomsen, A. Malpica, T. Wright, N. Atkinson and R. RichardsKortum, "Development of a multivariate statistical algorithm to analyze human cervical tissue fluorescence spectra acquired in vivo," *Lasers in Surgery and Medicine* **19** (1), 46-62 (1996).
16. S. K. Chang, N. Marin, M. Follen and R. Richards-Kortum, "Model-based analysis of clinical fluorescence spectroscopy for in vivo detection of cervical intraepithelial dysplasia," *Journal of Biomedical Optics* **11** (2), - (2006).
17. D. Arifler, C. MacAulay, M. Follen and R. Richards-Kortum, "Spatially resolved reflectance spectroscopy for diagnosis of cervical precancer: Monte Carlo modeling and comparison to clinical measurements," *Journal of Biomedical Optics* **11** (6), - (2006).
18. A. Milbourne, S. Y. Park, J. L. Benedet, D. Miller, T. Ehlen, H. Rhodes, A. Malpica, J. Matisic, D. Van Niekirk, E. N. Atkinson, N. Hadad, N. Mackinnon, C. Macaulay, R. Richards-Kortum and M. Follen, "Results of a pilot study of multispectral digital colposcopy for the in vivo detection of cervical intraepithelial neoplasia," *Gynecol Oncol* **99** (3 Suppl 1), S67-75 (2005).
19. R. D. Alvarez and T. C. Wright, "Effective cervical neoplasia detection with a novel optical detection system: a randomized trial," *Gynecol Oncol* **104** (2), 281-289 (2007).
20. T. DeSantis, N. Chakhtoura, L. Twiggs, D. Ferris, M. Lashgari, L. Flowers, M. Faupel, S. Bambot, S. Raab and E. Wilkinson, "Spectroscopic imaging as a triage test for cervical disease: a prospective multicenter clinical trial," *J Low Genit Tract Dis* **11** (1), 18-24 (2007).
21. D. G. Ferris, R. A. Lawhead, E. D. Dickman, N. Holtzapple, J. A. Miller, S. Grogan, S. Bambot, A. Agrawal and M. L. Faupel, "Multimodal Hyperspectral Imaging for the Noninvasive Diagnosis of Cervical Neoplasia," *J Low Genit Tract Dis* **5** (2), 65-72 (2001).
22. S. Y. Park, M. Follen, A. Milbourne, H. Rhodes, A. Malpica, N. MacKinnon, C. MacAulay, M. K. Markey and R. Richards-Kortum, "Automated image analysis of digital colposcopy for the detection of cervical neoplasia," *J Biomed Opt* **13** (1), 014029 (2008).
23. P. F. Escobar, J. L. Belinson, A. White, N. M. Shakhova, F. I. Feldchtein, M. V. Kareta and N. D. Gladkova, "Diagnostic efficacy of optical coherence tomography in the management of preinvasive and invasive cancer of uterine cervix and vulva," *International Journal of Gynecological Cancer* **14** (3), 470-474 (2004).
24. A. F. Zuluaga, M. Follen, I. Boiko, A. Malpica and R. Richards-Kortum, "Optical coherence tomography: A pilot study of a new imaging technique for noninvasive examination of cervical tissue," *American Journal of Obstetrics and Gynecology* **193** (1), 83-88 (2005).

25. I. Pavlova, K. Sokolov, R. Drezek, A. Malpica, M. Follen and R. Richards-Kortum, "Microanatomical and biochemical origins of normal and precancerous cervical autofluorescence using laser-scanning fluorescence confocal microscopy," *Photochemistry and Photobiology* **77** (5), 550-555 (2003).

CHAPTER 4

Instrumentation

In this chapter we describe two instruments which were used to collect clinical data *in vivo*. First we introduce and explain in detail the hardware and the software of the contact-probe device, the Fast Excitation Emission Matrix (FastEEM) instrument. We further discuss the safety of using FastEEM instrument to conduct research involving human subjects. Finally, we introduce the Quantitative Spectroscopy Imaging (QSI) system, which is an extension of the point probe device with the wide-area surveillance capabilities.

4.1 Fast Excitation Emission Matrix Instrument

The first instrument that facilitated the clinical *in vivo* study of cervical dysplasia, developed by our lab, is called the Fast Excitation-Emission Matrix

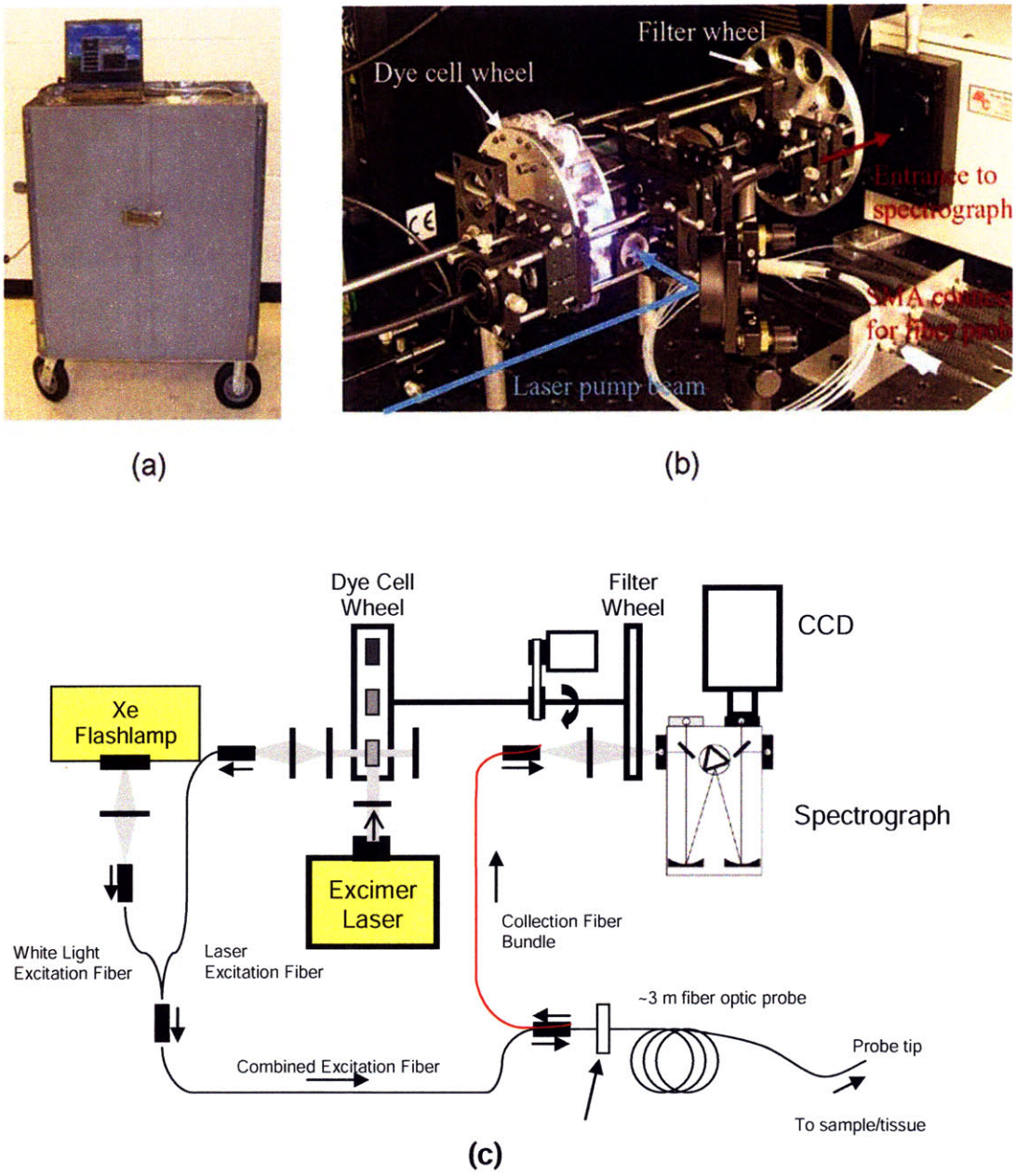

Figure 4.1.1. FastEEM instrument: (a) Full clinical instrument, (b) the dye cell and filter wheels that provide the sources for the laser induced fluorescence measurement, and (c) schematic representation of the optical components of FastEEM instrument.

Instrument (FastEEM).[1] It is a contact-probe portable device which acquires a set of white light diffuse reflectance spectra and nine fluorescence spectra in fraction of a second. The instrument is equipped with a XeCl excimer laser to excite tissue fluorescence and to pump a sequence of dye lasers which provide additional sources of fluorescence excitation. The pulsed white light source excites tissue reflectance. The measurements are obtained by bringing the flexible optical fiber probe into the gentle contact with tissue. The return fluorescence and reflectance collected by the probe are dispersed in a spectrograph and detected by an intensified CCD detector. A user-friendly interface has been developed through which the process of instrument calibration, data collection, and real time data analysis is integrated. Figure 4.1.1 shows photographs of full clinical instrument, the dye cell wheel that provides the sources for the laser induced fluorescence measurement, as well as the schematic representation of the optical components of the FastEEM instrument.

4.1.1 Excitation sources and delivery

The FastEEM is equipped with a XeCl excimer laser (Lambda Physik Optex, Ft. Lauderdale, FL, 308 nm, 8 mJ per pulse, FWHM 8 ns), which is a source for fluorescence excitation. The excimer laser is used as a source of fluorescence excitation, and as a pump for eight different dye lasers which provide additional 8 wavelengths for fluorescence excitation (from 340-460 nm). The laser dye solutions are contained within individual dye cells, which are 2.8 ml spectrosil quartz cuvettes (Starna Cells, Atascadero, CA) with a 10 mm pathlength and transmission from 170-2700 nm. Dye solutions are a mixture of the laser dyes shown in Table 4.1.1. and a solvent (either p-dioxane or methanol).

Table 4.1.1. Technical specifications for FastEEM laser dyes.

Laser Dye	Solvent	Emission λ [nm]	FWHM [nm]
p-Terphenyl (PTP)	*p*-dioxane	342	9
PBD	*p*-dioxane	360	8
Exalite 384	*p*-dioxane	383	7
Exalite 398	*p*-dioxane	400	7
LD 425	*p*-dioxane	407	8
Stilbene 420	methanol	425	12
Coumarin 440	methanol	441	8
Coumarin 460	methanol	461	8

The dye cells, as well as the optical arrangement for redirecting the excimer laser beam to the common collection fiber (right-angle prism and cylindrical lens), are mounted on a rotating wheel driven by an AC motor at ~ 3 Hz. As the wheel spins, the dye cells are pumped by the XeCl excimer laser. Synchronization is achieved by means of trigger pins positioned on the wheel, corresponding to each of the dye cells, and the laser. The output pulses are directed through a 10% reflective mirror and lens into the laser excitation fiber of the optical fiber probe.

The Xe arc flashlamp (Hamamatsu L7684, Bridgewater, NJ, 1 J per pulse, FWHM 2 μs), is a source for the white light reflectance excitation. The two open spaces in the wheel are reserved for white light excitation. When these positions traverse the optical cavity, the Xe flashlamp is triggered and focused by a lens into a white light excitation fiber. Two optical components are positioned between the lamp and the focusing lens: a long-pass (LP) filter to block any wavelength of light shorter than 300 nm to be delivered to tissue, as well as a neutral density filter with lower transmission characteristics in the blue then the rest of the spectral range. The latter is used to achieve an optimal white light excitation profile since the lamp easily saturates in the blue compared to the rest of the spectral range. The white light, as well as the different fluorescence excitation wavelengths are coupled by a Y-coupler to the single excitation fiber of an optical probe and delivered to the tissue.

4.1.2 Optical fiber probe

The optical probe, approximately 1.2 mm in diameter and 3 m in length, has a six-around-one geometry, with a central light delivery fiber and 6 surrounding collection fibers. All fibers are identical 200 μm core diameter multimode fibers with 0.22 numerical aperture which are fused together to form a quartz shield approximately 1 mm long. The quartz shield provides a well-defined delivery/collection geometry creating a sampling spot on the tissue surface with a diameter of approximately 800 μm. The 17° beveled tip prevents specular reflection from the probe-air interface. The measurements are made by bringing the probe into contact with the tissue. Figure 4.1.2 shows a photograph and a schematic diagram of the distal tip of the optical fiber probe.

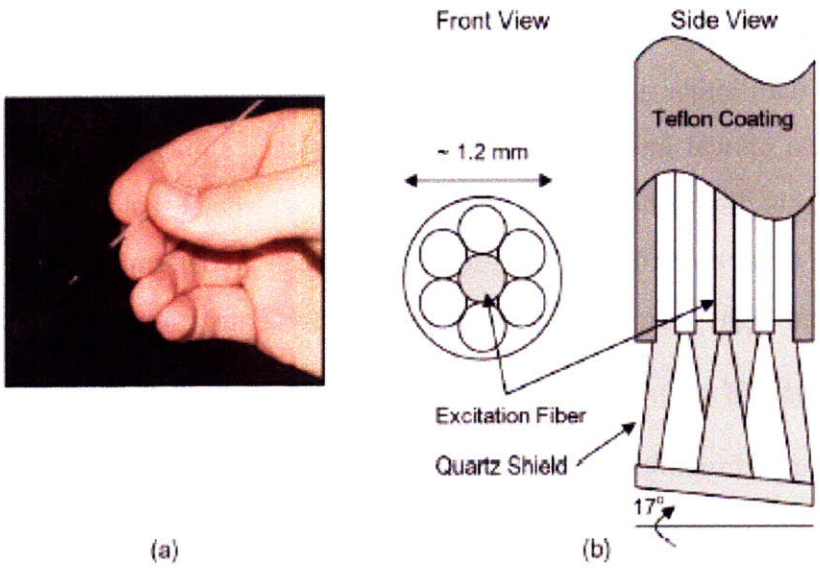

Figure 4.1.2. (a) Photograph and (b) schematic diagram of the distal tip of the optical fiber probe.

4.1.3 Collection and Detection system

The six collection fibers are terminated by SMA connectors, which allows for quick changing of the optical fiber probes. The six collection fibers are focused on the entrance slit of the diffraction grating spectrograph (Spectra Pro 150, Acton Research, Acton, MA, 300 grooves/mm with 500 nm blaze, center wavelength 550 nm), where they are arranged linearly and parallel to the slit. The backscattered fluorescence excitation light is prevented from entering the spectrograph by the means of the "filter wheel". The filter wheel spins in synchronization with the dye cell wheel. It holds the long pass filters that remove the excitation line from the collected light.

The return fluorescence and reflectance collected by the probe are dispersed in the spectrometer, and detected by an intensified gated CCD detector (PIMAX, Roper Scientific, Princeton, NJ). The dimensions of the chip are 256x1024 pixels. The rapid gated detection of the intensified CCD minimizes motion artifacts and enables data to be acquired in the presence of ambient light. The CCD is cooled to -20 ° C to reduce noise from the dark current and improve the signal-to-noise ratio.

The timing of the data collection is achieved through the use of a National Instruments timer/counter board (PCI-6602, National Instruments, Austin, TX).

Optical interrupters (Omron Photomicrosensors EE-SX770, Schaumburg, IL) are used to generate trigger signals from pins mounted on the rotating wheel. When a pin, associated with either a dye cell or a flesh lamp, passes through the beam of light between two optical interrupters, the constant voltage signal generated between the two sensors is diminished. This generates a trigger signal that is read by the timer board. The timer controller uses these trigger signals to determine when to pulse the laser or white light source and when to gate and read data from the detector.

4.1.4 FastEEM software

A user-friendly interface was developed by a team of engineers through which the entire process of instrument calibration, data collection, and real time

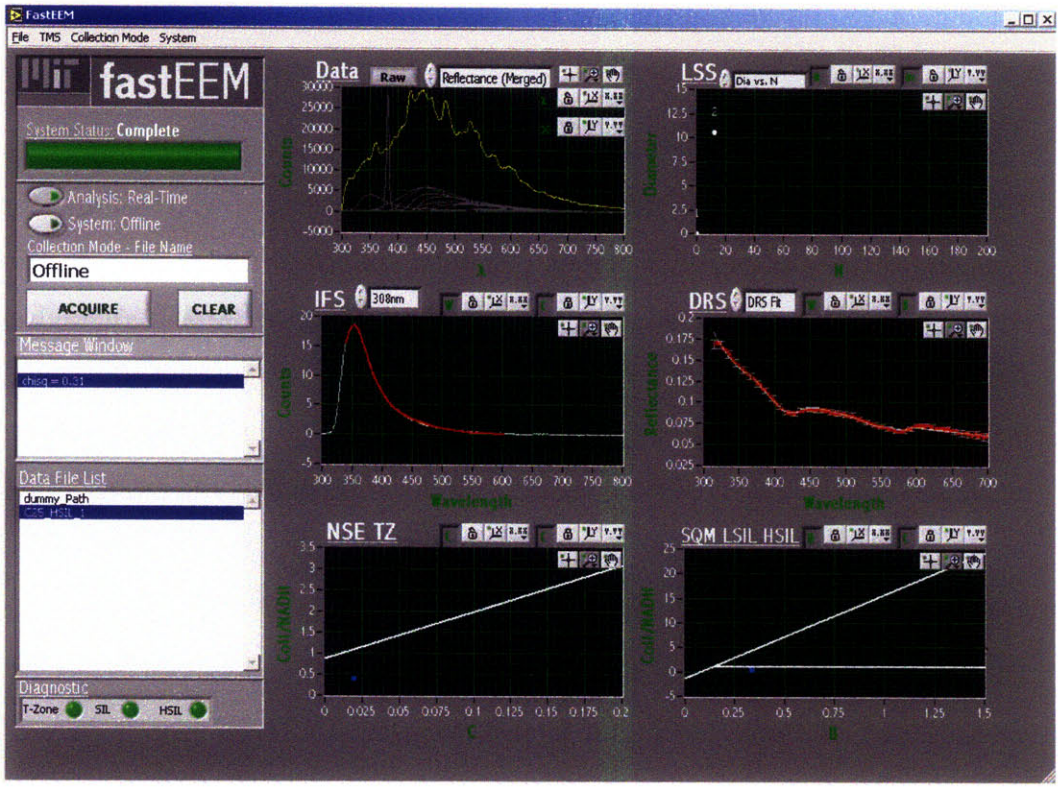

Figure 4.1.3. An interface provides visual and quantitative feedback during data collection.

diagnosis is integrated (Figure 4.1.3). A custom-designed software program was created using LabView 7.0 (National Instruments Corporation, Austin, TX). Data acquisition is initialized either by pressing a push-key within the program or by using

a footswitch, which provides control to the physician acquiring the data. Using the interface, various settings can be controlled including the gain on the CCD and the number of spectra to be averaged for each measurement. As a result of this thesis work, real-time analysis of the collected diffuse reflectance and fluorescence data using the mathematical models described in Chapter 5 can also be performed by the software in combination with MATLAB (The MathWorks, Inc. Natick, MA).

4.1.5 Instrument Calibration

Background calibration is used to remove effects of CCD dark currents and stray light. All data were corrected for background reflectance and fluorescence by measuring a spectrum from water in a black container and subtracting these counts from the signal measured from the sample. The wavelength calibration is performed by recording a spectrum from a mercury argon lamp (HG-1, Ocean Optics, Dunedin, FL) each day of data collection. Because the wavelengths of the mercury peaks are known, we determine the relationship between pixel number and wavelength by fitting a second-order polynomial to a plot of the wavelength of each peak versus the pixel number of the peak. White light reflectance calibration is achieved by dividing the background corrected tissue spectrum by that of a reflectance standard (20 % reflectance standard, Labsphere Inc., North Sutton, NH). Calibration of the measured reflectance corrects for the spectral profile of the flashlamp and the wavelength-dependence of the detector response. Each EEM is corrected for excitation intensity of the dye lasers by measurement of a standard rhodamine B dye mixture (5 g/L in ethylene-glycol). The known quantum yields of rhodamine B are then used to correct the intensity of each emission spectrum.

4.1.6 FastEEM safety

The FastEEM instrument delivers very low fluence of light to the tissue. The specifications for the light delivered to the tissue are presented in Table 4.1.2. (i.e. the light output of the optical fiber probe). The total light exposure to the tissue is less than what would be expected from 10 seconds of sun exposure on a sunny day in Southern California (determined from reference 2)[2].

Table 4.1.2. Specifications of the light delivered to the tissue

Specifications	Flash Lamp	Laser
Repetition Rate (Hz^1)	6	30
Radiant Energy (μJ/pulse)	1	1 - 4
Pulse Width, FWHM (ns)	$6*10^3$	9
Fluence per Pulse (mJ/cm^2)	0.17	0.17-0.68

The earliest model of the FastEEM instrument was developed on our laboratory in 1996.[3] Since that time, data has been collected in the clinic from over 350 patients from various tissue sites including the esophagus[4], the cervix[5], and the oral cavity[6]. To date, there have been no cases of patients experiencing adverse effects as a result of participation in this study. The protocol for our *in* vivo work has been reviewed and approved by Institutional Review Boards (IRB) at the respective institutions, including the Medical University of South Carolina (MUSC), the Brigham and Women's Hospital, the Veteran's Administration (VA) Hospital, Jamaica Plain, and Boston Medical Center.

Instruments similar to the FastEEM, with the radiant exposure similar to ours (337 nm N_2 laser, spot size 0.785 mm^2, 10 pulses per site, 8.71 μJ/pulse, 30 Hz repetition rate, FWHM of 5 ns) were used at the University of Texas at Austin and at the UT M.D. Anderson Cancer Center in Houston for detection of cervical cancer in a National Cancer Institute (NCI) sponsored project. The UT Austin investigators have found that the relative risk of ultraviolet exposure from their spectroscopic system and colposcopy is comparable.[7] The total light exposure in our study is an order of magnitude less than that presented in the MDACC study. The study had involved a large number of patients and no adverse effects have been reported.

4.1.7. Instrumentation Improvements

A number of instrumentation advancements have been made as a result of this thesis work. Here we explain hardware modification to ensure reliable reflectance and fluorescence data collection, as well as software fix developed to remove spectral artifacts in tissue data retrospectively.

4.1.7.i. Reliable reflectance spectra collection: Second order light fix

At the beginning of the thesis work, we identified an artifact in the diffuse reflectance tissue data collected over the period of two years. Our diffusion model (see Chapter 5 for details) was consistently unable to fit the red portion of the diffuse reflectance spectra. The initial hypothesis was that tissue spectra could not be approximated well as one-layer homogeneous semi-infinite media, due to the stratified structure of the epithelium. However, when tissue model experiments were performed the same problem arose. The tissue model is composed of spherical polystyrene beads of uniform size as a source of scattering and hemoglobin as a source of absorption, thus representing an experimental model that is well described by the theory and assumptions that we use in data analysis. Scattering and absorption coefficients of tissue models were chosen to cover the physiological range found in the epithelial tissue.

The second hypothesis for the cause of the artifact was that a significant amount of second order light is generated by the reflection grating in the spectrograph, thus distorting reflectance measurement. Second-order light corresponds to a higher order diffraction pattern of the signal from the shorter wavelengths, produced at exactly twice the original wavelength. Because of the spatial overlap of this signal with the true reflectance measured at the longer wavelengths, the counts recorded by the CCD would represent a combination of the two signals. We tested the hypothesis by inserting a 400 nm long pass filter (LP400) in front of the flashlamp, thereby cutting off shorter wavelengths. This significantly reduced the intensity of the red portion of the spectrum (>600 nm) in the phantoms. We concluded that the second order light generation indeed was a cause of the artifact in reflectance spectra.

This problem was resolved in two ways. As the FastEEM wheel rotates, two diffuse reflectance spectra, with and without LP 400, are now acquired. The reflectance spectra from 450-800 nm taken with LP 400 (corrected for the transmission properties of the filter) are merged with the reflectance spectra from 300-450 nm taken without the filter to provide a composite diffuse reflectance

spectrum covering the full spectral range (300-800 nm), free of the second order effect. Figure 4.1.4. shows diffuse reflectance spectra taken without and with the hardware fix, along with a spectrum predicted with diffusion theory, which overlaps with the hardware-corrected data.

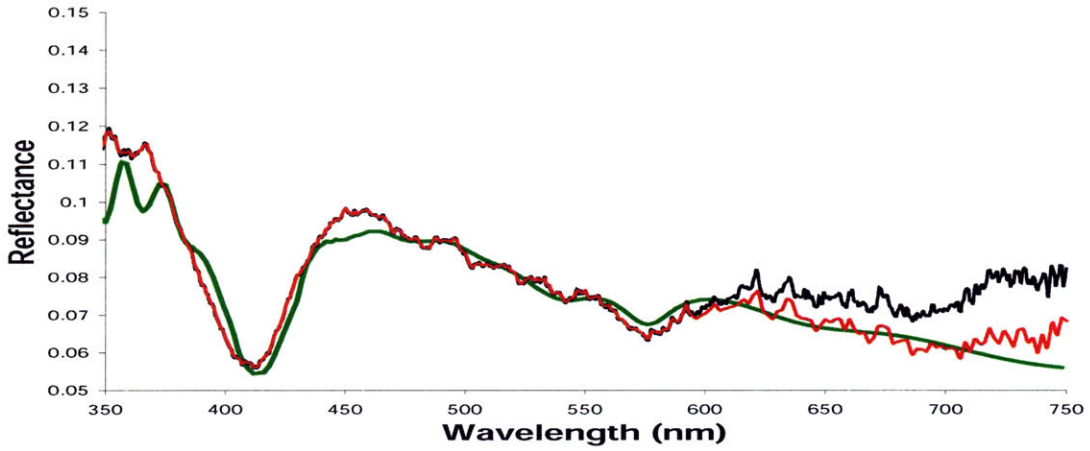

Figure 4.1.4. Diffuse reflectance spectra of a tissue model with hemoglobin concentration of 1 mg/ml and reduced scattering coefficient of 2 mm^{-1} Black: uncorrected spectrum; Red: spectrum taken with corrected instrument; Green: prediction of diffusion theory.

In addition to correcting the instrument, we developed an algorithm that removes the distortion from past corrupted spectra ("software fix"). We conducted a set of experiments by which we were able to quantify the portion of the first order light that shows up as the second order as a function of wavelength for our grating (e.g. percentage of light at 300 nm that shows up at 600 nm). We achieved this by collecting the emission spectra of various dyes in both first and second order, thus covering a wide spectral range. We validated our correction algorithm by performing tissue model experiments. As shown in Figure 4.1.5., tissue model data taken with the corrected instrument and data for software-corrected reflectance overlap. As a result of the software-fix, we were able to correct and salvage two years worth of clinical in vivo data collected from Barrett's esophagus.

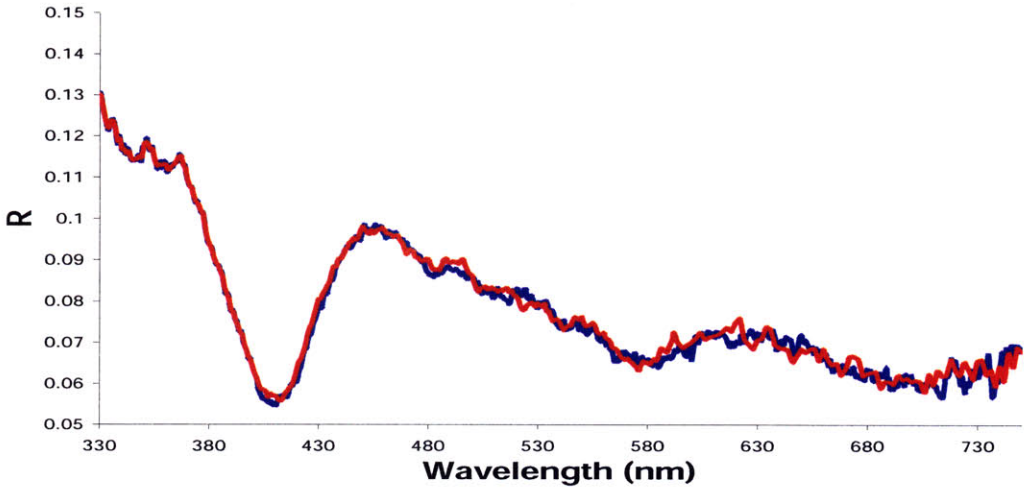

Figure 4.1.5. Spectral data obtained using the corrected instrument ("hardware fix") (red), and the software corrected data (blue).

4.1.7.ii. Reliable spectra collection: Colposcopy background light removal

After resolving the second order artifact, we identified a second artifact that was corrupting tissue spectra collected *in vivo*. We observed an occasional signal in the fluorescence spectra which couldn't be accounted for by emission of fluorophores included in our fluorescence model (see Chapter 5 for details). This signal was observed in variety of tissue data (bladder, esophagus, cervix, and oral cavity) collected by FastEEM instruments located in different medical institutions. The initial hypothesis was that tissue contained an unknown fluorophore that we haven't accounted for. However, we observed that the tissue fluorescence emission spectra contained the characteristic light pattern with lineshape and intensity which did not change for the entire range of FastEEM excitation wavelengths (308-480 nm). Fluorophores are typically not excited by such a wide wavelength range. Furthermore, quantum yield of the fluorophore changes with the excitation wavelength, and it would be expected that the intensity of the emitted light should vary from excitation to excitation. We concluded that this signal could not be explained by an emission of unknown fluorophore.

The next hypothesis for the source of unknown fluorescence signal was that the overhead lights in the operating room which were shone directly on the tissue during data collection, or colposcope light, were diffusing into the tissue and being collected by our probe. Unlike ambient room light which is weak and not focused directly on the tissue, these light sources are more powerful and directed on the tissue in a more focused manner. We showed that this hypothesis was correct by testing the spectrum of tissue phantom that exhibits no fluorescence. When data was collected in the absence of colposcopy light, no counts in fluorescence channels were observed. In the case when the colposcopy light was turned on, and positioned ~20 cm away (as during colposcopy) from the same tissue phantom, the artifact was observed (see Figure 4.1.6. (a)). This pattern was observed even in the absence of reflectance excitations. We next demonstrated that the artifact is truly coming from the colposcopy light which diffused into the tissue, emerged at the surface of the tissue, and got collected by the probe, and not the background light. When the probe was not in contact with tissue but exposed to ambient light, no artifact was seen (Figure 4.1.6. (b)).

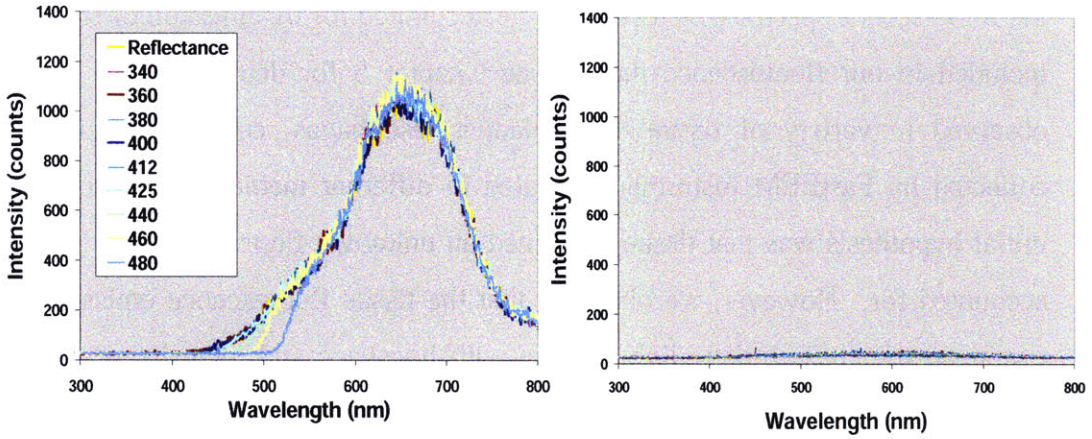

Figure 4.1.6. Stray light pattern (a) Measured signal showing in the reflectance and fluorescence channels caused by colposcope light focused on tissue (no reflectance or fluorescence excitation sources on), (b) Measured signal showing in the reflectance and fluorescence channels (no reflectance or fluorescence excitation sources on), when colposcope light was focused, and probe was not in contact with tissue.

We developed a strategy to correct both the reflectance and fluorescence signal for this artifact. First we identified a fluorescence excitation at which the measured fluorescence excitation signal was negligible (440 nm excitation). The signal measured for this excitation was not due to fluorescence, but to the stray light signal. We corrected the stray light spectrum for the transmission properties of the long-pass filter used for 440 nm excitation light, to recover the true spectrum of the stray light. The reflectance spectra were corrected by subtracting these counts from the measured spectrum. Figure 4.1.7. shows an example of reflectance spectra with stray light present, stray light corrected, and calibrated reflectance with colposcopy light turned off. As shown in Figure 4.1.7. stray light corrected spectrum overlaps with a reflectance spectrum collected with the light turned off. The measured signals at the remaining fluorescence excitations were then corrected by subtracting this spectrum from the measured signal at the excitation after multiplying the stray light spectrum by the transmission properties of the filter used at the particular excitation. We used this strategy to correct all the tissue in Barrett's esophagus, oral cavity, and the cervix. Once this problem was recognized, extra light sources other than room lights were turned off prior to each measurement.

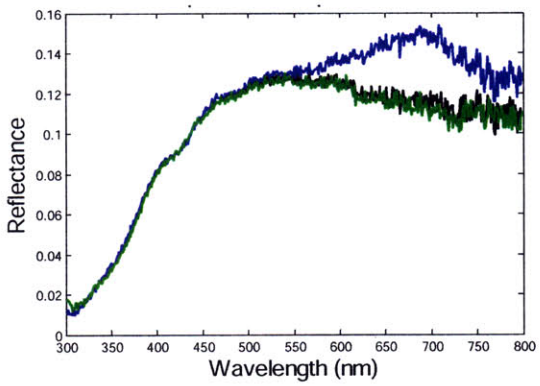

Figure 4.1.7. Reflectance spectra with stray light present (blue line), stray light correction (black line), and calibrated reflectance (green line) with colposcopy light turned off.

4.2 Quantitative Spectroscopy Imaging Instrument

The contact-probe instrument, FastEEM, and the analysis models developed in our laboratory (see Chapter 5) provide the detailed quantitative biochemical and morphological information, but only from several 1 mm^2 areas, thus lacking adequate tissue sampling. In order to screen the entire area at risk of developing cervical cancer, we developed a Quantitative Spectroscopy Imaging (QSI) Instrument. The QSI instrument is an extension of the contact-probe device with wide-area surveillance capabilities.[8]

We employed the principle of the "virtual probe" to provide wide area coverage while retaining the ability to extract detailed quantitative information about tissue biochemistry and morphology. The tip of the optical fiber is imaged to the tissue spot with similar geometry to the contact-probe, and then raster scanned across the entire organ to provide wide-area surveillance. The virtual probe provides several advantages over full-field illumination. Since the delivery-collection geometry is small, we are able to extract optical properties, such as reduced scattering coefficient and absorption coefficient independently. Furthermore, we are able to directly apply the knowledge acquired in the contact-probe studies over the period of couple of years to imaging studies.

QSI illuminates a 1 mm^2 region of the cervix with visible and 337 nm light and measures reflectance and fluorescence spectra over the visible wavelengths. Once the measurement is complete for one region, another 1 mm^2 region is interrogated until a 2.1 cm x 2.1 cm area of the cervix with 441 interrogation points (pixels) is examined. The total acquisition time is approximately 90 seconds. Motion compensation is achieved by acquiring regular white light photographs of the cervix once every second.

4.2.1. Instrumentation design

The QSI instrument is a portable clinical device with a modular design. As shown in the schematic representation of the QSI instrument (Figure 4.2.1), all the heavy components are positioned on the mobile cart, while a lightweight mobile

optical head is independent and easily operated by the physician. The three heavy instrument modules, mounted on the cart, are connected to the optical head by means of the optical fibers. Module 1 contains a xenon arc lamp (Simplicity series, Newport Corporation, 390-700 nm, 75 W, continuous wave) which is a source for the white light reflectance excitation, and the N_2 laser (NL100, Standford Research Systems Inc., 337 nm, 175 μJ per pulse, FWHM 3.5 ns), which is the source of fluorescence excitation. Module 2 contains a spectrograph and a CCD unit (Princeton Instruments Corp.). Module 3 contains the computer, which controls data acquisition and analysis. National Instruments Labview software and data acquisition hardware are used to control and coordinate the various pieces of equipment. Module 4, an optical head, is mounted on an articulated arm for easy maneuvering. This module is positioned on a smaller mobile cart which is independent from the other three modules, so that the optical head can be positioned next to the patient.

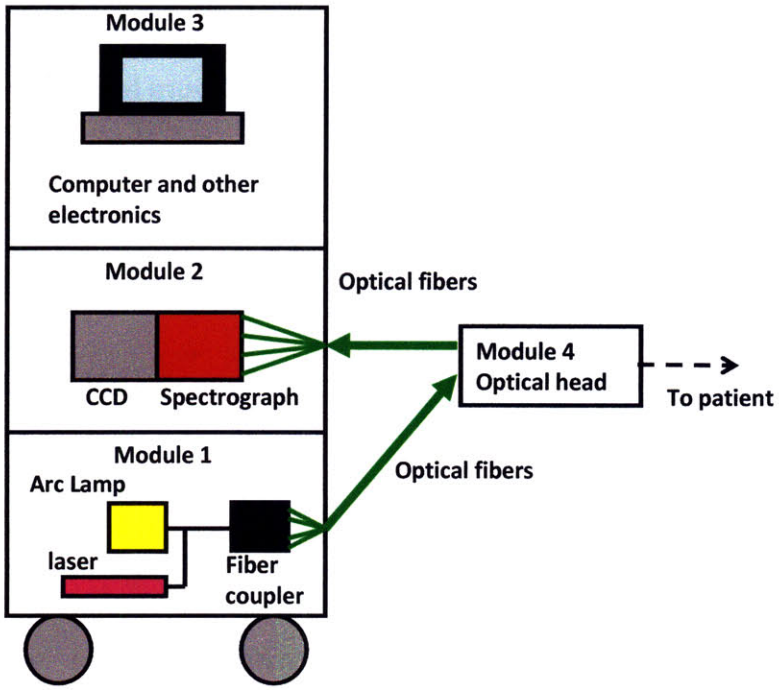

Figure 4.2.1: (a) Schematic representation of the QSI instrument.

Figure 4.2.2. is a schematic diagram of the optical head. The delivery/collection geometry is identical for both white light reflectance and fluorescence measurements. The incident light (NA ~ 0.02) illuminates a 1mm diameter spot on the tissue approximately 20 cm away from the optical head. The light emerging from tissue is collected from a concentric 2 mm diameter spot. This light is relayed back to the optical head and focused onto eight collection fibers which are coupled to a spectrograph and a CCD.

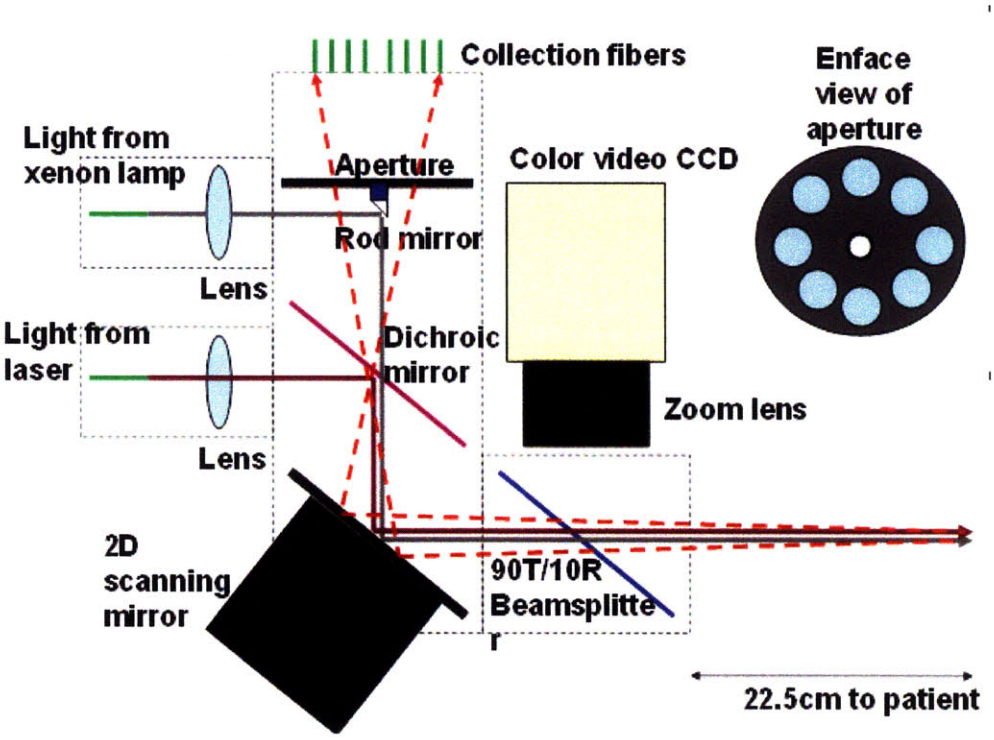

Figure 4.2.2.: Schematic diagram of the optical head.

Imaging is achieved by means of a two-dimensional scanning mirror (OIM102, Optics in Motion LLC), which raster scans the diagnostic spot across a 2.1 cm x 2.1 cm region of the tissue surface in a stepwise fashion. At each position, a reflectance measurement is conducted followed by a fluorescence measurement. An onboard color video camera (QICAM, QImaging Corp.) monitors both the movement of the light spot over the tissue and patient motion relative to that of the instrument.

The images collected by the video camera allow for measurement motion compensation, such that spectroscopy measurements can be correlated with the correct area of tissue examined. Two white light LEDs, provide extra illumination for the video camera. The total time required for a 2.1 cm x 2.1 cm scan is ~ 90 s.

4.3 References

1. J. W. Tunnell, A. E. Desjardins, L. Galindo, I. Georgakoudi, S. A. McGee, J. Mirkovic, M. G. Mueller, J. Nazemi, F. T. Nguyen, A. Wax, Q. G. Zhang, R. R. Dasari and M. S. Feld, "Instrumentation for multi-modal spectroscopic diagnosis of epithelial dysplasia," *Technology in Cancer Research & Treatment* **2** (6), 505-514 (2003).
2. NSF Polar Programs UV Monitoring Network, *Updates on UV Irradiance Levels.*
3. R. A. Zangaro, L. Silveira, R. Manoharan, G. Zonios, I. Itzkan, R. R. Dasari, J. VanDam and M. S. Feld, "Rapid multiexcitation fluorescence spectroscopy system for in vivo tissue diagnosis," *Applied Optics* **35** (25), 5211-5219 (1996).
4. I. Georgakoudi, B. C. Jacobson, J. Van Dam, V. Backman, M. B. Wallace, M. G. Muller, Q. Zhang, K. Badizadegan, D. Sun, G. A. Thomas, L. T. Perelman and M. S. Feld, "Fluorescence, reflectance, and light-scattering spectroscopy for evaluating dysplasia in patients with Barrett's esophagus," *Gastroenterology* **120** (7), 1620-1629 (2001).
5. I. Georgakoudi, E. E. Sheets, M. G. Muller, V. Backman, C. P. Crum, K. Badizadegan, R. R. Dasari and M. S. Feld, "Trimodal spectroscopy for the detection and characterization of cervical precancers in vivo," *American Journal of Obstetrics and Gynecology* **186** (3), 374-382 (2002).
6. M. G. Muller, T. A. Valdez, I. Georgakoudi, V. Backman, C. Fuentes, S. Kabani, N. Laver, Z. M. Wang, C. W. Boone, R. R. Dasari, S. M. Shapshay and M. S. Feld, "Spectroscopic detection and evaluation of morphologic and biochemical changes in early human oral carcinoma," *Cancer* **97** (7), 1681-1692 (2003).
7. C. K. Brookner, A. Agrawal, E. V. Trujillo, M. F. Mitchell and R. R. RichardsKortum, "Safety analysis: Relative risks of ultraviolet exposure from fluorescence spectroscopy and colposcopy are comparable," *Photochemistry and Photobiology* **65** (6), 1020-1025 (1997).
8. C. C. Yu, C. Lau, G. O'Donoghue, J. Mirkovic, S. McGee, L. Galindo, A. Elackattu, E. Stier, G. Grillone, K. Badizadegan, R. R. Dasari and M. S. Feld, "Quantitative spectroscopic imaging for non-invasive early cancer detection," *Optics Express* **16** (20), 16227-16239 (2008).

CHAPTER 5

Methods

In this chapter we introduce Tri-Modal Spectroscopy (TMS), a technique used to provide spectral diagnosis developed in our laboratory. We then describe the statistical methods used in this thesis to determine the statistical significance of extracted parameters and to develop the algorithms for disease diagnosis. Finally, we explain the clinical *in vivo* study design for both contact-probe and imaging studies.

5.1 Data Modeling

The sources of spectroscopic contrast in tissue reflectance and fluorescence due to the presence of disease are related to the changes that accompany cervical dysplasia, including loss of differentiation of the epithelial cells[1], degradation and reorganization of stromal collagen by matrix metalloproteinase activity[2,3], and angiogenesis[4]. The MIT Spectroscopy Laboratory have developed Tri-Modal Spectroscopy (TMS), a technique which uses physically based models to analyze cervical tissue spectra and provide spectral diagnosis. The advantage of TMS, being a model-based spectroscopy technique, is that it provides an understanding of the origins of spectroscopic contrast between normal and diseased tissue, and they diagnose disease based on quantitative information about tissue morphology and biochemistry.

TMS is a combination of three spectroscopic techniques: Diffuse Reflectance Spectroscopy (DRS), Intrinsic Fluorescence Spectroscopy (IFS), and Light Scattering Spectroscopy (LSS). The work presented in this thesis focuses primarily on DRS and IFS analysis. Here we explain the details of DRS and IFS, as well as why LSS is no longer used in our data analysis.

5.1.1 Diffuse Reflectance Spectroscopy (DRS)

Multiple scattering, a dominant light-tissue interaction responsible for the turbid appearance of biological tissue, is said to be diffusely reflected. DRS uses the information contained in multiply scattered light reemitted from tissue to extract the morphological properties of the tissue, as well as its absorption. Tissue reflectance spectra are analyzed using the model based on the diffusion approximation to the radiative transport equation developed in our laboratory by Zonios et al.[5] The penetration depth of the diffusive light is 0.5-1.5mm, depending on the wavelength and the type of tissue probed, which is mostly connective tissue. Therefore DRS provides information mainly about the morphology and absorption of the stroma.

The radiative transport equation represents a simpler approach than Maxwell's equations to describe the light propagation in media. The wave nature of light is

ignored, and transport of power through turbid medium is directly considered. The radiative transport equation can only be solved numerically, and requires further simplifications, such as diffusion approximation, in order to provide a closed form solution. In diffusion approximation to the radiative transport picture, photons engage in a random walk within the medium. Diffusion theory is appropriate in a medium dominated by scattering rather than absorption, which is often the case in tissue, so that each photon undergoes many scattering events before being terminated by an absorption event. The absorption and scattering properties of media are typically described by two wavelength dependent parameters, the absorption coefficient (μ_a) and scattering coefficient (μ_s). The inverse of these values represents the average distance traveled by a photon before encountering an absorber or scatterer, respectively. Diffusion theory also requires isotropic scattering in the medium (an equal probability of scattering in all directions), which is not the case in tissue. The scattering in tissue is, rather, strongly forward-directed. Anisotropy factor (g) is a measure of the amount of forward direction retained after a single scattering event and is equal to the average cosine of the scattering angle. To satisfy the diffusion approximation requirement of isotropic scattering in medium, another parameter, the reduced scattering coefficient (μ_s') is used instead of μ_s. μ_s' describes the diffusion of photons in a random walk of step size of $1/\mu_s'$, in units of length, where each step involves isotropic scattering. μ_s' is given by the following expression:

$$\mu_s'(\lambda) = \mu_s(\lambda) \cdot (1 - g)\ [\mathrm{mm}^{-1}], \tag{5.1}$$

In this case, the random walk is equivalent to describing photon movement using many small steps, $1/\mu_s$, that each involves a deflection angle.

The amount of light collected by the probe modeled by Zonios et al. is expressed in terms of the optical properties of tissue (μ_s' and μ_a) and the geometry of the probe. The basis of the Zonios model is an expression derived by Farrell et al.[6] who calculated the diffuse reflectance from a narrow beam of light incident on the surface of a semi-infinite turbid medium in the diffusion approximation. Here the

diffuse reflectance radial density is expressed as a function of distance from the point of incidence.

$$R(\lambda, r) = \frac{z_0}{4\pi}\frac{\mu_s' + \mu_a}{\mu_s'} \cdot \left[\left(\mu + \frac{1}{r_1} \right) \cdot \frac{\exp(-\mu r_1)}{r_1^2} + \left(1 + \frac{4}{3} \right) A \left(\mu + \frac{1}{r_2} \right) \frac{\exp(-\mu r_2)}{r_2^2} \right] \tag{5.2}$$

where

$$r_1' = (z_o^2 + r^2)^{1/2} \ , \quad r_2' = \left[z_o^2 \left(1 + \frac{4}{3} A \right) + r^2 \right]^{1/2} ,$$

$$z_o = \frac{1}{\mu_s' + \mu_a} \ , \quad \mu = \sqrt{3 \cdot \mu_a \cdot (\mu_s' + \mu_a)} \ , \tag{5.3}$$

$$A = \frac{1+y}{1-y} \quad \text{and} \quad y = -1.44 n_{rel}^{-2} + 0.710 n_{rel}^{-1} + 0.0636 n_{rel} + 0.668.$$

To account for the mismatch in refractive index at the tissue-surface interface, the parameter A describes the internal reflection at the interface and is calculated using the term y as described above. The term n_{rel} is the relative refractive index.

To find the total light collected by the probe, Farrell's expression was first integrated over the spatial extent of the light delivery and collection areas. Finally, in order to obtain a simple analytical expression, point delivery of light and collection over a circular spot with and effective radius r_c' was assumed, obtaining the following expression.

$$R(\lambda) = \frac{\mu_s' + \mu_a}{\mu_s'} \cdot \left\{ \exp(-\mu z_o) + \exp\left[-\left(1 + \frac{4}{3} A \right) \mu z_o \right] - z_o \frac{\exp(-\mu r_1')}{r_1'} - \left(1 + \frac{4}{3} A \right) z_o \frac{\exp(-\mu r_2')}{r_2'} \right\} \tag{5.4}$$

with

$$r_1' = (z_o^2 + r_c'^2)^{1/2} \ , \quad r_2' = \left[z_o^2 \left(1 + \frac{4}{3} A \right) + r_c'^2 \right]^{1/2} , \tag{5.5}$$

The r_c' depends on the probe geometry and can be determined by using a calibration phantom with known scattering and absorption properties. The r_c' of the probes used in studies presented in this thesis was determined to be 0.35 cm.

Equation 5.1 is used to analyze diffuse reflectance spectra collected by the probe.

5.1.1.i Modeling of the reduced scattering coefficient

An analytical expression was used to describe μ_s':

$$\mu_s'(\lambda) = A\left(\frac{\lambda}{\lambda_0}\right)^{-B} + C\left(\frac{\lambda}{\lambda_0}\right)^{-4} \quad [\text{mm}^{-1}], \tag{5.6}$$

where the wavelength, λ, is expressed in units of microns and λ_0 is equal to 0.7 μm. The A parameter is related to scatterer density, and the B parameter is related to the size of the Mie scatterers. The first term on the right-hand side of this expression has been commonly used by other researchers to model scattering from cells and tissues. We found that the second term was required to accurately model reflectance at shorter wavelengths (<400 nm), in which scattering from Rayleigh particles is significant.

5.1.1.i Modeling of the absorption coefficient

The absorption coefficient was modeled as the sum of the hemoglobin and β-carotene absorption coefficients as follows:

$$\mu_a(\lambda) = \mu_a^{Hb}(\lambda) + \mu_a^{\beta-car}(\lambda) \quad [\text{mm}^{-1}]. \tag{5.7}$$

The absorption coefficient of hemoglobin was modified by a correction factor to account for the fact that hemoglobin is confined to blood vessels, rather than homogeneously distributed in the tissue.[7] This effect, called vessel packaging, is caused by the fact that blood vessels are opaque to 420 nm light which is strongly absorbed by hemoglobin, but become more transparent to longer wavelengths of light. As a result, the Soret band (420 nm) is reduced relative to that of the weaker hemoglobin absorption bands. We used the correction factor $C_{diff}(\lambda, bvr)$ developed by van Veen et al.[8] and Svaasand et al.[9] to account for the effects of vessel packaging:

$$C_{diff}(\lambda) = \left\{\frac{1-\exp\left[-2\cdot\mu_a^{blood}(\lambda)\cdot bvr\right]}{2\cdot\mu_a^{blood}(\lambda)\cdot bvr}\right\}, \tag{5.8}$$

where *bvr is* the effective blood vessel radius in units of mm, and $\mu_a^{blood}(\lambda)$ is absorption coefficient of whole blood in units of mm^{-1}, given by:

$$\mu_a^{blood}(\lambda) = \log 10 \cdot 150\, mg/mL \cdot [(1-\alpha)\varepsilon_{Hb}(\lambda) + \alpha\varepsilon_{HbO_2}(\lambda)], \quad (5.9)$$

where α is the oxygen saturation of hemoglobin, and ε_{HbO2} and ε_{Hb} are the well known extinction coefficients of oxygenated and deoxygenated hemoglobin.[10] We assume that hemoglobin concentration of whole blood is 150 mg/mL[8], and impose a lower limit of 2.5 μm for *bvr* since the minimum diameter of a capillary is on the order of 5-7 μm.[11] The absorption coefficient of hemoglobin, μ_a^{Hb}, is then given by the expression:

$$\mu_a^{Hb}(\lambda) = C_{diff}(\lambda) \cdot \nu \cdot \mu_a^{blood}(\lambda) \quad [mm^{-1}], \quad (5.10)$$

where ν is the volume fraction of blood sampled and is described by the ratio:

$$\nu = {}^{[Hb]}/_{150}, \quad (5.11)$$

with [Hb] the total concentration of hemoglobin in units of mg/mL. The absorption coefficient of hemoglobin, $\mu_a^{\beta\text{-car}}$, is given by:

$$\mu_a^{\beta-car}(\lambda) = \log 10 \cdot [\beta car] \cdot \varepsilon_{\beta-car}(\lambda), \quad (5.12)$$

where [βcar] is the concentration of β-carotene in mg/ml, and $\varepsilon_{\beta\text{-car}}$ is its extinction coefficient.[12]

5.1.1.i Model fitting

Reflectance spectra were fit over the range of 350-750 nm using a constrained nonlinear least-squares fitting algorithm. First, calibrated diffuse reflectance spectrum, DRS, is calculated by the following formula:

$$DRS(\lambda) = \frac{data - background}{spectralon - background} * SpecCal \quad (5.13)$$

where, data, background and spectralon are in counts. *SpecCal* denotes the fraction of the light reflected by the spectralon reflectance standard and is an intrinsic property of the material. The values for *SpecCal* were provided by the manufacturer.

The standard deviation in counts as a function of wavelength, $\sigma_i(\lambda)$, is recorded during acquisition of data as well as for the calibration spectra. The error in DRS, $\delta(\lambda)$, is calculated with the propagation of error formula given below.

$$\delta(\lambda) = \sqrt{\sum_i \left(\frac{\partial DRS(\lambda)}{\partial x_i} \sigma_i(\lambda) \right)^2}$$
$$= \sqrt{\left(\frac{\partial DRS(\lambda)}{\partial data} \sigma_{data}(\lambda) \right)^2 + \left(\frac{\partial DRS(\lambda)}{\partial bgrd} \sigma_{bgrd}(\lambda) \right)^2 + \left(\frac{\partial DRS(\lambda)}{\partial spec} \sigma_{spec}(\lambda) \right)^2} \quad (5.14)$$

where i = data, background, spectralon, and $\sigma_i(\lambda)$ is the standard deviation in counts. This error is used in the expression for chi-square, χ^2:

$$\chi^2 = \sum_\lambda \left(\frac{DRS(\lambda) - Fit(\lambda)}{\delta(\lambda)} \right)^2 \quad (5.15)$$

The best fit (Zonios model) to DRS is found by minimization of χ^2.

We derive 7 parameters from modeling contact probe tissue reflectance: A [mm^{-1}], B, C [mm^{-1}], Hb [mg/ml], α, bvr [mm], and β-car [mg/ml].

5.1.2 Intrinsic Fluorescence Spectroscopy (IFS)

Intrinsic fluorescence spectroscopy (IFS) extracts the naturally occurring fluorescence emitted by tissue fluorophores, from the observed bulk fluorescence, which can be significantly distorted by absorption and scattering events in the turbid media. Fluorescence and reflectance spectra from the same spot of tissue are analyzed together using a photon-migration based model developed in our laboratory.[13] This model uses probabilistic concepts to describe light propagation in the tissue and it is based on the fact that the diffusely reflected and fluorescent photons undergo similar scattering and absorption events as they travel through the tissue.

In photon migration theory, light propagation in a turbid medium is described by photons traveling in paths with discrete nodes, at which absorption, scattering, and

fluorescence events occur. In this picture, reflectance is related to the product of albedo *a*, which represents the fraction of unabsorbed photons at each interaction event, and the escape probability of a photon that enters the medium, undergoes *n* scattering events, and is collected after exciting, ρ_n. The reflectance, *R*, can de described by a following expression:

$$R(\lambda) = \sum_{n=1}^{\infty} a^n \rho_n \tag{5.16}$$

where $a = \dfrac{\mu_s}{\mu_s + \mu_a}$,

and μ_s is a scattering coefficient.

An analytical expression for ρ_n, was derived based on Monte Carlo simulations by Wu *et al*[14]., modified by Zhang *et al.,* and given as follows:

$$\rho_n = \alpha \cdot \exp(-\beta n). \tag{5.17}$$

where

$$\beta = S(1-g), \quad \alpha = R_0 \cdot \varepsilon, \quad \text{and} \quad \varepsilon = \exp(\beta) - 1. \tag{5.18}$$

The parameter *S* is a constant related to the probe geometry, *g* is the anisotropy parameter of the medium, and R_0 is the reflectance in the absence of the absorption.

When fluorescence is considered, excitation light is absorbed after an initial *i* scattering events at the excitation wavelength, the fluorescence occurs at the $(i+1)^{th}$ node, and the fluorescence photon undergoes *n*-*i*-1 scattering events at the emission wavelength, where *n* is the total number of scattering events. The measured fluorescence can be defined as follows:

$$F_{xm} = \sum_{n=1}^{\infty} \sum_{i=0}^{n-1} a_x^{\,i+1} \cdot \frac{f_{xm}}{\mu_{sx} \cdot l} \cdot a_m^{n-i-1} \rho_{ni} \tag{5.19}$$

The fluorescence escape probability is once again derived based on Monte Carlo simulations by Wu *et al*[14]., modified by Zhang *et al.,* and given as follows:

$$\rho_{ni} = (\alpha_x \alpha_m)^{1/2} \exp[-\beta(i+1)] \exp[-\beta_m (n-i-1)]. \tag{5.20}$$

The quantity f_{xm} is intrinsic fluorescence and is given by:

$$f_{xm} = \left(\frac{I_x}{h\nu_x} \right) \mu_{fx} l \phi_{xm} h\nu_m . \tag{5.21}$$

The subscripts x and m correspond to the dependence of the quantities on the excitation and emission wavelengths, respectively. The intensity of the incident light is denoted by I, h is Planck's constant, and ν is frequency of light. The absorption coefficient of the fluorophore and its quantum yield are denoted by μ_f and Φ, respectively. The constant l has dimension of length and characterizes a given light delivery-collection geometry; it is, therefore, probe-specific. By combining the equations for R (λ), F_{xm}, ρ_n, and ρ_{ni} we obtain the formula for the intrinsic fluorescence as follows:

$$f_{xm} = \frac{F_{xm}}{\frac{1}{\mu_{sx} l} \cdot \left(\frac{R_{0x} R_{0m}}{\varepsilon_x \varepsilon_m} \right)^{1/2} \cdot \frac{R_x}{R_{0x}} \cdot \left(\frac{R_m}{R_{0m}} + \varepsilon_m \right)} \tag{5.22}$$

This expression is the basis for IFS method, which enables the intrinsic fluorescence spectrum to be extracted from the measured fluorescence, by use of the diffuse reflectance collected from a given tissue site with the same probe. The model assumes a homogeneous turbid medium. Furthermore, subsequent secondary absorption of fluorescence that occurs within the medium is not accounted for.

The intrinsic fluorescence of the tissue, once obtained, may be linearly decomposed into its molecular constituents. The spectrum of epithelial tissue intrinsic fluorescence is modeled as a linear combination of tissue fluorophore basis spectra. The basis spectra were extracted from the intrinsic fluorescence spectra using multivariate curve resolution (MCR). In order to reduce patient-to-patient variation in fluorescence spectra, the areas under the IFS spectra, as well as basis spectra, were normalized to a value of one. For 340 nm excitation, the wavelength that we focus on in this thesis, the intrinsic fluorescence was modeled as a linear combination of two fluorophores, the reduced form of nicotinamide adenine

dinucleotide (NADH) and collagen (Coll). From fitting the IFS spectra we extract the fractional contribution of these two components.

5.1.3 Light Scattering Spectroscopy (LSS)

Light Scattering Spectroscopy (LSS), developed in our laboratory by Perelman et al.[15], uses the information conveyed in the singly-scattered light from tissue to measure the size distribution of epithelial nuclei. According to Perelman et al. the difference between the observed and modeled diffuse reflectance spectra of tissue is attributed to single elastic light scattering from epithelial nuclei, and diagnostic information due to changes in nuclear size and density are extracted from it. LSS has been shown to be a promising technique for *in vivo* diagnosis of dysplasia in several pilot studies.[16,17]

After an in depth investigation of this model, a number of findings were discovered that provided strong evidence that this technique is not reliable. While the initial studies and development of this technique were based on work with cells, it was found that in tissue, imperfect modeling of hemoglobin absorption using the DRS model resulted in hemoglobin absorption features in the residual signal. The actual single scattering signal arising from epithelial nuclear scattering is much smaller than this residual spectrum and does not contain van de Hulst oscillations in wavelength.[7] Rather, this residual spectrum largely arises from the assumption of a uniform distribution of hemoglobin in the tissue. In fact, blood and hemoglobin are packaged in finite size blood vessels, which alters the diffuse reflectance. When we include vessel packaging, which accounts for the inhomogeneous distribution of hemoglobin in the diffuse reflectance model, the diffuse reflectance is modeled more accurately, greatly reducing the size of the residual spectrum. These findings are verified via numerical estimates based on light propagation and Mie theory, and analysis of published light scattering spectroscopy and tri-modal spectroscopy data measured from Barrett's esophagus patients.[1]

Furthermore, we generated numerical (synthetic) reflectance data using parameters consistent with those obtained from clinical data as inputs into the Zonios reflectance mode (Eq 5.4). Using the Zonios reflectance model we generated spectra

which incorporated vessel packing into the description of the absorption coefficient. The parameters describing the scattering and absorption coefficients respectively were chosen to mimic the parameters obtained from analyzing the data. Random Gaussian noise was added to all the spectra in the amounts typically found in clinical data measured from tissue. This synthetic reflectance data then was fit over the range from 350-750 nm using the Zonios model, however vessel packaging was not included in the model. The model-based LSS analysis was performed on the residual over the range from 380-700 nm.

Because the model did not account for the vessel packaging effects present in this data set, the residual contained features attributed to ill-fitting of the hemoglobin bands. This residual, although containing only hemoglobin features and noise, generates an apparent LSS signal. The mean diameter and nuclear magnitude parameters were very similar to values obtained from analysis of tissue data. Furthermore, when no hemoglobin features are present, only noise, the parameters extracted for mean diameter and standard deviation are again consistent with values derived from tissue data. The parameters extracted were most significantly affected by the wavelength range used in the LSS analysis as well as by the absorption properties and magnitude and wavelength-dependence (shape) of the noise.

From the evidence mentioned above, it was decided that the LSS technique was not a robust method and the signal generated using the model-based approach was unlikely to be due to epithelial nuclei. Therefore only DRS and IFS were used in the present work.

5.2 Statistical Methods

Two-sided Wilcoxon Rank Sum test is used to test the hypothesis that the extracted spectroscopic parameter distributions of two different tissue groups (i.e. different according to anatomy or disease diagnosis) were different. A p-value of < 0.05 was considered significant.

The spectral algorithms were developed by using logistic regression models based on a combination of significant spectroscopic parameters providing the most

important discriminative information. Logistic regression is a statistical method that calculates regression coefficients using maximum likelihood estimation (MLE) after transforming the dichotomous dependent variable (e.g., HSIL or non-HSIL) into a logit variable (the natural log of the odds of HSIL occurring). The likelihood of a logistic regression model is the probability that the observed value of the dependent variable may be predicted from the observed values of spectroscopic parameters, and is calculated using the MLE.

The likelihood ratio test was used to assess the significance of each of the spectroscopic parameters in the logistic regression model.[18] A p-value<0.05 was considered to be significant. The likelihood ratio test calculated the improvement in the model fit that the spectroscopic parameters made compared to the null model in which none of the parameters contributed to predicting the odds of the dependent variable (e.g. HSIL) occurring. The log of the likelihood ratio (LLR), defined as -2ln(likelihood ratio), was compared to the critical value of the chi-squared distribution (p-value = 0.05) in order to determine the significance of the increase in likelihood.

The likelihood ratio test determined the significance of an overall logistic model but did not asses which particular spectroscopic parameters carried the most discriminative power. In order to determine the significance of individual spectroscopic parameters in a model, a nested likelihood ratio test was used. Both forward and backward-elimination likelihood ratio tests were employed. This was done by calculating the LLR of the nested model which adds or drops one of the spectroscopic parameters to the overall model and comparing it to the critical value of the chi-squared distribution. The critical value of chi-square distribution was calculated for a p-value of 0.05 and 1 degree of freedom. If the chi-square value was above the critical value, then it was concluded that the spectroscopic parameter added or dropped in the nested model contributed significantly in predicting the odds of dependent variable occurring.

Leave-one-out cross-validation (LCV) was used to construct receiver-operator characteristic (ROC) curves for the spectral algorithms. LCV is a statistical validation

method applied in cases of the limited number of samples available for constructing a training set and test set for the evaluation of the performance of a classifier. LCV is performed by dividing the total number of samples, *n*, into two groups: a test set composed of a single sample, and a training set comprised of the remaining *n*-1 samples. The diagnostic algorithm developed from the training set is then applied to the test case. This procedure is repeated until each of the *n* samples are sequentially omitted and treated as the test case.

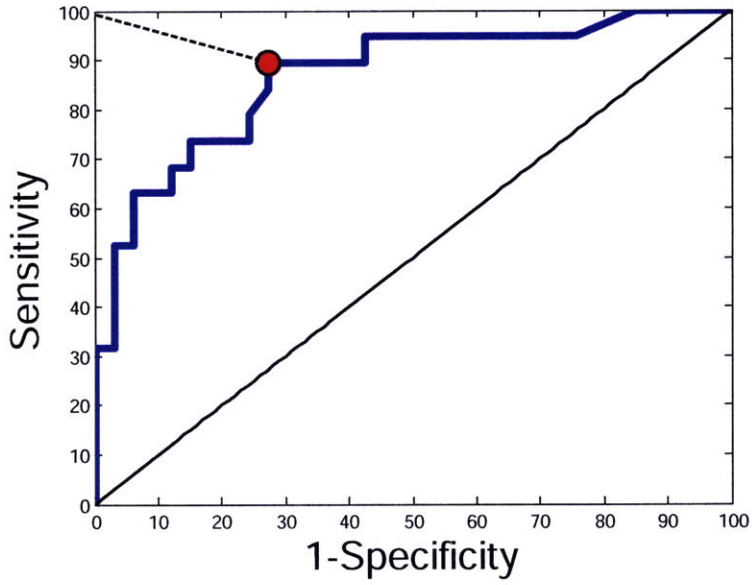

Figure 5.2.1. An example of the ROC curve. ROC curve (blue line), the 45° line (AUC=0.5) (black line), the point of representative sensitivity/specificity (red circle), and the shortest distance from the point of perfect separation (black dashed line).

The ROC curve [see Figure 5.2.1.] is a plot of sensitivity (true positive rate) against the 1-specificity (false positive rate) for a range of cutoff points (probability thresholds). The discrimination ability was evaluated by the area under the ROC curve (AUC), as well as the sensitivity and specificity. The AUC represents the overall accuracy of the model across the entire range of thresholds. Perfect separation is characterized by an AUC value of 1, and the inability to differentiate between two

groups is characterized by an AUC value of 0.5 [45° line in Figure 5.2.1.]. In the following, we report a point on the ROC curve which is the shortest distance away from the point of perfect separation (100% sensitivity and 100% specificity) defined by:

$$\min\left[\sqrt{\left(1-\frac{sensitivity}{100}\right)^2+\left(1-\frac{specificity}{100}\right)^2}\right]. \qquad (6)$$

We refer to this point whenever we quote sensitivity and specificity values.

5.3 Clinical *In Vivo* Study Design

The clinical *in-vivo* studies were conducted at the Boston Medical Center (BMC). The protocols for both contact-probe and the imaging studies were approved by the Institutional Review Boards of BMC, as well as by the Committee On the Use of Humans as Experimental Subjects of the Massachusetts Institute of Technology.

5.3.1 Contact-probe study

5.3.1.i Data collection

The contact probe *in vivo* study involved 43 patients undergoing colposcopic evaluation following an abnormal Pap smear, including atypical squamous cells of undetermined significance (ASC-US), atypical squamous cells- cannot exclude HSIL (ASC-H), LSIL, and HSIL. For each patient, reflectance and fluorescence spectra were collected from a colposcopically normal squamous (CNS) site as well as abnormal sites using a fiber optic based clinical device developed by our laboratory known as the Fast Excitation Emission Matrix (FastEEM). The instrument and the calibration procedures are described in Chapter 4. The optical fiber probe, which samples an area of tissue ~1 mm in diameter, was disinfected with CIDEX OPA (Advanced Sterilization Products, Irvine, CA) before each procedure. After the application of acetic acid (5% solution) to the cervix during colposcopy, the probe was brought into gentle contact with the tissue. Each measurement which consisted of the average of 5 sets of white light reflectance spectra (300-800 nm emission) and 5 sets of 9 fluorescence spectra (308-460 nm excitation) was acquired in

approximately 3s. The standard deviation of the 5 spectra was also recorded. A set of 2-3 measurements were acquired for each tissue site. Colposcopically abnormal sites were then biopsied and evaluated by histopathology. Clinically normal sites were not biopsied.

5.3.1.ii Histopathology

Each biopsy specimen underwent standard histopathological processing. The hematoxylin and eosin stained tissue sections were evaluated by three experienced pathologists using standard diagnostic criteria. We used consensus diagnosis (agreement of two of the three pathologists) to determine the disease diagnosis of the study samples. Each biopsied site was classified as either HSIL or non-HSIL (negative for SIL or LSIL).

All sites were further examined by a single pathologist for the absence or presence of features consistent with the transformation zone. If the stroma (the connective tissue underlying the epithelium) of a particular site was visible on the

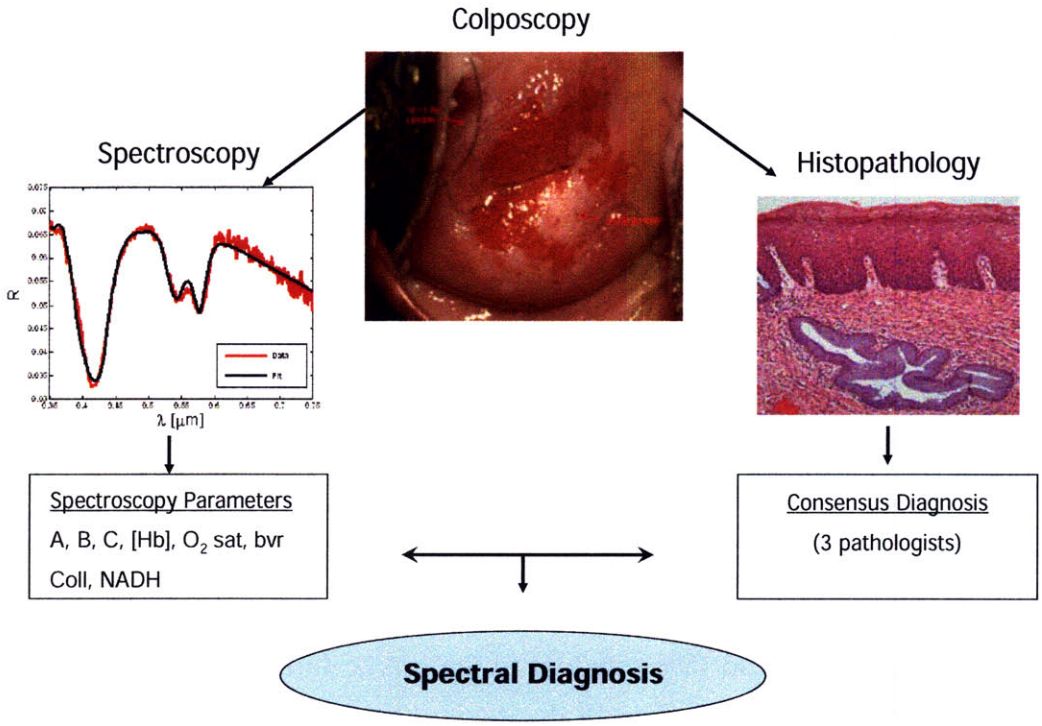

Figure 5.3.1. Contact-probe study design.

histology slide, we performed a qualitative assessment via microscopy of the percentage of stroma occupied by glands. Each site was classified as either having a significant content of stromal gland (SG) or a minimum glandular content (non-SG) based on whether ≥25% or <25% of the stroma was occupied by glands.

The average epithelial thickness was measured with with Zeiss Axio Imager 2.0.0.0. software and defined by an average value of three measurements across the squamous epithelium. Finally, we used two immunohistochemistry stains, p16 and Ki-67, which when used in combination are sensitive and specific biomarker of cervical SIL.

5.3.2 Imaging study

5.3.2.i Data collection

In vivo imaging data was acquired using the QSI device from patients who were referred for colposcopy or LEEP due to prior abnormal Papsmear or biopsy results. For each patient, reflectance and fluorescence spectra from the entire cervix (2.1 cm x 2.1 cm area of the cervix with 441 interrogation points) were obtained

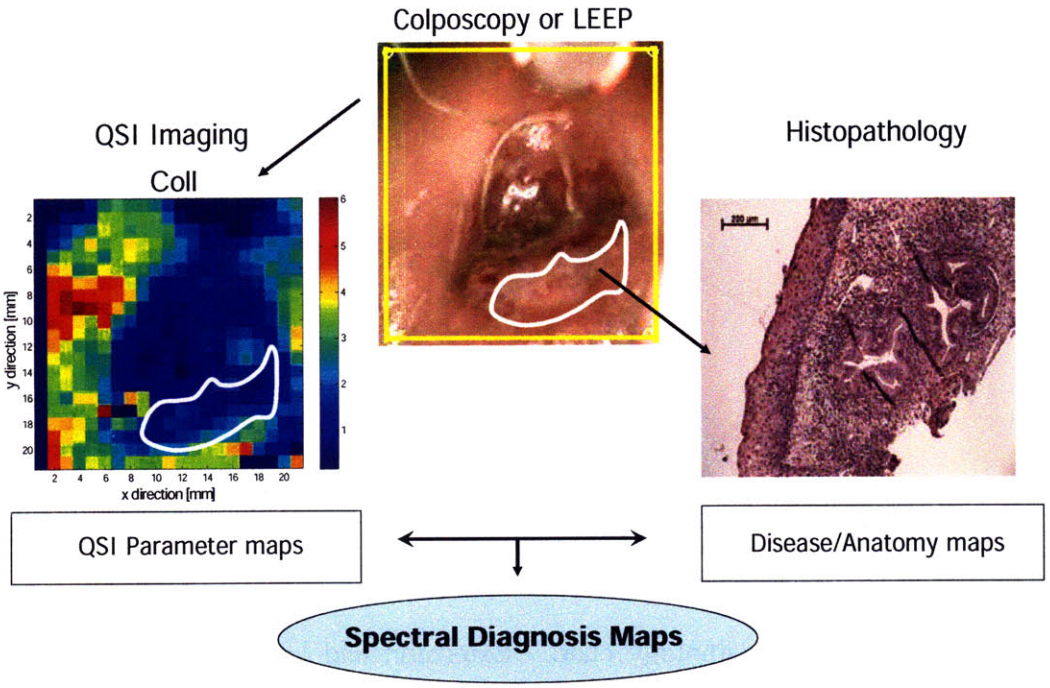

Figure 5.3.2. Imaging study design.

before and after the application of acetic acid (5 %). The total acquisition time was approximately 90 seconds.

5.3.2.ii Histology

Upon submission to pathology, the LEEP specimens were cut into twelve pieces corresponding to the 12 clock directions per standard of care. From each piece a section extending from endocervix through the transformation zone to ectocervix was prepared for evaluation under a microscope. For each section, a single pathologist recorded the extent and location of any HSIL present with millimeter precision. The location and the extent of the endocervix, transformation zone and the ectocervix

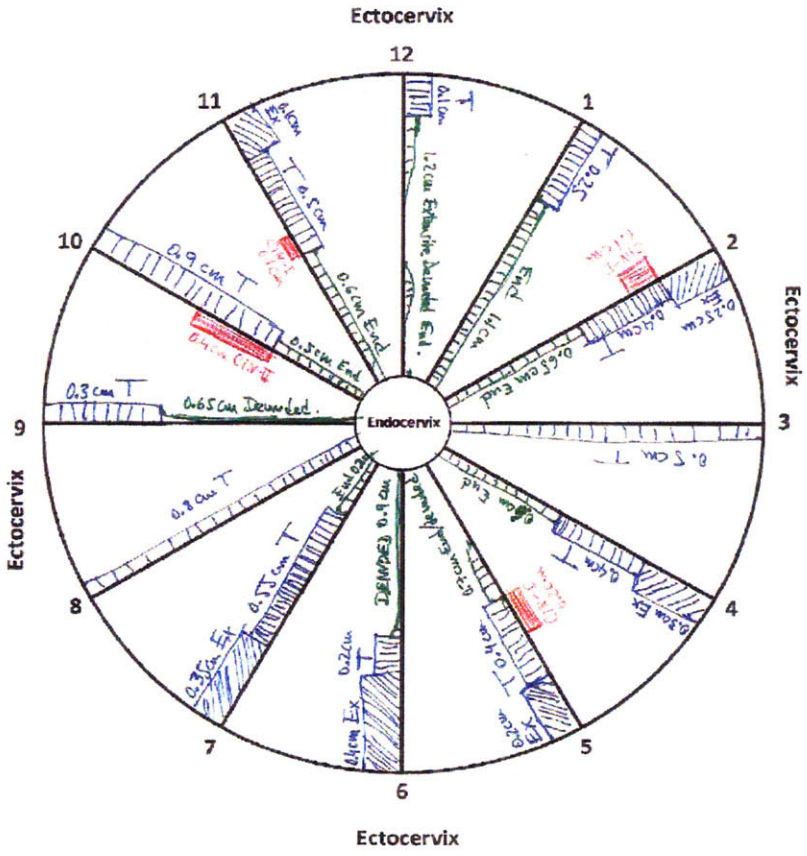

Figure 5.3.3. LEEP pathology chart. Extension and location of (a) endocervix – green, (b) transformation zone – blue parallel lines, (c) ectocervix – blue slanted lines, and (d) HSIL – red

were also recorded. As shown in Figure 5.3.3., the end result was a combined anatomy/disease map showing the location of cervical tissue zones, as well as the location of HSIL on the cervix.

5.3.3 Development and testing of spectroscopic algorithms

The clinical studies have accomplished five aims: 1) to identify changes in spectroscopic parameters between different zones of the cervix; 2) to examine the impact of grouping clinically normal squamous sites (CNS) and clinically suspicious non-HSIL sites on the performance of diagnostic algorithms for identifying HSIL sites; 3) to develop an algorithm based on spectroscopic parameters to differentiate HSIL from non-HSIL within clinically suspicious sites; 4) to examine the effect of stromal glandularity on the spectroscopic parameters; and 5) to extend contact probe studies into imaging studies.

5.4 References

1. A. Blaustein and R. J. Kurman, *Blaustein's pathology of the female genital tract*, Springer, New York (2002)
2. R. Kalluri and M. Zeisberg, "Fibroblasts in cancer," *Nature Reviews Cancer* **6** (5), 392-401 (2006).
3. H. Nagase and J. F. Woessner, "Matrix metalloproteinases," *Journal of Biological Chemistry* **274** (31), 21491-21494 (1999).
4. J. Mazibrada, M. Ritta, M. Mondini, M. De Andrea, B. Azzimonti, C. Borgogna, M. Ciotti, A. Orlando, N. Surico, L. Chiusa, S. Landolfo and M. Garigho, "Interaction between inflammation and angiogenesis during different stages of cervical carcinogenesis," *Gynecologic Oncology* **108** (1), 112-120 (2008).
5. G. Zonios, L. T. Perelman, V. M. Backman, R. Manoharan, M. Fitzmaurice, J. Van Dam and M. S. Feld, "Diffuse reflectance spectroscopy of human adenomatous colon polyps in vivo," *Applied Optics* **38** (31), 6628-6637 (1999).
6. T. J. Farrell, M. S. Patterson and B. Wilson, "A Diffusion-Theory Model of Spatially Resolved, Steady-State Diffuse Reflectance for the Noninvasive Determination of Tissue Optical-Properties Invivo," *Medical Physics* **19** (4), 879-888 (1992).
7. C. Lau, O. Scepanovic, J. Mirkovic, S. McGee, C.-C. Yu, S. Fulghum Jr., M. Wallace, J. Tunnell, K. Bechtel and M. S. Feld, "Re-evaluation of model-based LSS for tissue spectroscopy," *Journal of Biomedical Optics* (2008).
8. R. L. P. van Veen, W. Verkruysse and H. J. C. M. Sterenborg, "Diffuse-reflectance spectroscopy from 500 to 1060 nm by correction for

inhomogeneously distributed absorbers," *Optics Letters* **27** (4), 246-248 (2002).

9. L. O. Svaasand, E. J. Fiskerstrand, G. Kopstad, L. T. Norvang, E. K. Svaasand, J. S. Nelson and M. W. Berns, "Therapeutic response during pulsed laser treatment of port-wine stains: Dependence on vessel diameter and depth in dermis," *Lasers in Medical Science* **10** (4), 235-243 (1995).
10. S. Prahl, "Optical Absorption of Hemoglobin,"
11. C. H. Best, N. B. Taylor and J. B. West, *Best and Taylor's physiological basis of medical practice*, Williams & Wilkins, Baltimore (1991)
12. H. Du, R. C. A. Fuh, J. Z. Li, L. A. Corkan and J. S. Lindsey, "PhotochemCAD: A computer-aided design and research tool in photochemistry," *Photochemistry and Photobiology* **68** (2), 141-142 (1998).
13. I. Georgakoudi, B. C. Jacobson, J. Van Dam, V. Backman, M. B. Wallace, M. G. Muller, Q. Zhang, K. Badizadegan, D. Sun, G. A. Thomas, L. T. Perelman and M. S. Feld, "Fluorescence, reflectance, and light-scattering spectroscopy for evaluating dysplasia in patients with Barrett's esophagus," *Gastroenterology* **120** (7), 1620-1629 (2001).
14. J. Wu, M. S. Feld and R. P. Rava, "Analytical Model for Extracting Intrinsic Fluorescence in Turbid Media," *Applied Optics* **32** (19), 3585-3595 (1993).
15. L. T. Perelman, V. Backman, M. Wallace, G. Zonios, R. Manoharan, A. Nusrat, S. Shields, M. Seiler, C. Lima, T. Hamano, I. Itzkan, J. Van Dam, J. M. Crawford and M. S. Feld, "Observation of periodic fine structure in reflectance from biological tissue: A new technique for measuring nuclear size distribution," *Physical Review Letters* **80** (3), 627-630 (1998).
16. I. Georgakoudi, B. C. Jacobson, J. Van Dam, V. Backman, M. B. Wallace, M. G. Muller, Q. Zhang, K. Badizadegan, D. Sun, G. A. Thomas, L. T. Perelman and M. S. Feld, "Fluorescence, reflectance, and light-scattering spectroscopy for evaluating dysplasia in patients with Barrett's esophagus," *Gastroenterology* **120** (7), 1620-1629 (2001).
17. M. G. Muller, T. A. Valdez, I. Georgakoudi, V. Backman, C. Fuentes, S. Kabani, N. Laver, Z. M. Wang, C. W. Boone, R. R. Dasari, S. M. Shapshay and M. S. Feld, "Spectroscopic detection and evaluation of morphologic and biochemical changes in early human oral carcinoma," *Cancer* **97** (7), 1681-1692 (2003).
18. D. G. Kleinbaum, *Logistic regression : a self-learning text*, Springer, New York (1994)

CHAPTER 6

Quantitative spectroscopy for detecting cervical dysplasia: Impact of anatomy

In this chapter we investigate the effects of cervical tissue anatomy on reflectance and fluorescence spectroscopy measurements, with an aim to facilitate development of a diagnostic algorithm free of the confounding effects of anatomy. We use spectroscopy in both contact probe and imaging modes to study patients undergoing either colposcopic examination or treatment via Loop Electrosurgical Excision Procedure (LEEP) for uterine cervical squamous neoplasia. Physical models of light propagation in tissue were used to fit the spectra and to extract parameters related to tissue morphology and biochemistry. We present evidence that sites collected in the transformation zone, the area in which the vast majority of high grade squamous intraepithelial lesions (HSILs) are found, are spectroscopically distinct from the squamous sites, even in the absence of disease. We demonstrate that the apparent performance of diagnostic algorithms for identifying HSILs is enhanced when clinically normal squamous sites are included, as a result of normal anatomic differences. Based on our findings, including clinically normal squamous sites into the data set which is used to evaluate the performance of the algorithm for detection of HSIL is a confounding artifact that artificially increases performance values with respect to the key differentiation to be made, namely distinguishing HSILs from clinically suspicious non-HSILs.

6.1 Motivation

The effectiveness of reflectance and fluorescence spectroscopy for non-invasive *in vivo* diagnosis of cervical squamous intraepithelial lesions (SILs) has been extensively evaluated. Contact probes, as well as imaging techniques with wide-area surveillance capabilities, have been tested clinically in various stages, from pilot to phase III clinical studies.[1-10] The results show the potential of reflectance and fluorescence spectroscopy, individually or in combination, to improve the effectiveness of disease detection.

As we have already discussed in Chapter 3, the sources of spectroscopic contrast in tissue reflectance and fluorescence due to the presence of disease are related to the changes that accompany cervical dysplasia, including loss of differentiation of the epithelial cells[11], degradation and reorganization of stromal collagen by matrix metalloproteinase activity[12,13], and angiogenesis[14]. However, cervical tissue spectroscopy is not only affected by disease, but also by age[15,16], menopausal status[16,17], time after the application of acetic acid[8], and normal variations in cervical anatomy[2,10,16]. For example, spectroscopic differences between normal ectocervix and endocervix have been noted previously[2,10] and explained by differences in anatomy. Another important source of normal variations in anatomy are the dynamic changes that occur in the cervix during reproductive life, namely the process of squamous metaplasia in the transformation zone of the cervix.[11,18]

Although a minority of cervical neoplasias is found in the ectocervix, the vast majority of clinically significant neoplastic lesions (high grade intraepithelial lesions, HSILs) are found within the transformation zone.[11] Normal anatomical variations between the transformation zone and normal squamous epithelium should be reflected in tissue spectroscopy and, if significant, must be accounted for when developing diagnostic algorithms. Furthermore, normal ectocervix and endocervix are easily identified by colposcopic examination.[19] Therefore, in order to improve the accuracy of clinical HSIL detection, spectroscopy must be able to identify HSILs within the transformation zone. In order to achieve this goal, spectroscopy must be able to

reliably resolve the disease process in the context of the background microanatomic complexity inherent in the cervix.

Historically, spectroscopic studies have included clinically normal squamous sites, either non-biopsied or histopathologically confirmed, in the validation set for diagnosing HSILs[2,4,6,8,10]. Mourant et al.[7] and Georgakoudi et al.[3] noted an apparent increase in diagnostic power when clinically normal tissues were included in the validation set. Georgakoudi et al.[3] also noted that normal squamous tissue and the transformation zone had different spectroscopic properties, consistent with Freeberg et al.[16] observation that tissue type influences both reflectance and fluorescence measurements. Freeberg et al. concluded that understanding the effects of anatomy on spectroscopy may have a significant impact on diagnostic algorithm development. Nevertheless, this has not been further explored and the reasons for differences in diagnostic power when clinically normal tissues were included have not been explained.

In this study we investigate the effects of cervical anatomy on spectroscopy with an aim to facilitate the development of a diagnostic algorithm free of the confounding effects of cervical anatomy.

6.2 Methods

We study patients undergoing colposcopic examination using reflectance and fluorescence in the contact probe mode. Chapter 7 discusses the development of the algorithm for HSIL detection free of the confounding effects of cervical anatomy, and Chapter 8 describes how these studies were extended to the imaging mode using quantitative spectroscopy imaging (QSI). While the emphasis of this chapter is on contact probe data, we also use our imaging data to support conclusions of the contact probe study. Information about the FastEEM instrument used in the contact probe study and QSI instrument is given in Chapter 4. The details of the clinical study design and data modeling are given in Chapter 5. Physical models were used to fit the spectra and extract parameters related to tissue morphology and biochemistry. The extracted parameters were then used to develop spectroscopic algorithms with two broad aims: 1) to identify changes in spectroscopic parameters due to anatomy, and 2)

to examine the effects of anatomy on the apparent performance of diagnostic algorithms for identifying HSILs.

To identify changes in spectroscopic parameters between different zones of the cervix, we studied data from both contact probe and imaging patients. Tissue parameters were correlated to histopathology diagnosis for all data collected from the imaging patients and clinically suspicious sites from the probe data set. In the case of contact probe CNS sites, tissue parameters were correlated to clinical impression. A two-sided Wilcoxon Rank Sum test was used to test the hypothesis that the extracted spectroscopic parameter distributions of different tissue zones or different groups of sites were different. A p-value of < 0.05 was considered significant. The spectral algorithms were developed by using logistic regression models based on a combination of significant spectroscopic parameters providing the most important diagnostic information. Leave-one-out cross-validation (LCV) was used to construct receiver-operator characteristic (ROC) curves for the spectral algorithms.

To examine the impact of grouping CNS sites and clinically suspicious non-HSIL sites on the performance of diagnostic algorithms for identifying HSIL sites, we constructed and tested 5 data sets with varying percentages of CNS sites. For each percentage of CNS sites, we determined the significant parameters that differentiate HSIL sites from everything else (biopsied non-HSIL sites and CNS). In order to evaluate the discrimination ability based on absorption, scattering and fluorescence separately, we first tested a logistic regression algorithm based on each of the parameters alone. Next, we developed a logistic regression model based on a combination of significant spectroscopic parameters providing the highest diagnostic power.

6.3 Results

6.3.1 Data Set

As shown in Table 6.3.1., our contact probe data set consisted of 33 CNS sites, which were not biopsied, and 51 clinically suspicious biopsied sites, out of which histopathology determined that 30 sites were negative for SIL, 12 sites were

LSILs, and 9 sites were HSILs. For the purposes of developing a diagnostic algorithm which aims to detect HSIL sites, the negative for SIL sites and the LSIL sites were combined-- we refer to these in the following as non-HSIL sites. We note that these non-HSIL sites do not include the 33 CNS sites. The imaging data set consisted of 2 LEEP patients which were free of disease by histopathology.

Table 6.3.1. Contact probe data set

Clinical Category	Histology Category		# Sites
Normal (CNS)	Not biopsied		33
Suspicious	non-HSIL	Negative for SIL	30
		LSIL	12
	HSIL		9

6.3.2 Microscopic characterization of site location

Histopathology evaluation confirmed that 36 of all biopsied study sites were from the transformation zone. The histopathology features consistent with transformation zone were not found for only 6 sites. For 9 biopsied sites stroma was not visible on the histology slides, and it was impossible to confirm that the samples were in the transformation zone by histopathology. All of the HSIL sites but one for which stroma was not visible on the histology slide came from the transformation zone.

6.3.3 *Spectral comparison of normal squamous and normal transformation zone sites*

In order to determine the spectroscopic differences between normal squamous epithelium and the transformation zone, we studied data collected from both contact probe and imaging patients.

Contact Probe Results In order to determine the spectroscopic differences between the transformation zone and the normal squamous epithelium, we studied the normal

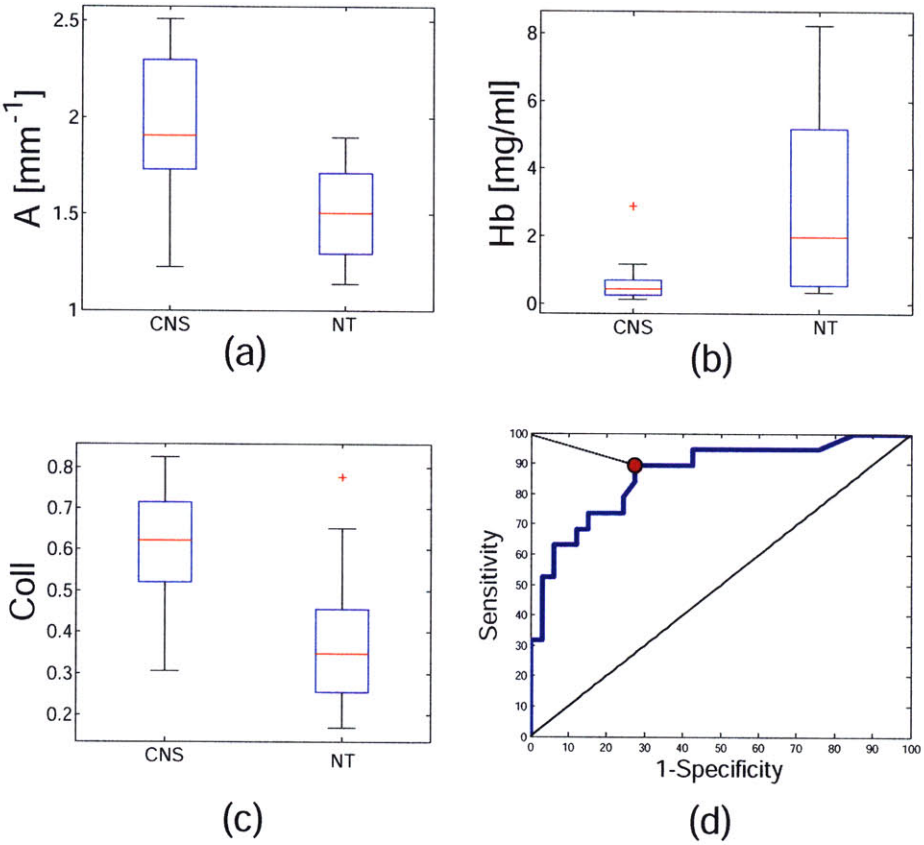

Figure 6.3.1. Discrimination of CNS from NT using contact probe data. Box plots of: (a) A parameter [mm^{-1}], (b) Hemoglobin concentration (Hb) [mg/ml], (c) fraction of IFS due to collagen (Coll); (d) LCV ROC plot for the logistic regression algorithm differentiating CNS from NT based on Coll and Hb: ROC curve (blue line), the 45° line (AUC=0.5) (black line), the point of representative sensitivity/specificity (red circle), and the shortest distance from the point of perfect separation (black dashed line).

transformation zone sites, which we refer to in following as NT sites and the CNS sites. NT sites, by histopathology, had no signs of dysplasia (LSIL or HSIL) and were confirmed to be in the transformation zone. Based on the Wilcoxon Rank Sum test, the values of majority of the extracted parameters were significantly different

between the CNS sites and NT sites. The CNS sites exhibited higher values of Coll and A parameters, and lower values of C parameter, Hb, α, β-carotene, and bvr than NT sites. When logistic regression and LCV were performed, CNS could be differentiated from NT based on Coll and Hb, with an AUC, sensitivity and specificity of 0.87, 90%, and 73% respectively. The contribution of other parameters to the diagnostic performance was negligible. The box plots of the three most significant parameters, A, Hb, and Coll parameters, as well as the ROC curve for differentiating CNS from NT, are shown in Figure 6.3.1.

Imaging Results Using the imaging data, we investigated the spectral differences

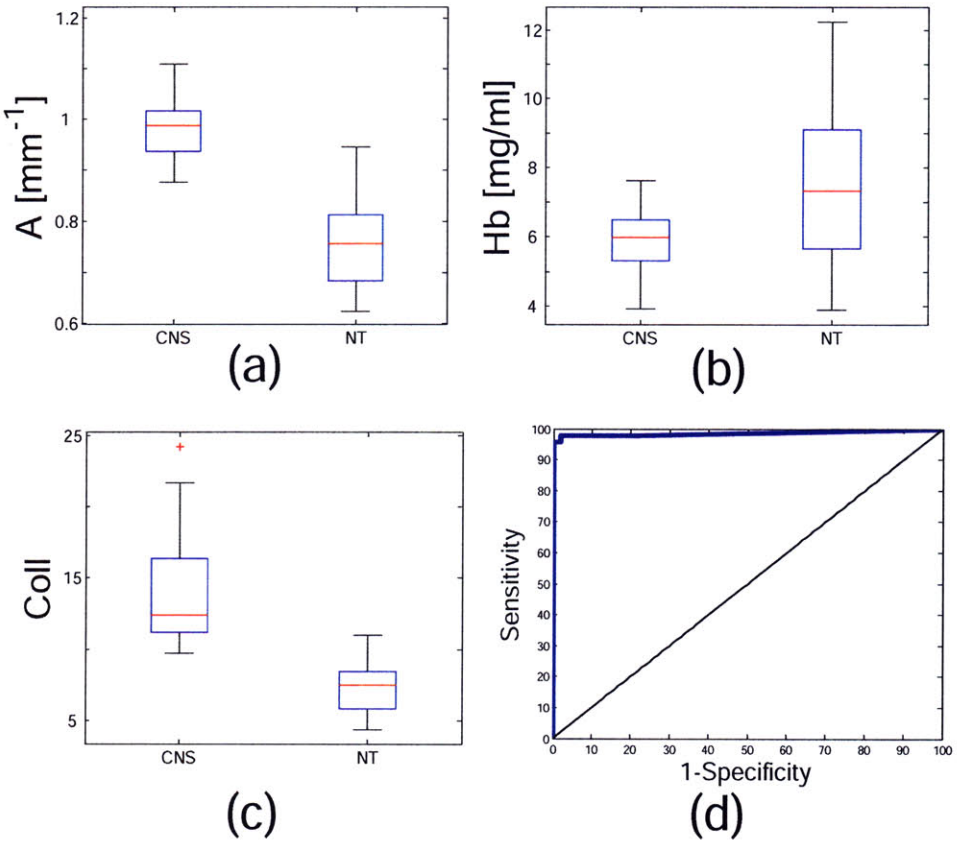

Figure 6.3.2. Discrimination of CNS from NT using imaging data. Box plots of: (a) A parameter, (b) Hb, (c) Coll; (same units as in Figure 1.) (d) LCV ROC curve for the logistic regression algorithm based on Coll and Hb for differentiating CNS from NT sites: ROC curve (full line), and the 45° line (AUC=0.5).

between CNS and NT sites. Data were collected from 2 LEEP patients, and the areas which were free of disease by both clinical impression and histopathology were evaluated. Based on the Wilcoxon Rank Sum test, all extracted reflectance and fluorescence parameters were significantly different between the CNS and NT sites. Just as in the case of the contact probe data, the CNS sites exhibit significantly higher values of Coll and A parameters and lower values of Hb and α than NT. Additionally, CNS sites exhibited higher values of B parameter than for the NT. When logistic regression and LCV were performed, CNS could be differentiated from the NT based on Coll and Hb, with an AUC, sensitivity and specificity of 0.98, 98%, and 98%, respectively. The box plots of the three most significant parameters, A, Hb , and Coll parameters, as well as the ROC curve for the logistic regression model for differentiating the CNS from the NT are shown in Figure 6.3.2.

6.3.4 *Spectral comparison of CNS, non-HSIL, and HSIL sites*

Based on the Wilcoxon Rank Sum test, a majority of the extracted parameters were significantly different for CNS and non-HSIL, as well as HSIL sites. Just as in the case of CNS vs. NT, the CNS sites exhibited higher values of Coll and A parameters and lower values of C, Hb, α, and bvr parameters than both non-HSIL and HSIL sites. When logistic regression and LCV were performed, non-HSIL sites could be differentiated from CNS sites using Coll and Hb parameters, with an AUC, sensitivity, and specificity of 0.88, 81% and 85%, respectively. With these same parameters, HSIL sites could be differentiated from CNS with an AUC, sensitivity, and specificity of 0.92, 89% and 97%, respectively. Box plots for the three most significant parameters, A, Coll, and Hb are shown in Figure 6.3.3 (a), (b), and (c), respectively. The corresponding ROC plots are shown in Figure 6.3.3 (d).

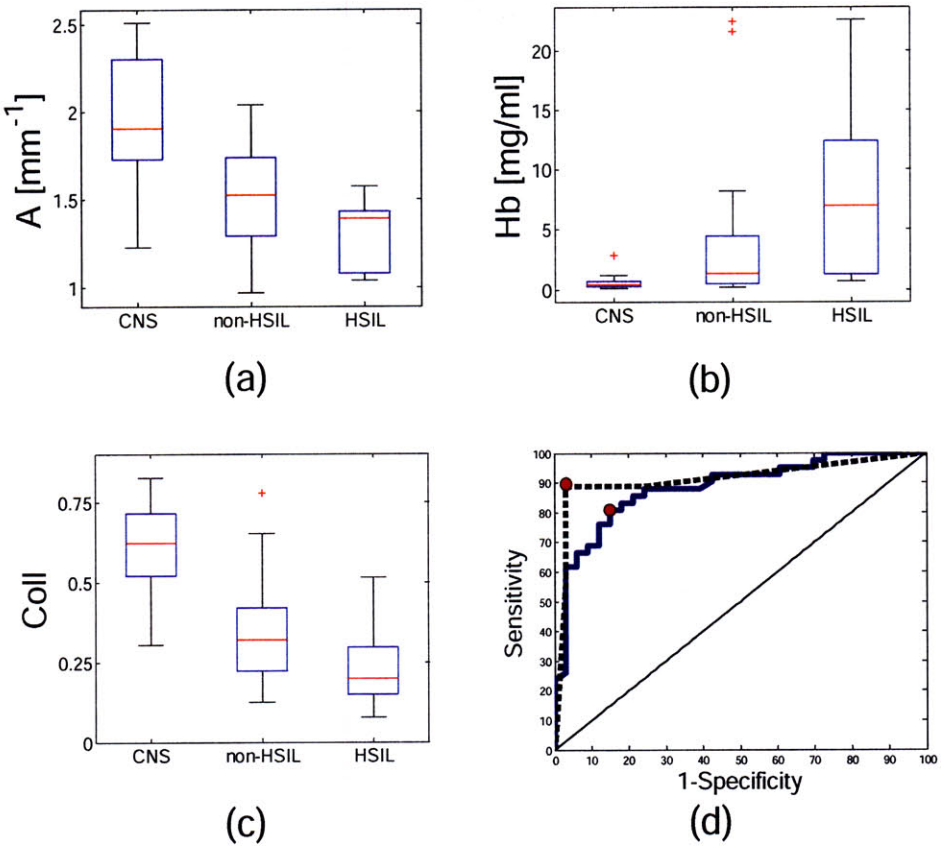

Figure 6.3.3. Discrimination of CNS from HSIL and non-HSIL. Box plots of (a) A parameter, (b) Hb, (c) Coll, (same units as in Figure 1.) and (d) LCV ROC curve for the logistic regression algorithm based on Coll and Hb for differentiating CNS sites from HSIL sites (back dashed line), and CNS sites from non-HSIL sites (full blue line), the 45° line (AUC=0.5) (black line), the points of representative sensitivity/specificity (red circles).

6.3.5 *Diagnostic performance for HSIL detection as a function of the percentage of CNS sites included in the test sample*

Because normal squamous sites are spectroscopically distinct from the transformation zone, and the majority of clinically suspicious sites (both HSIL and non-HSIL sites) are found in the transformation zone, we examined the impact of grouping CNS and non-HSIL sites on diagnostic algorithms for identifying HSIL sites. We constructed and tested 5 data sets with varying percentages of CNS sites.

For each data set we used the same 9 HSIL sites as the positive group, while the negative group contained percentages of CNS sites ranging from 0 to 100%, as shown in Table 6.3.2.

Table 6.3.2. Significant parameters for differentiating HSIL from negative sites (non-HSIL and CNS) as a function of the percentage of CNS sites included in the test sample.

CNS (% negative)	**0 %**	**25 %**	**50 %**	**80 %**	**100 %**
# non-HSIL / # CNS	42/0	42/14	33/33	8/33	0/33
Significant parameters	A, Hb, Coll	A, Hb, Coll	A, Hb, Coll, B	A, B, C, Hb, α, bvr Coll	A, B, C, Hb, α, bvr Coll

Table caption: We constructed the data sets by using all 33 CNS sites for the 100% group, and then randomly adding non-HSIL sites to create 80% and 50% groups. As we didn't have enough non-HSIL sites to create a 25% group while keeping all 33 CNS sites, we eliminated a certain amount of CNS sites to create this group. For 0% CNS we used all of the non-HSIL sites.

For each data set, we first determined the significant parameters for differentiating the positive (HSIL) group from the negative (non-HSIL and CNS) group using the Wilcoxon Rank Sum test. As shown in Table 3, non-HSIL sites (0 % CNS group) can be differentiated from HSIL by A, Hb, and Coll parameters. As the percentage of CNS in the negative group increased, the number of significant parameters increased. All spectroscopic parameters except β-carotene were significantly different when the negative group consisted only of CNS sites.

We then calculated the AUC for the logistic regression model based on each of the significant parameters separately, and finally for the combination of parameters that produced the best diagnostic performance. For each data set a combination of Coll and Hb provided the best diagnostic performance, and the addition of other parameters was negligible. For the individual parameters, as well as the combination providing the best diagnostic performance, the AUC increased as the percentage of CNS increased. Figure 4 compares AUCs of logistic regression models based on the

most significant parameters, A, Coll, and Hb, respectively, and varying amounts of CNS sites.

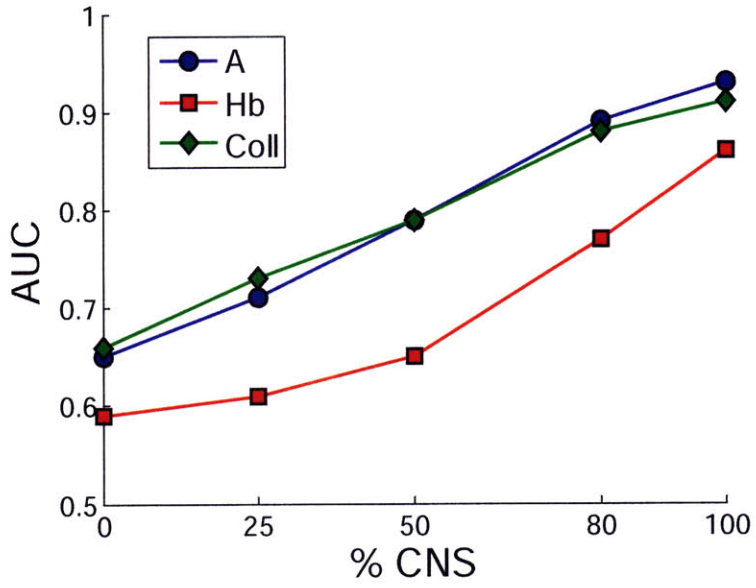

Figure 6.3.4. Area under the LCV ROC curve (AUC) for logistic regression models based on: 1) A parameter (blue line), 2) Coll (green line), and 3) Hb (red line), as a function of percentage of CNS sites included in the data set.

6.4 Discussion

6.4.1 Microscopic characterization of tissue type

Since all SILs begin at the squamo-columnar junction and the spatial extension and limits of SILs coincide with the distribution of the transformation zone[11], and colposcopy is successful in differentiating zones of the cervix, it is not surprising that the majority of clinically suspicious sites in this study were found in the transformation zone.

6.4.2 Spectral comparison of normal squamous and normal transformation zone sites

The results from the contact probe and imaging studies demonstrated that the transformation zone is spectroscopically distinct from the normal squamous sites. In both studies the transformation zone sites were histopathologically normal. However, the transformation zone sites from the contact probe study were clinically suspicious,

whereas those in the imaging study sites were clinically normal. No differences in the parameter trends were observed based on clinical impression. Both contact probe and imaging data demonstrated that NT sites exhibit lower values of Coll and A parameter and higher values of Hb compared to the CNS sites. These findings are consistent with the transformation zone comprising both ectocervical and endocervical features. Endocervix is typically represented by higher hemoglobin concentration, lower scattering, and lower collagen fluorescence relative to ectocervix. The spectroscopic variations can be explained by anatomy differences. Higher hemoglobin concentration is explained by the fact that the normal ectocervix is covered by non-keratinizing glycogen producing stratified squamous epithelium, while in the endocervix small capillary loops are located directly beneath the single layer of mucus secreting columnar cells, thus closer to the surface then in the case of the ectocervix. The lower scattering within the endocervix as compared to the ectocervix is likely related to the fact that the major source of tissue scattering is collagen fibers in the connective tissue, and the ectocervical stroma is composed of fibrous connective tissue, whereas the stroma of the endocervix is marked by abundant mucin-producing glands. The same anatomical feature may explain the lower collagen fluorescence in the endocervix compared to the ectocervix.

Thus, normal ectocervix (normal squamous epithelium) is anatomically and spectroscopically different from the transformation zone of the cervix, even in the absence of clinical and histological abnormality.

6.4.3 Spectral comparison of CNS, non-HSIL, and HSIL sites

CNS sites are spectroscopically distinct from both non-HSIL and HSIL sites. The same parameters that differentiate CNS sites from NT sites also differentiate CNS sites from all non-HSIL sites. This finding is not surprising, considering the fact that majority of non-HSIL sites are found in the transformation zone. Interestingly, the same parameters that differentiate CNS sites from NT sites also differentiate CNS sites form HSIL sites in our data set. All of the HSILs in our data set and the vast majority of HSILs in the general population are found in the transformation zone. These findings indicate that the spectral differences seen between normal squamous

and HSIL sites are largely due to anatomical differences between normal squamous epithelium and the transformation zone, and not to a disease state.

6.4.3 *Diagnostic performance for HSIL detection as a function of the percentage of CNS sites included in the test sample*

Many spectroscopic studies have included clinically normal squamous sites, with or without histopathology confirmation, in the data set used to evaluate the performance of the diagnostic algorithms to detect HSIL.[2,4,6,8,10] Our results show that the apparent performance of the diagnostic algorithm (HSIL vs. everything else) depends on the percentage of CNS sites included in the test. We find that as the percentage of CNS in the negative group decreases, the number of significant parameters differentiating HSIL from everything else decreases, as well. Diagnostic performance of logistic regression models based on the individual significant parameters, as well as on the combination that produced the highest diagnostic performance, also decreases. The parameters that we tested included those describing the scattering, absorption, and fluorescence properties of tissue. Based on our findings, including clinically normal squamous sites into the data set which is used to develop or evaluate the performance of the algorithm for detection of HSIL is a confounding artifact that artificially increases performance values with respect to the key differentiation to be made, namely distinguishing HSILs from clinically suspicious non-HSILs.

6.5 Conclusion

Normal transformation zone is anatomically, histologically, and as we have shown, spectroscopically different from the normal squamous epithelium. As the vast majority of the HSILs are found in the transformation zone, the spectral differences between normal squamous and HSIL sites are largely due to the confounding effects of anatomy. The inclusion of clinically normal squamous sites into a data set which is used to evaluate the diagnostic performance of the algorithm (HSILs vs. non-HSILs) produces unrealistically high performance values. In order to improve the accuracy of clinical HSIL detection, spectroscopy must be able to identify HSILs within the transformation zone. Chapter 7 discusses the development of a spectral

algorithm free of the confounding effects of anatomy and Chapter 8 extends these studies to the imaging mode.

6.6 References

1. R. D. Alvarez, T. C. Wright and O. D. Grp, "Effective cervical neoplasia detection with a novel optical detection system: A randomized trial," *Gynecologic Oncology* **104** (2), 281-289 (2007).
2. S. K. Chang, Y. N. Mirabal, E. N. Atkinson, D. Cox, A. Malpica, M. Follen and R. Richards-Kortum, "Combined reflectance and fluorescence spectroscopy for in vivo detection of cervical pre-cancer," *Journal of Biomedical Optics* **10** (2), - (2005).
3. I. Georgakoudi, E. E. Sheets, M. G. Muller, V. Backman, C. P. Crum, K. Badizadegan, R. R. Dasari and M. S. Feld, "Trimodal spectroscopy for the detection and characterization of cervical precancers in vivo," *American Journal of Obstetrics and Gynecology* **186** (3), 374-382 (2002).
4. W. K. Huh, R. M. Cestero, F. A. Garcia, M. A. Gold, R. S. Guido, K. McIntyre-Seltman, D. M. Harper, L. Burke, S. T. Sum, R. F. Flewelling and R. D. Alvarez, "Optical detection of high-grade cervical intraepithelial neoplasia in vivo: Results of a 604-patient study," *American Journal of Obstetrics and Gynecology* **190** (5), 1249-1257 (2004).
5. N. M. Marin, A. Milbourne, H. Rhodes, T. Ehlen, D. Miller, L. Benedet, R. Richards-Kortum and M. Follen, "Diffuse reflectance patterns in cervical spectroscopy," *Gynecologic Oncology* **99** (3), S116-S120 (2005).
6. Y. N. Mirabal, S. K. Chang, E. N. Atkinson, A. Malpica, M. Follen and R. Richards-Kortum, "Reflectance spectroscopy for in vivo detection of cervical precancer," *Journal of Biomedical Optics* **7** (4), 587-594 (2002).
7. J. R. Mourant, T. J. Bocklage, T. M. Powers, H. M. Greene, K. L. Bullock, L. R. Marr-Lyon, M. H. Dorin, A. G. Waxman, M. M. Zsemlye and H. O. Smith, "In vivo light scattering measurements for detection of precancerous conditions of the cervix," *Gynecologic Oncology* **105** (2), 439-445 (2007).
8. R. J. Nordstrom, L. Burke, J. M. Niloff and J. F. Myrtle, "Identification of cervical intraepithelial neoplasia (CIN) using UV-excited fluorescence and diffuse-reflectance tissue spectroscopy," *Lasers in Surgery and Medicine* **29** (2), 118-127 (2001).
9. I. M. Orfanoudaki, G. C. Themelis, S. K. Sifakis, D. H. Fragouli, J. G. Panayiotides, E. M. Vazgiouraki and E. E. Koumantakis, "A clinical study of optical biopsy of the uterine cervix using a multispectral imaging system," *Gynecologic Oncology* **96** (1), 119-131 (2005).
10. N. Ramanujam, M. F. Mitchell, A. Mahadevan, S. Thomsen, A. Malpica, T. Wright, N. Atkinson and R. RichardsKortum, "Development of a multivariate

statistical algorithm to analyze human cervical tissue fluorescence spectra acquired in vivo," *Lasers in Surgery and Medicine* **19** (1), 46-62 (1996).

11. A. Blaustein and R. J. Kurman, *Blaustein's pathology of the female genital tract*, Springer, New York (2002)

12. R. Kalluri and M. Zeisberg, "Fibroblasts in cancer," *Nature Reviews Cancer* **6** (5), 392-401 (2006).

13. H. Nagase and J. F. Woessner, "Matrix metalloproteinases," *Journal of Biological Chemistry* **274** (31), 21491-21494 (1999).

14. J. Mazibrada, M. Ritta, M. Mondini, M. De Andrea, B. Azzimonti, C. Borgogna, M. Ciotti, A. Orlando, N. Surico, L. Chiusa, S. Landolfo and M. Garigho, "Interaction between inflammation and angiogenesis during different stages of cervical carcinogenesis," *Gynecologic Oncology* **108** (1), 112-120 (2008).

15. C. K. Brookner, M. Follen, I. Boiko, J. Galvan, S. Thomsen, A. Malpica, S. Suzuki, R. Lotan and R. Richards-Kortum, "Autofluorescence patterns in short-term cultures of normal cervical tissue," *Photochemistry and Photobiology* **71** (6), 730-736 (2000).

16. J. A. Freeberg, D. M. Serachitopol, N. McKinnon, R. Price, E. N. Atkinson, D. D. Cox, C. MacAulay, R. Richards-Korturn and M. Follen, "Fluorescence and reflectance device variability throughout the progression of a phase II clinical trial to detect and screen for cervical neoplasia using a fiber optic probe," *Journal of Biomedical Optics* **12** (3), - (2007).

17. E. M. Gill, A. Malpica, R. Richards-Kortum, M. Follen and N. Ramanujam, "Collagen autofluorescence of the human cervix and menopausal status," *Lasers in Surgery and Medicine* 12-12 (2003).

18. V. Kumar, A. K. Abbas, N. Fausto, S. L. Robbins and R. S. Cotran, *Robbins and Cotran pathologic basis of disease*, Elsevier Saunders, Philadelphia (2005)

19. D. G. Ferris, *Modern colposcopy : textbook and atlas*, Kendall/Hunt, Dubuque, Iowa (2004)

CHAPTER 7

Contact probe studies: Development of diagnostic algorithm

In Chapter 6 we demonstrated that apparent performance of spectral diagnostic algorithms for identifying cervical dysplasia is artificially enhanced when clinically normal sites were included, as a result of normal anatomic differences. In this chapter we use contact probe data to develop a spectral algorithm for detection of high grade squamous intraepithelial lesions (HSILs) free of the confounding effects of cervical anatomy. We focus on the clinically relevant issue that spectroscopy must address, namely how well HSILs can be differentiated from non-HSILs among clinically suspicious sites, majority of which are found in transformation zone. Our result show that the spectroscopic contrast between non-HSIL and HSIL is enhanced if parameters are normalized by an internal standard, the corresponding parameter extracted from clinically normal squamous site of the same patient. The normalized A scattering parameter is the most diagnostic parameter and the addition of any other spectroscopy parameter does not contribute significantly to the diagnostic performance. A leave-one-out cross validated sensitivity, specificity, and area under the receiver-operator characteristic (ROC) curve of 89%, 79%, and 0.85, respectively, are achieved for this separation.

7.1 Introduction

The main target of the clinical management of women with suspected SIL is the accurate diagnosis of advanced precancerous changes, specifically high grade SILs (HSILs). As already explained in Chapter 2, the current clinical standard for cervical cancer diagnosis is colposcopy, a procedure that involves visual inspection and biopsy of at-risk tissue, followed by histopathology. The accuracy of colposcopy highly depends on the physician's expertise. The reported values of sensitivity and specificities of colposcopy vary widely in the literature.[1-3] In expert hands, colposcopy was reported to be quite sensitive (96 %) but not very specific (48 %) for detection of cervical dysplasia.[2] As an objective, real time diagnostic tool, spectroscopy has the potential to reduce the interobserver disagreement in colposcopy and the amount of unnecessary biopsies. The diagnostic effectiveness of reflectance and fluorescence spectroscopy, in both contact probe and imaging modes, has been tested in various stages of clinical studies, from pilot to phase III clinical studies.[4-13] The results show the potential of reflectance and fluorescence spectroscopy, individually or in combination, to improve the accuracy of disease detection. A comprehensive review of the clinical effectiveness of reflectance and fluorescence spectroscopy for the *in vivo* diagnosis of cervical dysplasia was given in a recent review article by Cardenas-Turanzas et al.[14]

HSILs have a relatively high risk of progression to invasive cancer and require treatment. Unlike HSILs, low grade SILs (LSILs) have high rates of spontaneous regression and do not require treatment.[15] Since the vast majority of HSILs is found within the transformation zone and normal ectocervix and endocervix are easily identified by colposcopic examination,[15] spectroscopy must be able to identify HSILs within the transformation zone in order to improve the accuracy of clinical HSIL detection. Furthermore, there is a distribution of risk of high grade disease even within the transformation zone. More severe disease is typically located close to the squamo-columnar junction where the epithelium is least mature, while most mature metaplastic epithelium has little neoplastic potential, like that of the original squamous epithelium.[16] In order to accurately diagnose HSILs, spectroscopy must be

able to reliably resolve the disease process in the context of the background microanatomic complexity inherent in the transformation zone.

A number of spectroscopic studies include clinically normal squamous sites, either non-biopsied or histopathologically confirmed, in the data set used to evaluate the performance of algorithms for diagnosing HSILs.[5,7,9,11,13] Several studies have shown that both normal anatomic variations and disease are important sources of spectroscopic contrast in tissue.[6,10,17] In Chapter 6, we demonstrated that the apparent performance of diagnostic algorithms for identifying HSILs is enhanced when clinically normal squamous sites are included, as a result of normal anatomic differences. Both diagnostic parameters and performance metrics depend heavily on how much clinically normal squamous sites are included in the test group. Based on the findings presented in Chapter 6, including clinically normal squamous sites into the data set which is used to evaluate the performance of the algorithm for detection of HSILs is a confounding artifact that artificially increases performance values with respect to the key differentiation to be made, namely distinguishing HSILs from clinically suspicious non-HSILs.

In this Chapter we use contact probe data to develop an algorithm for detection of HSILs free of the confounding effect of cervical anatomy. We asses the potential clinical impact of our technique by evaluating its success in differentiating HSIL from non-HSIL sites among clinically suspicious sites, which are predominantly found in the transformation zone. We also investigate the effect of normal anatomical variation within the transformation zone, the stromal glandularity content, on the extracted spectroscopy parameters. Chapter 8 extends these studies to the imaging mode using a Quantitative Spectroscopy Imaging (QSI).

7.2 Methods

We study patients undergoing colposcopic examination using reflectance and fluorescence in the contact probe mode. Information about the FastEEM instrument used in the contact probe study is given in Chapter 4. The details of the clinical study design and data modeling are given in Chapter 5. Our study has two aims: 1) to develop an algorithm based on spectroscopic parameters to differentiate HSIL from

non-HSIL within clinically suspicious sites; and 2) to examine the effect of normal anatomic variation within the transformation zone, the stromal glandular content, on the spectroscopic parameters.

To identify changes in spectroscopic parameters due to disease we studied the values of extracted spectroscopy parameters from clinically suspicious sites. The spectroscopy parameters extracted from each clinically suspicious site were normalized to the values of the corresponding spectroscopy parameters extracted from a CNS site collected from the same patient to correct for patient-to-patient variations. Normalized tissue parameters were correlated with histopathology. We determined the significant parameters and developed a diagnostic algorithm using logistic regression model and the combination of parameters that provided the best diagnostic performance.

Tissue parameters were correlated to histopathology diagnosis for all data collected from clinically suspicious sites from the probe data set. A two-sided Wilcoxon Rank Sum test was used to test the hypothesis that the extracted normalized spectroscopic parameter distributions of HSIL and non-HSIL were different. A p-value of < 0.05 was considered significant. The spectral algorithms were developed by using logistic regression models based on a combination of significant normalized spectroscopic parameters providing the most important diagnostic information. Leave-one-out cross-validation (LCV) was used to construct receiver-operator characteristic (ROC) curves for the spectral algorithms. The discrimination ability was evaluated by the area under the ROC curve (AUC), as well as the sensitivity and specificity.

To study the effect of stromal glandularity on spectroscopy parameters, we divided biopsied non-HSIL sites into two groups: 1) non-HSIL sites with a minimal amount (<25%) of stromal glands (non-SG sites), and 2) non-HSIL sites with highly glandular stroma (≥25%) (SG sites), and compared them to HSIL sites by using the statistical methods described above.

7.3 Results

7.3.1 Data Set

As already shown in Table 6.3.1. of Chapter 6, our contact probe data set consisted of 33 CNS sites, which were not biopsied, and 51 clinically suspicious biopsied sites, out of which histopathology determined that 30 sites were negative for SIL, 12 sites were LSILs, and 9 sites were HSILs. For the purposes of developing a diagnostic algorithm which aims to detect HSIL sites, the negative for SIL sites and the LSIL sites were combined-- we refer to these in the following as non-HSIL sites. We note that these non-HSIL sites do not include the 33 CNS sites.

7.3.2 Microscopic characterization of site location, stromal glandularity, and epithelial thickness

No information about stromal glandularity or epithelial thickness was available for the CNS sites, as they were not biopsied. This information was available for clinically suspicious biopsied sites only.

Site location Histopathology evaluation confirmed that 36 of all biopsied study sites were from the transformation zone. The histopathology features consistent with transformation zone were not found for only 6 sites. For 9 biopsied sites stroma was not visible on the histology slides, and it was impossible to confirm that the samples were in the transformation zone or to determine the stromal glandularity by histopathology. All of the HSIL sites but one for which stroma was not visible on the histology slide came from the transformation zone.

Table 7.3.1. Description of glandular content for non-HSIL and HSIL sites.

Group	Glandular content		
	≥25%	<25 %	Could not be evaluated
non-HSIL	13 (31%)	21 (50%)	8 (19%)
HSIL	5 (56%)	3 (33%)	1 (11%)

Stromal glandularity Table 7.3.1. provides a description of stromal glandularity for non-HSIL and HSIL groups. Unlike the non-HSIL sites, the majority of HSIL sites had glandular stroma (≥25% stroma occupied by glands).

Epithelial thickness Table 7.3.2. provides an average epithelial thickness values for HSIL and non-HSIL sites. According to Wilcoxon Rank Sum test there was no significant difference in epithelial thickness values between HSIL and non-HSIL sites.

Table 7.3.2. Epithelial thickness values for HSIL and non-HSIL sites.

Epithelial thickness	**Group**	
	HSIL	**non-HSIL**
Average (μm)	171	250
Standard Deviation (μm)	50	124

7.3.3 Identifying HSILs among the clinically suspicious sites

To assess the potential clinical impact of our technique, it is essential to evaluate its success in differentiating HSIL from non-HSIL sites among clinically suspicious sites. Clinically suspicious sites are typically found in the transformation zone of the cervix. We developed a diagnostic algorithm to determine whether a clinically suspicious lesion was an HSIL or non-HSIL site. We found that normalization of the spectroscopy parameters enhanced the contrast between HSIL and non-HSIL sites.

In Chapter 6 we investigated the differences in spectroscopy between HSIL and non-HSIL sties before parameter normalization. As already shown in Figure 6.3.1. of previous chapter, before parameter normalization non-HSIL sites can be differentiated from HSILs by their lower values of A and Coll parameters, and higher values of Hb. When logistic regression and LCV were performed, HSIL sites could be differentiated from non-HSIL based on Coll and Hb with an AUC, sensitivity, and

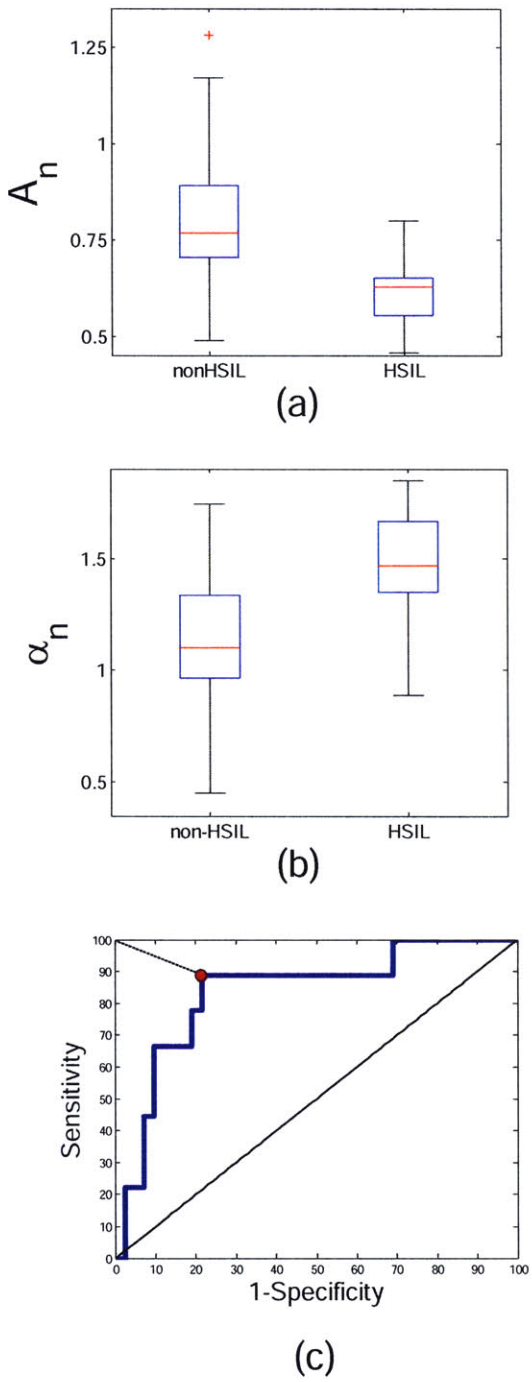

Figure 7.3.1. Discrimination of HSIL from non-HSIL among clinically suspicious sites. Boxplots of normalized (a) A_n parameter, and (b) α_n; (c) LCV ROC curve for the diagnostic algorithm (A_n parameter only)

specificity of only 0.68, 78% and 67%, respectively. However, after normalization, an AUC, sensitivity and specificity of 0.84, 89% and 79%, respectively, were achieved. HSIL sites are characterized by a significantly lower values of the A_n parameter and significantly higher values of α_n, Hb_n, and bvr_n compared to non-HSIL sites. Unlike Coll, $Coll_n$ did not exhibit significant difference between two groups. The positive and negative predictive values were 48% and 97%, respectively. The normalized A parameter was the most diagnostic, and the addition of any other spectroscopy parameter did not contribute significantly to diagnostic performance. The corresponding ROC plot is shown in Figure 7.3.1(c), and the two most significant parameters, A_n and α_n, are shown in Figure 7.3.1. (a) and (b), respectively.

7.3.4 Effect of stromal glandularity on spectroscopic parameters

Because the glandular content varies within the transformation zone, we also investigated the effect of stromal glandularity on the spectroscopy parameters. Since the majority of the HSIL sites in our data set have significantly glandular stroma, while the majority of non-HSIL sites are minimally glandular, we divided biopsied non-HSIL sites into two groups: 1) non-HSIL sites with a highly glandular stroma (≥25%) (SG sites), and 2) non-HSIL sites with a minimal amount (<25 %) of stromal

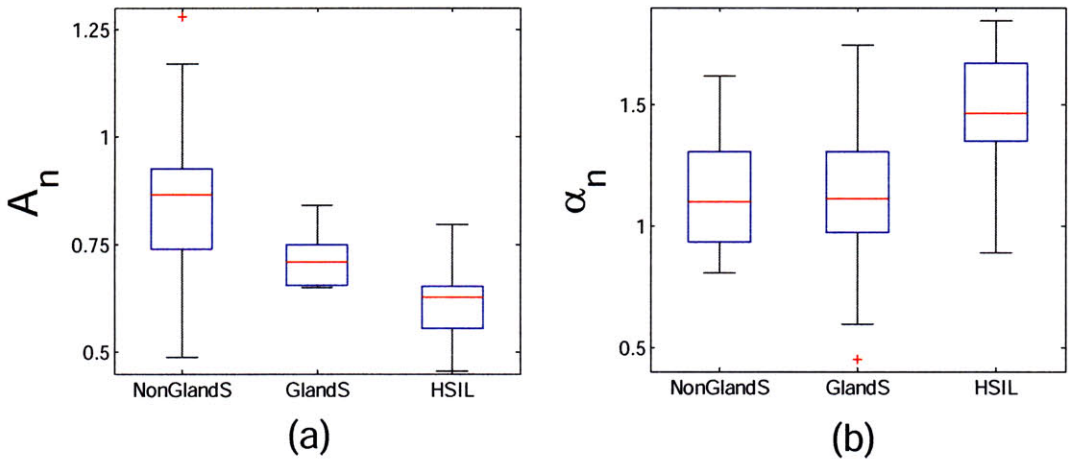

Figure 7.3.2. Discrimination of HSIL from SG and non-SG sites. Box plots of (a) A_n parameter and (b) α_n.

glands (non-SG sites), and compared them to HSIL sites. While HSIL can be differentiated from non-SG sites on the basis of lower values of A_n and Coll and higher values of Hb_n, α_n and bvr_n, only two parameters, A_n and α_n, were significantly different between HSIL sites and SG sites by using the Wilcoxon Rank Sum test. Figure 7.3.2. shows box plots of the A_n and α_n parameters which were significantly different between HSIL and both SG and non-SG sites.

We developed logistic regression models to differentiate HSIL from non-SG and SG sites. In both cases, A_n alone provided the best diagnostic ability and the addition of other parameters was negligible. We also developed a logistic regression model to differentiate Non-SG sites from SG sites. When LCV were performed, SG could be differentiated from Non-SG with AUC, sensitivity and specificity of 0.71, 69%, and 79% respectively, based on Coll and Hb_n. Table 7.3. provides a summary of the diagnostic parameters used and the performance of the logistic regression model for different groups tested in this chapter and in the previous chapter. The comparisons are grouped according to whether there is a difference in anatomy, disease state, or both.

Table 7.3.3. Parameters used in the diagnostic models, and performance of the models for the different groups tested.

Anatomy or Disease Difference	**Test Groups**	**Diagnostic parameters used**	**Logistic regression AUC/Sens(%)/Spec(%)**
Anatomy	CNS vs. NT* (probe)	Coll, Hb	0.89/89/85
	SG vs. Non-SG	Coll, Hb_n	0.71/69/79
Anatomy + Disease	HSIL vs. non-HSIL	A_n	0.84/89/79
Disease	HSIL vs. SG	A_n	0.82/89/70

*NT- histopathologically confirmed to be normal transformation zone sites. This result was obtained in the companion paper.

7.4 Discussion

7.4.1 Microscopic characterization of site location, stromal glandularity, and epithelial thickness

Since all SILs begin at the squamo-columnar junction and the spatial extension and limits of SILs coincide with the distribution of the transformation zone[16], and colposcopy is successful in differentiating zones of the cervix, it is not surprising that the majority of clinically suspicious sites in this study were found in the transformation zone. Furthermore, unlike the non-HSIL sites, the majority of HSIL sites in our study had glandular stroma (≥25% stroma occupied by glands). This finding is consistent with the fact that there is a distribution of risk of HSIL within the transformation zone. HSIL disease is typically located close to the squamo-columnar junction, where the epithelium is least mature and the stroma is more glandular, whereas most mature metaplastic epithelium has little neoplastic potential. [16] There was no significant difference in epithelial thickness values between HSIL and non-HSIL sites.

7.4.2 Identifying HSILs among the clinically suspicious sites

The clinically relevant issue that spectroscopy must address is how well HSILs can be differentiated from non-HSILs among clinically suspicious sites, i.e. sites that are subjectively assessed by clinician as colposcopically abnormal. Predictably, clinically suspicious sites are typically found in the transformation zone of the cervix. In making this distinction, we found that normalizing the spectroscopy parameters of the clinically suspicious biopsied sites by the value of the corresponding spectroscopy parameters of the clinically normal squamous site collected from the same patient enhanced the spectroscopic contrast between HSIL and non-HSIL sites. This finding is not surprising, given the fact that during colposcopy, clinically suspicious sites are identified based on their contrast in color, texture, and other features relative to normal tissue. Normalization may reduce sources of intrinsic patient-to-patient spectroscopic variations, such as age and menopausal status. Furthermore, normalization may account for differences caused by the time-dependent effect of the applied acetic acid on tissue scattering and

absorption. The vasoconstrictive and light scattering effects of the acetic acid[15,18] may affect the hemoglobin concentration, effective blood vessel radius, and also the scattering parameters. Finally, as will be seen in Chapter 8, a Quantitative Spectroscopy Imaging system study of cervical dysplasia *in vivo* also found that parameter normalization is crucial for distinguishing HSILs from non-HSILs within the transformation zone of the cervix.

A number of features characterize precancerous SILs that are at higher likelihood of progressing to invasive cancer, such as loss of differentiation of the epithelial cells,[16] degradation and reorganization of stromal collagen by matrix metalloproteinase activity,[19,20] as well as increased microvascular density and angiogenesis[21]. Increased epithelial fluorescence, attributed to mitochondrial NADH, as well as decreased collagen fluorescence, attributed to collagen matrix degradation by matrix metalloproteinases, has been observed for dysplastic compared to normal cervical fresh tissue using fluorescence confocal microscopy.[22] It is expected therefore, that HSIL sites will express spectroscopic features such as lower reduced scattering coefficient, lower contribution of collagen fluorescence, higher contribution of NADH fluorescence, and higher hemoglobin concentration.

We find that several spectroscopy parameters, A, α, Hb, bvr, and Coll, after normalization for patient-to-patient variation, are statistically significant for differentiating HSILs from non-HSILs among clinically suspicious sites, majority of which are found in the transformation zone.

In our study HSIL sites exhibit significantly lower values of A_n parameter relative to the non-HSIL sites. This observation is consistent with the study of Arifler et al.[23], who used Monte Carlo modeling of cervical tissue to show that the smaller stromal reduced scattering coefficient is the major cause for decreased reflectance intensity of HSIL compared to normal squamous tissue. Georgakoudi et al.[6] also report lower reduced scattering coefficient for SILs vs. biopsied non-SILs. Furthermore, in a study of 161 patients, Mirabal et al.[9] found that there is a gradual decrease in mean reflectance intensity as the severity of dysplasia increases. It is unknown, however, if higher hemoglobin concentration, lower scattering, or a

combination of both is responsible for such a trend. Finally, the companion study conducted with the Quantitative Spectroscopy Imaging system also observed lower values of A_n parameter for HSIL compared to non-HSIL sites within transformation zone.[24]

We also observe higher hemoglobin concentration of HSIL sites relative to the non-HSIL sites. Higher hemoglobin concentration in HSIL sites compared to other tissue types has been noted by Chang et al.[25] Additionally, Marin et al.[8] report that hemoglobin features of the reflectance tissue spectra are more prominent in abnormal tissue compared to normal squamous tissue. However, studies that considered diagnosing HSIL within clinically suspicious sites, such as Georgakoudi et al.[6], as well as Mourant et al.[10] reported no significant change in the hemoglobin concentration between HSIL and non-HSILs.

Our finding of higher hemoglobin oxygenation for HSIL sites compared to non-HSIL within the clinically suspicious sites is consistent with the results of a study by Mourant et al.[10] which also looked at the difference between HSIL and clinically suspicious non-HSIL sites, 90% of which were found in the transformation zone. The source of higher hemoglobin oxygenation for HSIL sites is not well understood and needs further investigation.

We find that the effective blood vessel radius is increased for HSIL sites compared to non-HSIL sites. This may be due to the presence of dilated atypical blood vessels associated with precancerous and cancerous changes[15].

Finally, we observe decreased Coll for HSIL sites compared to non-HSIL sites. This observation is consistent with decreased collagen fluorescence due to degradation of collagen matrix, increased NADH fluorescence due to changes in cellular metabolism, or a combination of both. The increase in epithelial thickness is not a source of this feature, since there was no significant difference in measured epithelial thickness between HSIL and non-HSIL sites in our study. Increased NADH contribution of SILs compared to non-SILs within the transformation zone has been observed by Georgakoudi et al.[6] Chang et. al[25] report a decreased stromal collagen contribution; however, their study included clinically normal squamous

sites. Studies by Nordstrom[11], and Huh[7], which utilize 340 nm fluorescence, reported no significant differences between HSIL and normal sites in the transformation zone (squamous metaplasia). A study of Ramanujam et al. reported that 340 nm excitation HSIL sites could not be differentiated from non-HSIL sites in the transformation zone (cervical intraepithelial neoplasia 2/3 (equivalent to HSIL) vs. squamous metaplasia).

If the microscopic architecture of suspicious sites is not taken into account, the spectroscopic differences between HSIL and non-HSIL sites may be attributed solely to disease state. When we considered the glandular composition of these suspicious sites, most of which were within the transformation zone, we found that HSIL sites have relatively higher content of glandular stroma compared to non-HSIL sites. The HSILs are more likely to occur in the area close to the squamo-columnar junction. Therefore, HSIL sites are more likely to have a significantly glandular stroma. The only two parameters that differentiate the HSIL group and a SG group (non-HSIL sites with >25% stroma occupied by glands), are A_n and α_n. This is a challenging distinction to make, since the major difference between these two sites is the disease state. Furthermore, we show that SG sites can be differentiated from Non-SG sites with AUC, sensitivity and specificity of 0.71, 69%, and 79%, respectively, based on Coll and Hb_n , as seen in Table 7.3.3.. Our results suggest that Hb_n, bvr_n, and Coll are highly dominated by anatomy, whereas a low values of A_n parameter and high values of α_n are the true signatures of disease.

Finally we developed a spectral diagnostic model to distinguish HSIL sites vs. non-HSIL sites. It demonstrated an AUC, sensitivity and specificity of 0.84, 89% and 79%, respectively. Positive and negative predictive values were 48% and 97% respectively. The high negative predictive value suggests that this technique may be useful for guiding biopsy. The A_n parameter was the most diagnostic, and the addition of other spectroscopy parameters did not contribute significantly to diagnostic performance.

7.5 Conclusions

In Chapter 6 we have demonstrated that the inclusion of clinically normal squamous sites into a data set which is used to develop and evaluate the diagnostic

performance of the algorithm (HSILs vs. non-HSILs) produces unrealistically high performance values and changes the optimal diagnostic parameters. The clinically relevant issue that spectroscopy must address is how well HSILs can be differentiated from non-HSILs among clinically suspicious sites, the vast majority of which are found in the transformation zone of the cervix. In making this distinction, we found that the spectroscopic contrast between non-HSIL and HSIL is enhanced if parameters are normalized by an internal standard, the corresponding parameter extracted from clinically normal squamous site of the same patient. The A_n parameter is the most diagnostic parameter and the addition of any other spectroscopy parameter does not contribute significantly to the diagnostic performance. The AUC, sensitivity, and specificity for leave-one-out cross-validation and logistic regression model are 0.85, 89%, and 79% respectively. Positive and negative predictive values are 48% and 97% respectively. The HSIL sites, most of which are characterized by substantial amount of glandular stroma ($\geq$ 25 %), can be accurately distinguished from a group of non-HSIL sites exhibiting a substantial amount of glandular stroma by only two parameters, A_n and α_n. We conclude that Hb_n, bvr_n, and Coll are strongly dominated by anatomy, while a low A_n parameter and high α_n are true signatures of disease. In the next Chapter, we will extend these studies to an imaging modality and show the results which are consistent with the results of the contact probe study presented here.

7.6 References

1. D. Solomon, M. Schiffman, R. Tarone, E. E. Partridge, L. Kilgore, S. Hester, J. L. Walker, G. A. Johnson, A. Yadack, R. S. Guido, K. McIntyre-Seltman, R. P. Edwards, J. Gruss, N. B. Kiviat, L. Koutsky, C. Mao, J. M. Haug, D. Ferris, J. T. Cox, L. Burke, C. M. Wheeler, C. Peyton-Goodall, M. M. Manos, R. J. Kurman, D. L. Rosenthal, M. E. Sherman, M. H. Stoler, D. M. Harper, J. Rosenthal, M. Dunn, J. Quarantillo, D. Robinson, A. T. Lorincz, L. Rich and A. Grp, "A randomized trial on the management of low-grade squamous intraepithelial lesion cytology interpretations," *American Journal of Obstetrics and Gynecology* **188** (6), 1393-1400 (2003).
2. M. F. Mitchell, D. Schottenfeld, G. Tortolero-Luna, S. B. Cantor and R. Richards-Kortum, "Colposcopy for the diagnosis of squamous intraepithelial lesions: A meta-analysis," *Obstetrics and Gynecology* **91** (4), 626-631 (1998).
3. S. B. Cantor, M. Cardenas-Turanzas, D. D. Cox, E. N. Atkinson, G. M. Nogueras-Gonzalez, J. R. Beck, M. Follen and J. L. Benedet, "Accuracy of colposcopy in the diagnostic setting compared with the screening setting," *Obstetrics and Gynecology* **111** (1), 7-14 (2008).

4. R. D. Alvarez, T. C. Wright and O. D. Grp, "Effective cervical neoplasia detection with a novel optical detection system: A randomized trial," *Gynecologic Oncology* **104** (2), 281-289 (2007).
5. S. K. Chang, Y. N. Mirabal, E. N. Atkinson, D. Cox, A. Malpica, M. Follen and R. Richards-Kortum, "Combined reflectance and fluorescence spectroscopy for in vivo detection of cervical pre-cancer," *Journal of Biomedical Optics* **10** (2), - (2005).
6. I. Georgakoudi, E. E. Sheets, M. G. Muller, V. Backman, C. P. Crum, K. Badizadegan, R. R. Dasari and M. S. Feld, "Trimodal spectroscopy for the detection and characterization of cervical precancers in vivo," *American Journal of Obstetrics and Gynecology* **186** (3), 374-382 (2002).
7. W. K. Huh, R. M. Cestero, F. A. Garcia, M. A. Gold, R. S. Guido, K. McIntyre-Seltman, D. M. Harper, L. Burke, S. T. Sum, R. F. Flewelling and R. D. Alvarez, "Optical detection of high-grade cervical intraepithelial neoplasia in vivo: Results of a 604-patient study," *American Journal of Obstetrics and Gynecology* **190** (5), 1249-1257 (2004).
8. N. M. Marin, A. Milbourne, H. Rhodes, T. Ehlen, D. Miller, L. Benedet, R. Richards-Kortum and M. Follen, "Diffuse reflectance patterns in cervical spectroscopy," *Gynecologic Oncology* **99** (3), S116-S120 (2005).
9. Y. N. Mirabal, S. K. Chang, E. N. Atkinson, A. Malpica, M. Follen and R. Richards-Kortum, "Reflectance spectroscopy for in vivo detection of cervical precancer," *Journal of Biomedical Optics* **7** (4), 587-594 (2002).
10. J. R. Mourant, T. J. Bocklage, T. M. Powers, H. M. Greene, K. L. Bullock, L. R. Marr-Lyon, M. H. Dorin, A. G. Waxman, M. M. Zsemlye and H. O. Smith, "In vivo light scattering measurements for detection of precancerous conditions of the cervix," *Gynecologic Oncology* **105** (2), 439-445 (2007).
11. R. J. Nordstrom, L. Burke, J. M. Niloff and J. F. Myrtle, "Identification of cervical intraepithelial neoplasia (CIN) using UV-excited fluorescence and diffuse-reflectance tissue spectroscopy," *Lasers in Surgery and Medicine* **29** (2), 118-127 (2001).
12. I. M. Orfanoudaki, G. C. Themelis, S. K. Sifakis, D. H. Fragouli, J. G. Panayiotides, E. M. Vazgiouraki and E. E. Koumantakis, "A clinical study of optical biopsy of the uterine cervix using a multispectral imaging system," *Gynecologic Oncology* **96** (1), 119-131 (2005).
13. N. Ramanujam, M. F. Mitchell, A. Mahadevan, S. Thomsen, A. Malpica, T. Wright, N. Atkinson and R. RichardsKortum, "Development of a multivariate statistical algorithm to analyze human cervical tissue fluorescence spectra acquired in vivo," *Lasers in Surgery and Medicine* **19** (1), 46-62 (1996).
14. M. Cardenas-Turanzas, J. A. Freeberg, J. L. Benedet, E. N. Atkinson, D. D. Cox, R. Richards-Kortum, C. MacAulay, M. Follen and S. B. Cantor, "The clinical effectiveness of optical spectroscopy for the in vivo diagnosis of cervical intraepithelial neoplasia: Where are we?," *Gynecologic Oncology* **107** (1), S138-S146 (2007).
15. D. G. Ferris, *Modern colposcopy : textbook and atlas*, Kendall/Hunt, Dubuque, Iowa (2004)

16. A. Blaustein and R. J. Kurman, *Blaustein's pathology of the female genital tract*, Springer, New York (2002)
17. J. A. Freeberg, D. M. Serachitopol, N. McKinnon, R. Price, E. N. Atkinson, D. D. Cox, C. MacAulay, R. Richards-Korturn and M. Follen, "Fluorescence and reflectance device variability throughout the progression of a phase II clinical trial to detect and screen for cervical neoplasia using a fiber optic probe," *Journal of Biomedical Optics* **12** (3), - (2007).
18. W. Choi, C. C. Yu, C. Fang-Yen, K. Badizadegan, R. R. Dasari and M. S. Feld, "Feild-based angle-resolved light-scatteiring study of single live cells," *Optics Letters* **33** (14), 1596-1598 (2008).
19. R. Kalluri and M. Zeisberg, "Fibroblasts in cancer," *Nature Reviews Cancer* **6** (5), 392-401 (2006).
20. H. Nagase and J. F. Woessner, "Matrix metalloproteinases," *Journal of Biological Chemistry* **274** (31), 21491-21494 (1999).
21. J. Mazibrada, M. Ritta, M. Mondini, M. De Andrea, B. Azzimonti, C. Borgogna, M. Ciotti, A. Orlando, N. Surico, L. Chiusa, S. Landolfo and M. Garigho, "Interaction between inflammation and angiogenesis during different stages of cervical carcinogenesis," *Gynecologic Oncology* **108** (1), 112-120 (2008).
22. I. Pavlova, K. Sokolov, R. Drezek, A. Malpica, M. Follen and R. Richards-Kortum, "Microanatomical and biochemical origins of normal and precancerous cervical autofluorescence using laser-scanning fluorescence confocal microscopy," *Photochemistry and Photobiology* **77** (5), 550-555 (2003).
23. D. Arifler, C. MacAulay, M. Follen and R. Richards-Kortum, "Spatially resolved reflectance spectroscopy for diagnosis of cervical precancer: Monte Carlo modeling and comparison to clinical measurements," *Journal of Biomedical Optics* **11** (6), - (2006).
24. C. Lau, J. Mirkovic, C.-C. Yu, O. D. G., L. Galindo, R. Dasari, A. de las Morenas, V. Feng, K. Badizadegan, E. Stier and M. S. Feld, "Early Cancer Detection using Quantitative Spectroscopy Imaging: A Pilot Study in the Cervix," *Journal of Biomedical Optics*
25. S. K. Chang, N. Marin, M. Follen and R. Richards-Kortum, "Model-based analysis of clinical fluorescence spectroscopy for in vivo detection of cervical intraepithelial dysplasia," *Journal of Biomedical Optics* **11** (2), - (2006).

CHAPTER 8

Quantitative Spectroscopic Imaging: A pilot study in the cervix

In this Chapter we describe a pilot study in which we extend quantitative spectroscopy from contact-probe to wide-area QSI for detection of HSILs in the transformation zone. We present the disease related structural and biochemical changes observed by QSI. Using the observed spectroscopy changes, we construct diagnostic maps showing the locations of HSILs on patients evaluated prospectively with QSI. To construct the spectroscopy diagnostic maps, we normalize the quantitative spectroscopy measurements to reduce the effects of patient-to-patient variation just as in the case of the contact-probe studies. These maps are compared to corresponding disease maps obtained with histopathology to demonstrate the accuracy of QSI for detecting HSILs in the cervix. The results show that sites identified as HSIL by QSI are in good agreement with pathology. Furthermore, the HSIL identification criteria are the same for contact-probe and wide-area imaging implementations, indicating that quantitative spectroscopy's diagnosis is independent of instrument implementation.

8.1 Motivation

The contact-probe instrument, FastEEM, and the analysis models developed in our laboratory (see Chapter 5) provide detailed quantitative biochemical and morphological information, but only from several 1 mm^2 areas, thus lacking the adequate tissue sampling. In order to screen the entire area at risk of developing cervical cancer, we have developed a Quantitative Spectroscopy Imaging (QSI) Instrument. The QSI instrument is an extension of the contact-probe device with wide-area surveillance capabilities. As discussed in Chapter 4, we employed the principle of the "virtual probe" to provide wide area coverage while retaining the ability to extract detailed quantitative information about tissue biochemistry and morphology. The tip of the optical fiber is imaged to a tissue spot with a similar geometry to the contact-probe, and then raster scanned across the entire organ to provide wide-area surveillance. The virtual probe provides several advantages over full-field illumination. Since the delivery-collection geometry is small, we are able to extract optical properties such as reduced scattering coefficient and absorption coefficient independently. Furthermore, we are able to directly apply the knowledge acquired in the contact-probe studies to imaging studies.

Previous efforts have been made to apply spectroscopy in an imaging mode, particularly in the cervix[1-5], to enable wide-area diagnosis as is done in colposcopy. Milbourne *et al.* and Park *et al.* conducted three color reflectance and fluorescence spectroscopic imaging and observed that dysplastic cervical tissue emits at different wavelengths than normal cervical tissue when excited with ultraviolet or blue excitation light. A study by *Alvarez et al.* describes results of a large multicenter two-arm randomized trial comparing the effectiveness of colposcopy alone with colposcopy and a optical detection system (ODS), a method based on white light tissue reflectance, fluorescence and cervical video imaging.[2] The result of the study shows that the use of ODS in conjunction with colposcopy increased the true positive rate for detection of CIN2,3 in women with ASC and LSIL referral cytology by 26.5% and is claimed to be clinically significant. The use of ODS did not improve detection of CIN2,3 in women with HSIL cytology on referral.

Quantitative spectroscopic imaging, developed in our laboratory, differs from the spectroscopy imaging techniques reviewed above in that QSI measures tissue properties by using physical models of light propagation to extract information about tissue scatterers, absorbers, and fluorphores from the measured spectra. Understanding these changes allows knowledge obtained from QSI studies done with one instrumentation implementation to be transferred to another implementation and facilitates extending QSI to detect early cancer in other body organs.

In this Chapter we describe a pilot study to apply the findings of our contact-probe study and to extend quantitative spectroscopy from contact-probe to wide-area QSI for detection of HSIL in the cervix. In Chapter 6 we demonstrated that normal anatomical variations in the cervix must be accounted for prior to developing and evaluating a spectroscopic diagnostic algorithm for HSIL detection. Almost all HSILs are found in the transformation zone and gynecologists primarily aim to distinguish HSIL from non-HSIL within the transformation zone. As a result, this pilot study evaluates QSI's ability to distinguish HSIL from non-HSIL tissue in the transformation zone, as was done in the contact probe study explained in Chapter 7. We present the disease related structural and biochemical changes observed by QSI. Using the observed spectroscopy changes, we construct diagnostic maps showing the locations of HSIL on patients evaluated prospectively with QSI. These maps are compared to corresponding disease maps obtained with histopathology to demonstrate the accuracy of QSI for detecting HSIL in the cervix.

8.2 Methods

The QSI system was used to examine 19 patients referred for either colposcopy or LEEP at the Boston Medical Center due to a prior abnormal Pap smear or biopsy result, respectively. The details of QSI and the instrumentation implementation are described in Chapter 4. The details of clinical study design, as well as data modeling, were described in Chapter 5. Since the QSI instrument is a novel technique, our research team required 8 patients to learn the equipment and repair problems. Findings from the remaining 11 patients, 8 LEEPs and 3 colposcopies, are presented in this Chapter.

8.2.1. Overview of the diagnostic algorithm

To obtain a diagnostic map from measured quantitative spectroscopy parameter maps, four steps are required:

1) Identification of the endocervix- Spectroscopy parameters and edge detection are used to identify the location of the endocervix. The subsequent search for HSIL is not conducted in the endocervix.

2) Identification of the ectocervix- Spectroscopy parameters are used to identify a region of normal ectocervix tissue for normalizing the effects of patient-to-patient variation. This region serves as an on-site standard.

3) Parameter normalization- Spectroscopy parameters measured from the standard are used to normalize corresponding spectroscopy parameters measured from all other non-endocervix sites on the patient. Steps two and three are equivalent to the normalization procedure used in the contact probe study.

4) Identification of HSIL within the transformation zone- Normalized spectroscopy parameters are used to distinguish HSIL from non-HSIL tissue in the transformation zone.

8.2.1.i. Identification of the endocervix

Step 1 identifies the endocervix and separates it from the ectocervix and the transformation zone. As already discussed, the transformation zone is the site of the vast majority of HSILs[6], while the endocervix has no occurrence of HSIL. Endocervix is easily recognizable by visual inspection. Its intense red color is due to the superficial blood vessels located directly beneath the single layer of columnar epithelial cells. To identify the endocervix with QSI, we develop spectroscopic criteria using the measured parameters for segmenting endocervix from other tissues. We search for regions on the cervix with reduced A and elevated Hb relative to neighboring tissue. The scattering coefficient, which is represented by the A parameter, is lower in endocervix than in transformation zone and ectocervix due to the absence of highly scattering collagen-based connective tissue. The endocervix has

higher hemoglobin concentration due to the presence of superficial blood vessels. A and Hb values from the endocervix and transformation zone are inputted into Bayes' rule to compute the posterior probability (PP) of endocervix. For each patient we obtain a PP map of endocervix. Pixels with PP higher than a threshold are classified as likely to be endocervix. Once spectroscopy has selected regions likely to be endocervix, a Canny edge detection algorithm[7] is applied to the blue light picture from the color CCD to identify sharp changes in intensity on the cervix. Since hemoglobin in endocervical tissue absorbs blue light, the endocervix appears much darker than the transformation zone in a blue light picture and edge detection can identify its boundaries. Regions of tissue where both spectroscopy and edge detection identifies endocervix are classified as endocervix.

8.2.1.ii. Identification of the ectocervix

Step 2 identifies a region of normal ectocervix which is used for normalizing the effects of patient-to-patient variation on spectroscopy parameters, as was done in the contact probe study. Unlike the contact-probe study where a suitable ectocervix site was identified by the clinician, QSI has to automatically identify suitable sites from amongst its 441 pixels. To identify a suitable standard, we search for regions of each cervix with increased A and Coll relative to the surrounding tissue. Squamous epithelium is characterized by connective tissue comprised mainly of collagen, so it exhibits higher scattering, quantified by A, and collagen fluorescence, quantified by Coll, as already discussed in the contact probe studies. Once squamous tissue on the cervix is identified, we identify spatially contiguous areas larger than one pixel with homogeneous A and Coll measurements and choose these areas as the standard. Requiring homogeneity reduces the likelihood of selecting ectocervix sites where measurement quality was poor. Measurement quality can be adversely affected by specular reflection, blood, and foreign objects such as intrauterine devices and the speculum. After identifying the area to be the standard, we compute the average values of each spectroscopy parameter in the area.

8.2.1.iii. Parameter normalization

Step 3 uses the standard identified in Step 2 to normalize spectroscopy parameters measured from the transformation zone to reduce the effects of interpatient variation, as was done in the contact-probe study. Normalization for a patient involves dividing each spectroscopy parameter measured from each pixel in the transformation zone by its corresponding average value in the standard to obtain the normalized spectroscopy parameter for that pixel. Normalization highlights intrapatient variation in the transformation zone without confounding effects from interpatient variation, enhancing the contrast between HSIL and non-HSIL tissue.

8.2.1.iv. Identification of HSIL within the transformation zone

Step 4 uses normalized spectroscopy parameters to identify HSIL regions, as was done in the contact probe study. Normalized spectroscopy parameters measured from each tissue pixel outside of the endocervix and the standard are inputted into Bayes' Rule (similar to the procedure in Step 1) to compute the posterior probability of HSIL for that pixel. This results in a PP map of HSIL for each patient. Pixels with PP greater than the threshold can be classified as HSIL to yield a diagnostic map.

8.2.2. Diagnostic algorithm calibration

Data from the first seven LEEP patients, in chronological order, amongst the eight LEEP patients suitable for study were chosen to form a calibration set. Only LEEP patients were chosen for the calibration set because pathology information over much of the cervix is available, whereas with colposcopy patients, pathology information is available for biopsied sites only. Calibration is performed in three steps, corresponding to the steps of diagnosis described above that require calibration (Step 1, 2, and 4). In Step 1, we select endocervix tissue from the calibration set using visual criteria, as in colposcopy. The transformation zone is identified using pathology. We subsequently identify the differences in A and Hb spectroscopy parameters that distinguish transformation zone from endocervix in the calibration patients and train the likelihood functions in Bayes' rule to compute the PP of endocervix given a spectroscopy measurement. We estimate the necessary prior probabilities of endocervix and non-endocervix by determining the area fraction of tissue in the seven calibration patients that are endocervix. The threshold is set by

using the PP to identify endocervix in each calibration patient. In Step 2, we select normal squamous epithelium in the calibration set from pathology information and compare spectroscopy parameters measured from squamous to those measured from transformation zone. The differences in A and Coll between squamous and transformation zone are used to select threshold values distinguishing squamous epithelium from the transformation zone. In Step 3, we select transformation zone tissue sites on the calibration patients which were HSILs and non-HSILs based on pathology. We then identify normalized spectroscopy parameters that distinguish HSILs from non-HSILs and train the likelihood functions in Bayes' rule to compute the posterior probabilities of HSIL. We estimate the necessary prior probabilities of HSIL and non-HSIL by determining the area fraction of transformation zone tissue in the seven calibration patients.

After the four step diagnostic algorithm has been trained, we apply it on four patients (one LEEP and three colposcopy) prospectively to first segment tissue types and then identify areas in transformation zone tissue with HSIL as determined by quantitative spectroscopy imaging.

8.3 Results

Figure 8.3.1. shows several spectroscopy parameter maps measured from the cervix. The dark orifice near the center of Figure 8.3.1.(a) is the cervical os. Surrounding the os is deep red endocervical tissue, which owes its coloration to greater hemoglobin absorption as illustrated in Figure 8.3.1.(b). Away from the os near the edge of the cervix is the ectocervix, which is characterized by higher scattering (Figure 8.3.1.(c)). Between the endocervix and ectocervix is transformation zone where spectroscopy parameters transitions from columnar to squamous values. As already demonstrated in Chapter 6, the optical properties of the cervix vary with anatomical region, therefore, it is important to identify spectroscopy parameters that separate HSIL from non-HSIL within one anatomical region. We focus here on the transformation zone where the vast majority of HSILs occur.

Figure 8.3.1.(d) is the disease map determined by LEEP pathology for this patient. The white lines indicate regions along the 12 sections confirmed to have

HSIL. Other regions of the cervix may also have HSIL, but these could not be confirmed by pathology because some regions of the LEEP specimen had denuded mucosal surfaces (epithelium has been damaged).

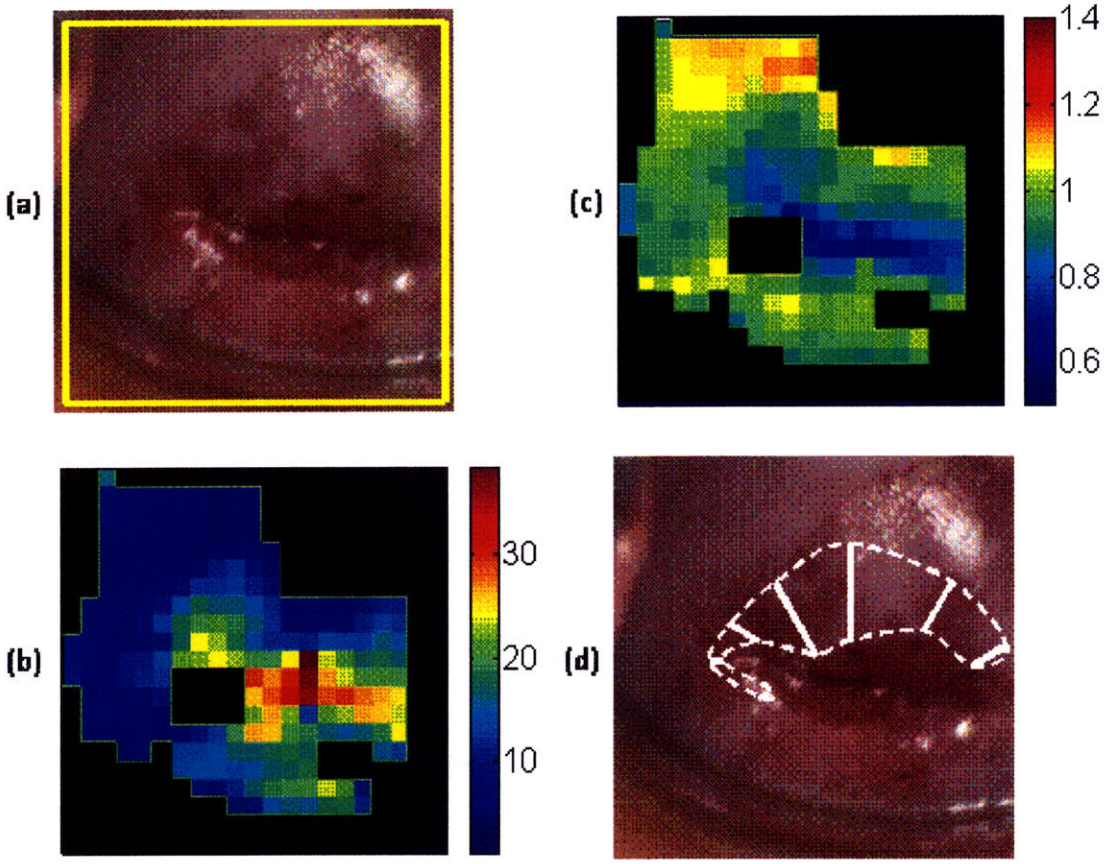

Figure 8.3.1. (a) A white light photograph of the cervix with yellow lines marking the approximately 2.1 cm x 2.1 cm square scanned by QSI. (b) and (c) Maps of the Hb and A scattering parameter measured at each 1 mm x 1 mm pixel. Points with no spectroscopy data due to the presence of specular reflection, motion, or non-cervical tissue are colored black in the parameter maps. (d) Disease map determined by LEEP pathology. Solid white lines indicate regions of the cervix confirmed to have HSIL by pathology. HSIL may be present in other parts of the cervix, but these sites could not be confirmed due to denuded mucosal surfaces. Dashed white lines delineate the area estimated to have HSIL by connecting the ends of the solid lines.

As already shown in the contact probe study (Chapter 7), the difference in spectroscopy parameters between HSIL and non-HSIL tissue in the transformation zone illustrate the importance of normalizing for patient-to-patient variation by showing the improved contrast between HSIL and non-HSIL when viewed with normalized spectroscopy parameters. The importance of using normalized spectroscopy parameters is shown in Figure 8.3.2. Figure 8.3.2.(a) is a box plot of the *A* parameter (reduced scattering coefficient at 700 nm) measured from HSIL and non-HSIL sites on multiple calibration patients. HSIL exhibits lower scattering than non-HSIL tissue in the transformation zone, as already demonstrated in Chapter 7.

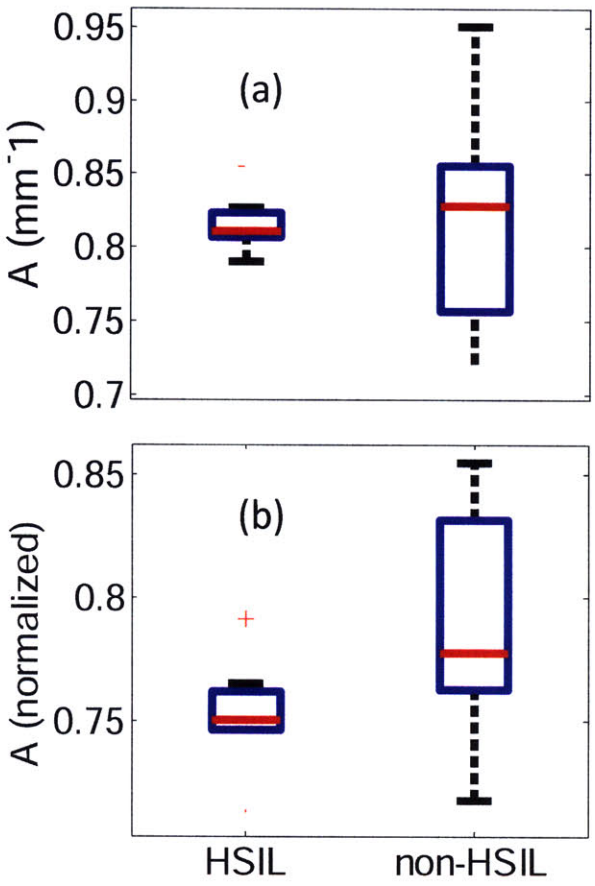

Figure 8.3.2. Box plots of spectroscopy parameters measured from HSIL and non-HSIL sites in the transformation zone of calibration patients. (a) A scattering parameter. (b) Normalized A parameter. The red line is the median and the blue box indicates the 25th and 75th percentiles. The black lines indicate the extent of the data and red crosses indicate outliers.

Performing a two-sided Wilcoxon Rank Sum test on the data shows A has a p-value of 0.60 for distinguishing HSIL from non-HSIL. A parameter before normalization has no diagnostic power. Figure 8.3.2.(b) is a box plot of the normalized A parameter measured from HSIL and non-HSIL sites on multiple calibration patients. After normalization, we see HSIL continues to exhibit lower scattering than non-HSIL tissue. However, a two-sided Wilcoxon Rank Sum test shows normalized A has a p-value of 0.022 for distinguishing HSIL from non-HSIL, which is by convention significant. The imaging results presented here and contact-probe results presented in Chapter 7 both show normalizing spectroscopy parameters enhances contrast between HSIL and non-HSIL tissue in cervical transformation zone.

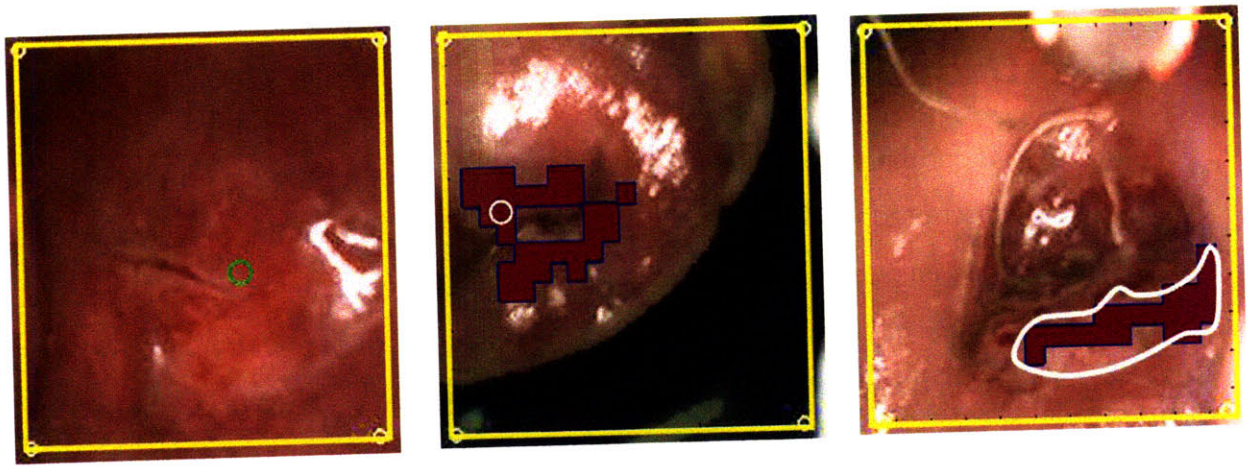

Figure 8.3.3. Diagnostic maps computed from spectroscopy parameters measured from two colposcopy, (a) and (b), and one LEEP patient, (c). Dark red areas are HSIL as determined by QSI. Transparent areas either are non-HSIL or have no diagnosis due to specular reflection, foreign objects, or the presence of endocervix tissue. The green circle in (a) is the site of a negative biopsy. The white circle in (b) is the site of a positive biopsy. The white region in (c) is an approximate area with HSIL according to LEEP pathology. The solid white lines are obtained in the same fashion as the dashed white lines in Figure 8.3.1.(d). The yellow lines delineate the 2.1cm x 2.1cm area scanned by QSI.

We found that A parameter after normalization were significantly different between HSIL and non-HSIL within transformation zone. We model probability distributions of HSIL and non-HSIL as Gaussians. We used Bayes' rule to calculate the posterior probability of HSIL in two colposcopy and one LEEP patient from their normalized *A* parameter maps. One of the three prospective colposcopy patients did not have normal squamous epithelium in the field of view, so no QSI diagnosis is available in this case. We then obtain the spatially continuous posterior probability maps and threshold to obtain the diagnostic maps in Figure 8.3.3. Figure 8.3.3.(a) and (b) shows QSI accurately predicts the presence and absence of HSIL in two biopsy cases. QSI would have saved the patient in Figure 8.3.3.(a) one unnecessary biopsy. In Figure 8.3.3.(c), QSI predicts an extensive region of HSIL from approximately 4 o'clock to 8 o'clock while LEEP pathology reported a similar sized region of HSIL in the same area.

8.4 Discussion and Conclusions

The primary distinction between quantitative spectroscopic imaging and existing spectroscopy imaging is QSI's ability to directly measure tissue properties such as the amount of scatterers, hemoglobin oxygen saturation, and collagen concentration. This is done by comparing the measured spectra with models of light propagation in tissue. Previous spectroscopy imaging studies relied on features in the spectra, such as the mean intensity and slope, which do not directly correspond to changes in tissue properties[8,9]. As a result, QSI can detect intrinsic tissue morphological and biochemical changes associated with disease. Intrinsic tissue properties do not vary with instrumentation implementation while spectral features such as mean intensity and slope are instrument dependent. Using quantitative spectroscopy has allowed our imaging study to observe the same differences in normalized spectroscopy parameter *A* (reduced scattering coefficient) between HSIL and non-HSIL tissue as our companion contact-probe study[10]. This example illustrates the advantage offered by quantitative spectroscopy in the research and development stage where frequent instrumentation changes are required. Results obtained with a first generation instrument can be more easily translated to a second

generation instrument. For example, contact-probe results can be applied to a wide-area imaging system.

Quantitative spectroscopic imaging will be evaluated in a larger study in the cervix to determine its abilities to address specific clinical needs, such as reducing the number of biopsies in patients referred for colposcopy without significantly affecting dysplasia detection.

8.5 References

1. A. Milbourne, S. Y. Park, J. L. Benedet, D. Miller, T. Ehlen, H. Rhodes, A. Malpica, J. Matisic, D. Van Niekirk, E. N. Atkinson, N. Hadad, N. Mackinnon, C. Macaulay, R. Richards-Kortum and M. Follen, "Results of a pilot study of multispectral digital colposcopy for the in vivo detection of cervical intraepithelial neoplasia," *Gynecol Oncol* **99** (3 Suppl 1), S67-75 (2005).
2. R. D. Alvarez and T. C. Wright, "Effective cervical neoplasia detection with a novel optical detection system: a randomized trial," *Gynecol Oncol* **104** (2), 281-289 (2007).
3. T. DeSantis, N. Chakhtoura, L. Twiggs, D. Ferris, M. Lashgari, L. Flowers, M. Faupel, S. Bambot, S. Raab and E. Wilkinson, "Spectroscopic imaging as a triage test for cervical disease: a prospective multicenter clinical trial," *J Low Genit Tract Dis* **11** (1), 18-24 (2007).
4. D. G. Ferris, R. A. Lawhead, E. D. Dickman, N. Holtzapple, J. A. Miller, S. Grogan, S. Bambot, A. Agrawal and M. L. Faupel, "Multimodal Hyperspectral Imaging for the Noninvasive Diagnosis of Cervical Neoplasia," *J Low Genit Tract Dis* **5** (2), 65-72 (2001).
5. S. Y. Park, M. Follen, A. Milbourne, H. Rhodes, A. Malpica, N. MacKinnon, C. MacAulay, M. K. Markey and R. Richards-Kortum, "Automated image analysis of digital colposcopy for the detection of cervical neoplasia," *J Biomed Opt* **13** (1), 014029 (2008).
6. D. G. Ferris, J. T. Cox, D. M. O'Connor, V. C. Wright and J. Foerster, *Modern Colposcopy: Textbook and Atlas*, Kendall Hunt, (2004)
7. J. Canny, "A Computational Approach to Edge-Detection," *Ieee Transactions on Pattern Analysis and Machine Intelligence* **8** (6), 679-698 (1986).
8. R. J. Nordstrom, L. Burke, J. M. Niloff and J. F. Myrtle, "Identification of cervical intraepithelial neoplasia (CIN) using UV-excited fluorescence and diffuse-reflectance tissue spectroscopy," *Lasers in Surgery and Medicine* **29** (2), 118-127 (2001).
9. W. K. Huh, R. M. Cestero, F. A. Garcia, M. A. Gold, R. S. Guido, K. McIntyre-Seltman, D. M. Harper, L. Burke, S. T. Sum, R. F. Flewelling and R. D. Alvarez, "Optical detection of high-grade cervical intraepithelial neoplasia in vivo: results of a 604-patient study," *Am J Obstet Gynecol* **190** (5), 1249-1257 (2004).

10. J. Mirkovic, C. Lau, S. McGee, C.-C. Yu, E. Stier, C. Crum, A. d. l. Morenas, L. Galindo, J. Nazemi, V. Feng, C. McGahan, D. Schust, K. Badizadegan, R. Dasari and M. Feld, *Quantitative spectroscopy for detection of cervical dysplasia in vivo: development of a diagnostic algorithm.* 2008.

CHAPTER 9

Correlation of Spectroscopy to Pathology Biomarkers of Cervical Dysplasia

In this Chapter we investigate correlation between spectroscopy parameters and pattern of staining of two objective biomarkers for cervical dysplasia diagnosis $p16^{INK4a}$ and Ki-67.

9.1 Motivation

The histopathology diagnosis of cervical neoplasia has an important role in patient management and is encumbered by high interobserver disagreement.[1-3] A diagnosis of low-grade squamous intraepithelial lesions (LSILs) in particular is a subject to high discordance among pathologists, and there is considerable interobserver discordance in the interpretation of high grade lesions (HSILs), particularly those at the lower end of this spectrum (CIN2). While not all of these problems can be ameliorated by detection alone, an objective biomarker of cervical dysplasia would allow unambiguous identification of truly dysplastic cells and/or possibly predict disease progression.

Considerable research has been devoted to better understand the molecular events involved in cervical carcinogenesis and to develop novel diagnostic methods which may improve the poor interobserver agreement in pathology. It is now widely accepted that persisting infection with high-risk human papilloma virus (HPV) types is a necessary, although not sufficient, variable for the development of cervical cancer. As already discussed in Chapter 2, infection by HPV is usually self-limited and transient. It is estimated that the cumulative risk of such infections in 70 years of a women's life is more than 70%. However, only very few women will ever develop both a persistent infection and an eventual cervical malignancy. The latent infection produces no cytopathic effects and epithelial morphologic abnormalities, since HPV DNA only resides in the basal cells and infectious virions are not produced. If a productive viral infection is established, large amount of virions is formed. This produces the cytopathic effects of HPV characteristic for the LSIL, such as koilocytosis, superficial nuclear atypia and cytoplasmic vacuolization. Replication and production of new infectious virions occurs only in the intermediate epithelial layer, and not in the basal/parabasal layers, as this process requires certain degree of epithelial cell differentiation. Since intermediate cells are determined to die, the viral infection causes almost no damage to the infected host.

The cervical HSILs and ultimately cancer develop as a consequence of uncontrolled early gene expression by oncogenic HPVs in the basal and parabasal

epithelial layers, which is relatively rare event.[4] Imbalance in the expression of the viral E6 and E7 genes is crucial in oncogenesis. The E6 protein supports premature degradation of the cellular p53 tumor suppressor gene and thus interferes with the apoptotic function of the host cell. The E7 protein induces destabilization of the retinoblastoma protein (Rb) complex and thus allows the cell to evade cell cycle control. Interference of viral genes with pathways involved in the replication of the epithelial cell and life cycle leads to chromosomal instability, which eventually leads to cancer.

Given the high prevalence of HPV infection, the best strategy for early detection is to target the subgroup of HPV infected cells that have acquired chromosomal instability. One of the approaches used in discovery of useful biomarkers of cervical dysplasia is the analysis of protein expression profiles that occur as a consequence of the deregulated expression of the viral oncogenes. Recent studies have shown that immunohistochemical staining for $p16^{INK4A}$ will discriminate dysplastic and malignant cervical epithelia from their benign mimics. Strong overexpression of $P16^{INK4a}$ protein was shown to identify cells with deregulated expression of the HPV.

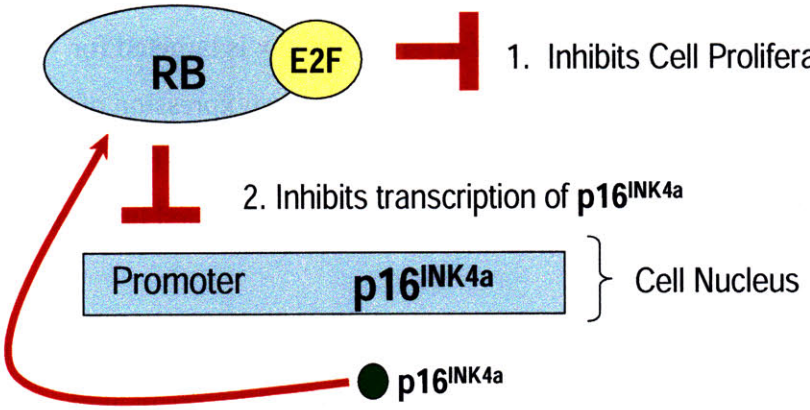

Figure 9.1.1 $p16^{INK4a}$ expression in the normal cell. RB-retinoblastoma protein, E2F-cellular transcription factor that promotes cell proliferation.

$p16^{INK4a}$ is a negative regulator of the cell cycle. It belongs to a class of cyclin dependent kinase (CDK) inhibitors, and it is involved in the retinoblastoma (Rb)

tumor suppression pathway. As explained in Figure 9.1.1. normal cells expressing $p16^{INK4a}$ are cell cycle arrested.

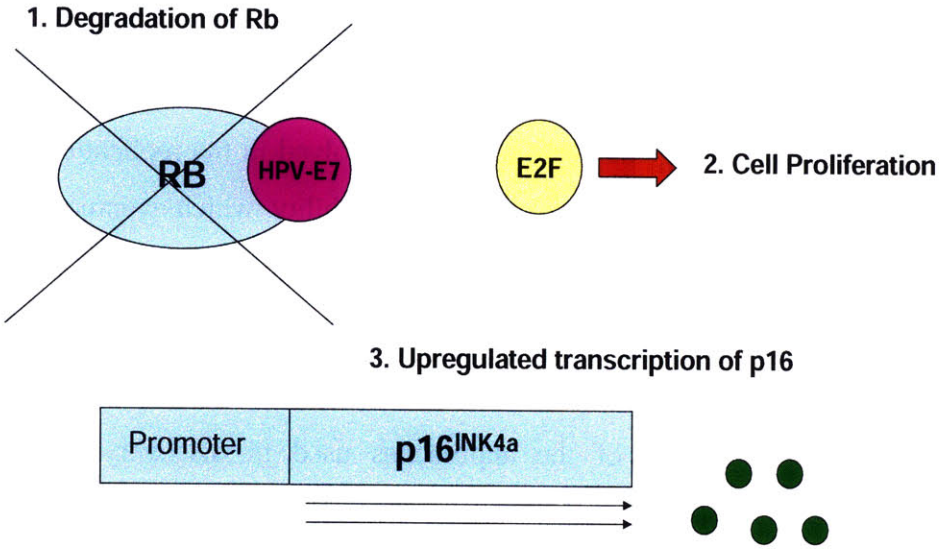

Figure 9.1.2. $p16^{INK4a}$ expression in the HPV-transformed cell. RB-retinoblastoma protein, E2F- cellular transcription factor that promotes cell proliferation, HPV-E7- viral protein that induces destabilization of RB

In HPV transformed cells, HPV-E7 forms a complex with Rb, which releases E2F and causes cellular proliferation. HPV-E7-Rb complex is targeted for ubiquitination and degraded. Degradation of Rb causes overexpression of $p16^{INK4a}$ As a result, the HPV transformed cell exhibits overexpression of $p16^{INK4a}$ and are proliferating, unlike normal cells which would be cell cycle arrested in those conditions.

$p16^{INK4a}$ is a sensitive biomarker of cervical dysplasia; however, atrophic and metaplastic epithelia may occasionally produce false positive result with $p16^{INK4a}$. Another immunohistochemistry stain, Ki-67, is used in combination with $p16^{INK4a}$ to improve the specificity of dysplasia detection. Ki-67 is universally used to evaluate cell proliferation as it highlights cells with active DNA replication. It does not always distinguish dysplastic proliferating cells from normal proliferating cells, but when used as an adjunct to $p16^{INK4a}$ it increases test specificity for dysplastic cells.

The objective of this chapter was to correlate the contact-probe spectroscopy measurements discussed in Chapter 7 with a pattern of biomarker staining.

9.2 Methods

The contact probe *in vivo* study involved 43 patients undergoing colposcopic evaluation following an abnormal Pap smear, including atypical squamous cells of undetermined significance (ASC-US), atypical squamous cells- cannot exclude HSIL (ASC-H), LSIL, and HSIL. For each patient, reflectance and fluorescence spectra were collected from a colposcopically normal squamous (CNS) site as well as abnormal sites using a FastEEM instrument, described in Chapter 4. The optical fiber probe, which samples an area of tissue ~1 mm in diameter, was disinfected with CIDEX OPA (Advanced Sterilization Products, Irvine, CA) before each procedure. After the application of acetic acid (5% solution) to the cervix during colposcopy, the probe was brought into gentle contact with the tissue. Each measurement which consisted of the average of 5 sets of white light reflectance spectra (300-800 nm emission) and 5 sets of 9 fluorescence spectra (308-460 nm excitation) was acquired in approximately 3s. The standard deviation of the 5 spectra was also recorded. A set of 2-3 measurements were acquired for each tissue site. Colposcopically abnormal sites were then biopsied and evaluated by histopathology. Clinically normal sites were not biopsied.

9.2.1. Histopathology

Each biopsy specimen from the contact probe study of cervical dysplasia in vivo, previously described in Chapter 5, underwent standard histopathological processing. The hematoxylin and eosin stained tissue sections were evaluated by three experienced pathologists using standard diagnostic criteria. We used a majority diagnosis (agreement of two of the three pathologists) to determine the disease diagnosis of the study samples. Each biopsied site was classified as either non-dysplasia, LSIL, or HSIL. We further employed two immunohistochemistry stains described above, $p16^{INK4a}$ and Ki-67, which when used in combination are sensitive and specific biomarkers of cervical dysplasia. Tissue from most but not all of the study sites stained by H&E were available for additional staining. The presence of

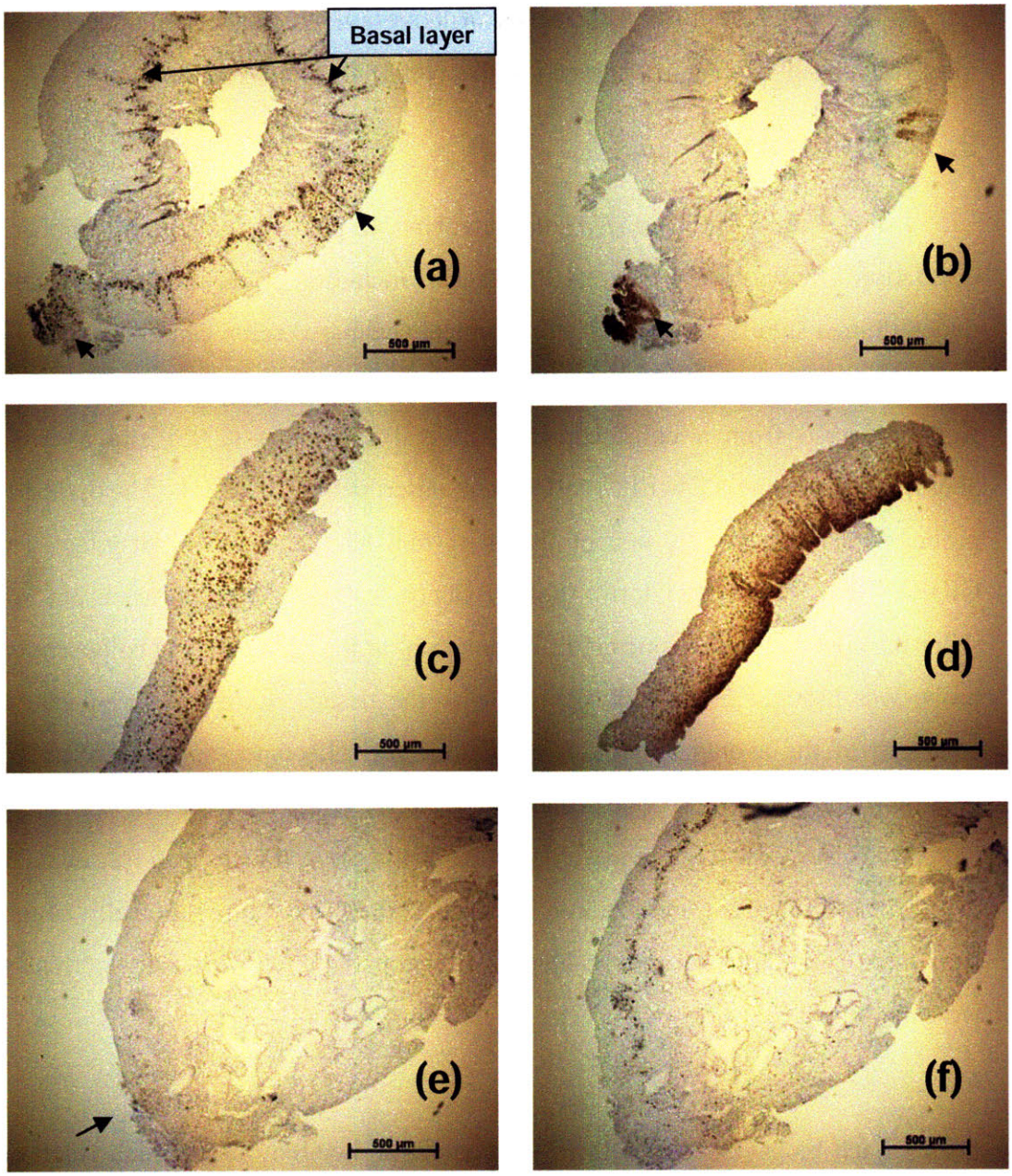

Figure 9.2.1. Biomarker staining pattern. Photographs on the left, ((a), (c), and (e)) are p16 ^{INK4a} immunohistochemistry stains. Photographs on the right ((b), (d), and (f)) are Ki-67 immunohistochemistry stains. Positive patchy staining pattern indicated in short black arrows is shown in (a) and (b). Positive diffuse staining pattern is shown in (c) and (d). Positive p16 ^{INK4a} indicated by short black arrow, but negative Ki-67, of the same tissue section is shown in (e) and (f) respectively, giving the overall negative score.

p16 ^{INK4a} or Ki-67 staining (positive vs. negative), as well as its pattern (diffuse vs. patchy) for each available biopsied tissue site was recorded. If a site was positive for both p16 ^{INK4a} and Ki-67 an overall positive result for biomarker staining was assigned to that site. If the site was negative for both, or positive for one, and negative for the other, an overall negative result for biomarker staining was assigned to that site. Virtually all epithelia will exhibit some Ki-67 staining, so a positive score required immunostaining in the upper epithelial layers, which is not characteristic of non-neoplastic epithelium but can happen in inflamed cervical mucosa. Examples of biomarker staining patterns are shown in Figure 9.2.1.

Overall biomarker staining result was first correlated to consensus diagnosis. We then developed a spectroscopy algorithm to differentiate biomarker positive sites from biomarker negative sites. To correlate overall biomarker staining to pathology majority diagnosis, we determined how many HSIL, LSIL, and non-dysplasia sites stained positively for biomarkers. We used logistic regression to develop spectroscopy algorithm to differentiate biomarker positive from biomarker negative sites. The likelihood ratio test was used to assess the significance of each of the spectroscopic parameters in the logistic regression model. A p-value<0.05 was considered to be significant. Leave-one-out cross-validation (LCV) was used to construct receiver-operator characteristic (ROC) curves for the spectral algorithms.

9.3 Results

9.3.1. Correlation of biomarker staining result to consensus pathology

We found that the vast majority of HSIL (7/8), some LSIL (6/10), and none of the non-dysplastic sites (0/23) stained negatively for biomarkers. Overall, our data set consisted of 13 sites with a positive biomarker score and 23 sites with a negative biomarker score. Table 9.3.1. summarizes the results of the biomarker staining.

Table 9.3.1. Biomarker staining results

H&E Consensus Diagnosis	# Sites			
	p16 +	Ki-67 +	Biomarker +	Total
No dysplasia	2	1	0	23
LSIL	7	7	6	10
HSIL	7	8	7	8
All sites	16	16	13	41

9.3.2. Correlation of biomarker staining result to spectroscopy measurements

When logistic regression and LCV were performed, positive sites could be differentiated from negative based on Coll, with an AUC, sensitivity and specificity of 0.78, 77%, and 79% respectively. The contribution of other parameters to the diagnostic performance was negligible. The boxplots of Coll, as well as the ROC curve for differentiating biomarker positive from negative sites, are shown in Figure 9.3.1.

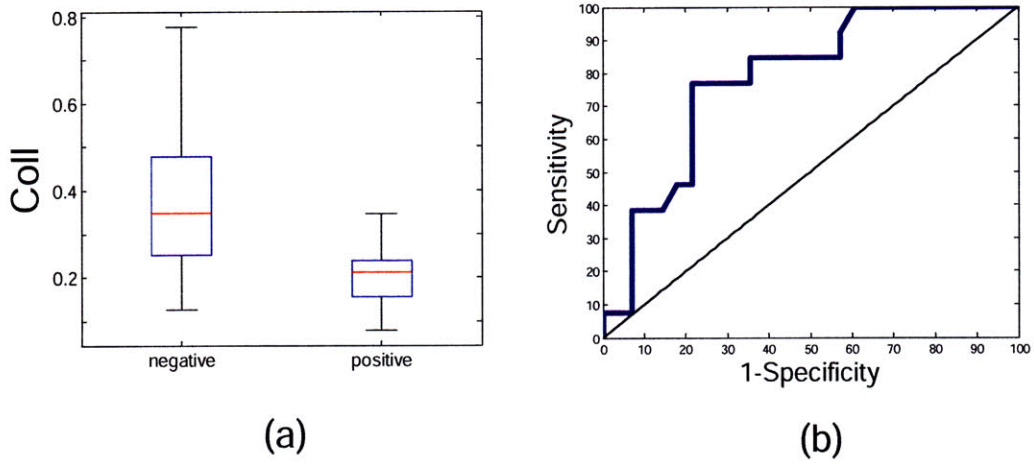

Figure 9.3.1. Discrimination of biomarker positive vs. negative sites. Boxplots of normalized (a) Coll and (b) LCV ROC curve for the diagnostic algorithm (Coll only).

9.4 Discussion and Conclusions

Biomarker positive sites can be differentiated from biomarker negative sites by low values of Coll parameter. Diagnostic performance is lower than when the "gold standard" was a majority diagnosis in pathology (AUC, sensitivity and specificity of 0.78, 77%, and 79% respectively). Clinically the most relevant issue is the diagnosis of HSIL, achieved by majority diagnosis and by a spectroscopic algorithm described in Chapter 7 (AUC, sensitivity and specificity of 0.84, 89%, and 79% respectively). As biomarker positive sites are composed of the vast majority of HSILs plus a portion of LSILs and biomarker negative sites are composed of all of the non-dysplastic sites plus the rest of the LSILs, this diagnostic criterion functions with some effectiveness, albeit differently than standard H&E pathology diagnosis. Studies correlating pattern of biomarker staining (diffuse vs. patchy) and spectroscopy have yet to be done.

9.5 References

1. H. C. W. Devet, P. G. Knipschild, H. J. A. Schouten, J. Koudstaal, W. S. Kwee, D. Willebrand, F. Sturmans and J. W. Arends, "Interobserver Variation in Histopathological Grading of Cervical Dysplasia," *Journal of Clinical Epidemiology* **43** (12), 1395-1398 (1990).
2. W. G. McCluggage, H. Bharucha, L. M. Caughley, A. Date, P. W. Hamilton, C. M. Thornton and M. Y. Walsh, "Interobserver variation in the reporting of cervical colposcopic biopsy specimens: Comparison of grading systems," *Journal of Clinical Pathology* **49** (10), 833-835 (1996).
3. M. H. Stoler, M. Schiffman and A. S. C. Undetermin, "Interobserver reproducibility of cervical cytologic and histologic interpretations - Realistic estimates from the ASCUS-LSIL triage study," *Jama-Journal of the American Medical Association* **285** (11), 1500-1505 (2001).
4. J. Monsonégo, *Emerging issues on HPV infections : from science to practice*, Karger, Basel ; New York (2006)

CHAPTER 10

Future Directions

This chapter proposes several future directions that may be pursued in light of the accomplishments of this thesis.

10.1 Large scale QSI clinical *in vivo* study in the cervix

The results of our contact-probe clinical in vivo studies have demonstrated that the normalized A parameter, the reduced scattering coefficient at 700 nm, alone is sufficient for accurately distinguishing HSIL from non-HSIL within the transformation zone. Our pilot study with the QSI instrumentation has confirmed the results of the contact probe studies. A larger QSI study with an objective to 1) confirm the results of the QSI pilot study, and 2) to estimate the accuracy with which QSI can identify tissue with HSIL in the transformation zone is underway. The QSI implementation will be evaluated on patients at risk of cervical dysplasia referred to either colposcopy or LEEP. The study will be conducted on approximately 80 patients with half used for developing QSI's diagnostic algorithm and the other half for a prospective evaluation.

The diagnostic algorithm will be developed and optimized for the first forty patients in the same manner as explained in Chapter 8. The algorithm will then be prospectively evaluated on the second group of forty patients. The prospective evaluation will be conducted on both colposcopy and LEEP patients and will involve comparing the accuracy of colposcopy to the accuracy of QSI for identifying HSIL. For colposcopy patients, the clinician will determine where biopsies are required. Similarly, QSI will determine if biopsies are necessary at the same sites. The gynecologist will be blinded to the results of imaging algorithm. After obtaining pathology results, we will determine if QSI is more accurate in determining the presence or absence of HSIL at the biopsied sites. For LEEP patients, the clinician will determine where they would have taken a biopsy if the patient were a colposcopy patient. Similarly, QSI will determine where biopsies would be taken if the patient were a colposcopy patient. After pathology results are available, QSI's accuracy relative to colposcopy's will be determined. We will compare QSI to comparable published colposcopy results in addition to those obtained during this study.

10.2 Development of simple instrumentation for detection of cervical dysplasia

If the results of the contact-probe study and the QSI pilot study are further confirmed with the results of the larger study (section 10.2), this may direct the design of a significantly simpler, faster, and less expensive cervical dysplasia imaging system. One potential design of new system includes illumination of a 1 mm^2 region of the cervix with nearly monochromatic red light, detection by a photodiode, and raster-scanning using a small mechanical actuator. Because tissue has relatively low absorption under red light illumination, scattering can be disentangled from absorption and elucidated from reflectance spectra. Tissue sites with low intensity of returning light detected by a photodiode would be classified as HSIL. This is equivalent to identifying regions of the cervix with low A parameter. The scanning process would provide examination of the entire cervix. Such a system could potentially cost very little to manufacture and be useful as a valuable addition to any commercial digital colposcope. Also, the system's simplicity may facilitate its use as a cervical dysplasia screening and diagnostic tool in developing countries where medical infrastructure is weak. In such a setting, treatment procedures can be applied immediately after the system detects HSIL.

10.3 Quantitative spectroscopy study of Anal Dysplasia

A study that aims to develop an optically based technique for the diagnosis of neoplastic changes in the anus, as an extension of the cervical dysplasia contact-probe project has been initiated. This study is motivated by the fact that cervical and anal preinvasive diseases are tightly associated. The cervix and anal canal share embryologic, histologic and pathologic characteristics. The squamocolumnar junction and the transformation zone where normal metastatic change and abnormal dysplastic change may occur are found in both organs. Both anal squamous intraepithelial lesions (ASIL) and cervical squamous intraepithelial lesion (SIL) are diagnosed almost exclusively in the presence of human papilloma virus (HPV) infection. The spectrum of HPV types associated with ASIL is similar to that

described in the dysplastic cervix. Furthermore, diagnosis of SIL caries a more than threefold increase in the risk of simultaneous abnormal anal smear.[1]

Since ASILs and SILs have common histopathological features, screening and diagnostic procedures for these conditions are identical. Both anal and cervical cytology are described using the Bethesda classification system with same criteria. Following the detection of abnormal anal cytology, the next step is high-resolution anoscopy (HRA). The HRA procedure is equivalent to a colposcopy procedure. The same instrument and enhancing solutions are used to visualize anal tissue as in the case of cervical tissue. Just as in colposcopic procedure, variations in the density of whitening of dysplastic epithelium, aberrant surface vascular pattern, and mosaicism are features of interest.

Unlike cervical lesions, for which regression and progression rates are well established, relatively little is known of the long-term natural history of ASIL and studies are currently in progress to address this issue.[2] Therefore, screening and treatment guidelines are not yet universally accepted. However, certain population groups are at increased risk of developing anal cancer and recommended screening and treatment guidelines for subjects at risk for HSIL have become available.[3] The following groups are associated with a significant risk of developing anal HSIL: 1) Women with cervical cancer, high-grade SIL, or vulvar cancer 2) All HIV-positive men and women regardless of sexual orientation 3) All men having sex with men (MSM) regardless of HIV status, 4) Transplant recipients, 5) All men and women with perianal condyloma. Therefore, the anal dysplasia study targets a slightly different population than the cervical dysplasia study.

Dr. Stier, M.D. from Department of Obstetrics and Gynecology, who is a current PI for the cervical dysplasia study, is a PI of anal dysplasia protocol. The same instrument used in the cervical dysplasia contact-probe study, described in Chapter 4, has been utilized for this study.[4] The subjects are contacted at their regular visit in Dr. Stier's anoscopy clinic. The visit is approximately 30 minutes long. If a patient returns to the clinic for a follow-up, he/she are asked if they would like to participate in study again. We aim to enroll up to 50 subjects in a one-year

period and to correlate spectroscopic findings with standard histologic diagnosis and with specific morphometric staining and analysis. Specific stains will include biomarkers: p16, to confirm the presence of HPV-related hot gene expression, and Ki-67 to determine the cellular proliferative status.

The extension of the cervical contact-probe project to include anal dysplasia will enable a study of cervical and anal lesions in parallel, since this could provide insight into biochemical and structural differences of apparently similar diseases.

10.4 References

1. S. E. Goldstone, B. Winkler, L. J. Ufford, E. Alt and J. M. Palefsky, "High prevalence of anal squamous intraepithelial lesions and squamous cell carcinoma in men who have sex with men as seen in a surgical practice," *Diseases of the Colon & Rectum* **44** (5), 690-698 (2001).
2. A. P. Zbar, C. Fenger, J. Efron, M. Beer-Gabel and S. D. Wexner, "The pathology and molecular biology of anal intraepithelial neoplasia: comparisons with cervical and vulvar intraepithelial carcinoma," *International Journal of Colorectal Disease* **17** (4), 203-215 (2002).
3. P. V. Chin-Hong and J. M. Palefsky, "Natural history and clinical management of anal human papillomavirus disease in men and women infected with human immunodeficiency," *Clinical Infectious Diseases* **35** (9), 1127-1134 (2002).
4. J. W. Tunnell, A. E. Desjardins, L. Galindo, I. Georgakoudi, S. A. McGee, J. Mirkovic, M. G. Mueller, J. Nazemi, F. T. Nguyen, A. Wax, Q. G. Zhang, R. R. Dasari and M. S. Feld, "Instrumentation for multi-modal spectroscopic diagnosis of epithelial dysplasia," *Technology in Cancer Research & Treatment* **2** (6), 505-514 (2003).

CHAPTER 11

Conclusions

Here we give an overview of thesis accomplishments followed by the final remarks.

11.1 Overview of Thesis Accomplishments

The overall goal of this thesis was to develop a real-time clinical diagnostic tool based on reflectance and fluorescence spectroscopy, which is accurate and free of confounding effect of anatomy, for detection of HSILs. In order to achieve such a goal the work in this thesis was focused on: 1) instrumentation improvement, 2) analysis model development, and 3) clinical in vivo studies of cervical dysplasia.

In Chapter 4 we described instrument improvements allowing for extraction of artifact free reflectance and fluorescence data. Two sources of artifact in tissue spectra collected during the contact probe pilot studies were identified, namely second order light generation by a diffraction grating, as well as the colposcopy light artifact. An instrumental method to remove this effect prospectively was implemented. A method to retrospectively remove artifact in already collected data was developed and enormous amount of valuable clinical data collected in vivo in patients with Barrett's esophagus has been salvaged.

In Chapter 5 we described the analysis model modification which improved: 1) the accuracy of parameter extraction, and 2) understanding of the physical basis for spectral diagnosis. We advanced our understanding of model based LSS analysis and showed that what we initially attributed to signal from nuclear scattering (LSS signal) is actually due to changes in hemoglobin absorption due to vessel packaging phenomena.

During the course of the clinical in vivo study, we developed an understanding of the physical basis for differences in the spectroscopic parameters due to tissue anatomy and disease. We demonstrated that both normal variations in tissue anatomy and disease are major sources of spectroscopic contrast, and that it was crucial to disentangle the effects of the two in order to develop reliable diagnostic algorithms.

In Chapter 6 we showed that normal transformation zone is spectroscopically different from the normal squamous epithelium. As the vast majority of the HSILs are found in the transformation zone, the spectral differences between normal

squamous and HSIL sites are largely due to the confounding effects of anatomy. We demonstrated that the inclusion of clinically normal squamous sites into a data set which is used to evaluate the diagnostic performance of the algorithm (HSILs vs. non-HSILs) produces unrealistically high performance values. We have shown that the clinically relevant issue that spectroscopy must address is how well HSILs can be differentiated from non-HSILs among clinically suspicious sites, the vast majority of which are found in the transformation zone of the cervix. In making this distinction in Chapter 7, we demonstrated that the spectroscopic contrast between non-HSIL and HSIL is enhanced if parameters are normalized by an internal standard, the corresponding parameter extracted from clinically normal squamous site of the same patient. The parameters A, α, Hb, bvr, and Coll were statistically significant for differentiating HSILs from non-HSILs within clinically suspicious sites after patient-to-patient normalization. However, the A parameter was the most diagnostic parameter and the addition of any other spectroscopy parameter does not contribute significantly to the diagnostic performance. The AUC, sensitivity, and specificity for leave-one-out cross-validation and logistic regression model are 0.85, 89%, and 79% respectively. Positive and negative predictive values are 48% and 97% respectively. The HSIL sites, most of which are characterized by a substantial amount of glandular stroma ($\geq$ 25 %), can be accurately distinguished from a group of non-HSIL sites exhibiting a substantial amount of glandular stroma by only two parameters, A and α. We concluded that Hb, bvr, and Coll are strongly dominated by anatomy, while a low A parameter and high α were true signatures of disease.

In Chapter 8, we extended these studies to an imaging modality and showed results which are consistent with the results of the contact probe study presented in Chapter 6 and 7. To develop an imaging modality we employed the principle of the "virtual probe" in order to provide wide area coverage while retaining the ability to extract detailed quantitative information about tissue biochemistry and morphology. The tip of the optical fiber is imaged to a tissue spot with similar geometry as the contact-probe, and then raster scanned across the entire organ to provide wide-area surveillance. The virtual probe provides several advantages over the full-field illumination. Since the delivery-collection geometry is small, we are able to extract

optical properties, such as reduced scattering coefficient and absorption coefficient independently. Furthermore, we are able to directly apply the knowledge acquired in the contact-probe studies to imaging studies. QSI can detect intrinsic tissue morphological and biochemical changes associated with disease. Intrinsic tissue properties do not vary with instrumentation implementation while spectral features such as mean intensity and slope are instrument dependent. Using quantitative spectroscopy has allowed our imaging study to observe the same differences in normalized spectroscopy parameter A (reduced scattering coefficient) between HSIL and non-HSIL tissue as the contact-probe study. This example illustrates the advantage offered by quantitative spectroscopy in the research and development stage where frequent instrumentation changes are required

The results of our contact-probe clinical in vivo studies have demonstrated that the normalized A parameter, the reduced scattering coefficient at 700 nm, alone is sufficient for accurately distinguishing HSIL from non-HSIL within the transformation zone. Our pilot study with the QSI instrumentation has confirmed the results of the contact probe studies. These results suggest the design of a significantly simpler, faster, and less expensive cervical dysplasia imaging system. One potential design of new system includes illumination of a 1 mm^2 region of the cervix with nearly monochromatic red light, detection by a photodiode, and raster-scanning using a small mechanical actuator. Such a system could potentially cost very little to manufacture and be useful as a valuable addition to any commercial digital colposcope. Also, the system's simplicity may facilitate its use as a cervical dysplasia screening and diagnostic tool in developing countries where medical infrastructure is weak. In such a setting, treatment procedures can be applied immediately after the system detects HSIL.

11.2 Final Remarks

One of the major findings identified during the course of our research was the fact that tissue scattering alone was not only sufficient, but the best measure for identifying HSIL disease within transformation zone of the cervix. The *in vivo* contact-probe study of cervical dysplasia first showed that the A parameter alone,

after normalization by an internal standard, provided the best diagnostic performance in differentiating HSIL disease from non-HSIL within clinically suspicious sites. These results were further confirmed in an *in vivo* imaging study of the cervix using the QSI system. In both studies we used complex, multi-modal instrumentation and several analysis methods to comprehensively study cervical tissue. The finding that only the A parameter has diagnostic importance suggests that a significantly simpler, faster, and less expensive instrument which only measures tissue scattering may be all that is required to reliably detect cervical disease.

If the results of the contact-probe study and the imaging pilot study are further confirmed based on a larger study (section 10.2), our laboratory will design a simplified instrument for detecting cervical dysplasia and investigate how effective this approach is in improving the accuracy of cervical dysplasia detection. In developed countries, this simple instrument could be used as an adjunct to colposcopy to reduce the amount of unnecessary biopsies. However, the greatest impact of this simple and relatively inexpensive instrumentation would be on cervical cancer diagnosis in developing countries, where patients are often subjected to "see and treat" approach due to a lack of medical infrastructure. Patients typically undergo visual inspection after application of acetic acid (VIA). The identification of suspicious lesions during VIA is followed by immediate treatment. The simple spectroscopic instrumentation could be used as an adjunct to VIA as a more reliable diagnostic to identify patients who need to undergo treatment (reduce false positives).parameter, the reduced scattering coefficient at 700 nm, alone is sufficient for accurately distinguishing HSIL from non-HSIL within the transformation zone. Our pilot study with the QSI instrumentation has confirmed the results of the contact probe studies. These results suggest the design of a significantly simpler, faster, and less expensive cervical dysplasia imaging system. One potential design of new system includes illumination of a 1 mm^2 region of the cervix with nearly monochromatic red light, detection by a photodiode, and raster-scanning using a small mechanical actuator. Such a system could potentially cost very little to manufacture and be useful as a valuable addition to any commercial digital colposcope. Also, the system's simplicity may facilitate its use as a cervical dysplasia screening and diagnostic tool

in developing countries where medical infrastructure is weak. In such a setting, treatment procedures can be applied immediately after the system detects HSIL.